The Flow Environment of Road Vehicles in Winds and Traffic

Simon Watkins, Riccardo Pagliarella

RMIT University, Melbourne, Australia
simon@rmit.edu.au

Abstract The aerodynamic development of a new vehicle is usually performed in smooth flow EFD or CFD domains with the vehicle in isolation. However the flow environment on-road is complex due to the presence of atmospheric winds, the wakes of nearby stationary objects and, depending upon driving conditions, the wakes of other vehicles. Winds and traffic generate a turbulent flow environment and can augment or reduce the mean velocity experienced by the moving vehicle. Recent work on turbulence arising from vehicles traversing the atmospheric boundary layer is reviewed and the consequence of upstream vehicle wakes is considered. The influence of distance and rear slant angle is examined, via wind-tunnel measurements of wakes of Ahmed bodies using dynamically calibrated multi-hole probes. The effect on very closely coupled vehicles (such as may occur in future platoons) is investigated via force and surface pressure measurements on two and three vehicle Ahmed bodies of varying rear slant angle. It is argued that the typical turbulence intensity for current highway driving is about 5%, but this can be significantly augmented when in the close proximity of other vehicles and/or during high winds. Further it is shown that for some vehicle forms, close coupling can increase the total platoon drag.

Preliminary Experiments Applying Active Flow Control to a 1/24th Scale Model of a Semi-Trailer Truck

L. Taubert and I. Wygnanski

The University of Arizona, Dept. of Aerospace and Mechanical Engineering
taubert@u.arizona.edu, wygy@email.arizona.edu

Abstract Preliminary experiments were carried out to investigate possible benefits of using a relatively new type of fluidic actuators (Raman & Raghu [1]) in combination with attached aft bodies to reduce the drag on a standard semi-trailer truck. The actuators generate oscillating jets that cause the formation of streamwise vortices that enhance the entrainment of the shear layer significantly. Taking into account the potential feasibility of any add-ons to a trailer, seven different bodies with simple geometries were chosen for this investigation.

Nomenclature

A_a	total open area of actuator nozzles
A_{cs}	cross section of trailer, based on total height
L_c	circumference of trailer
U_j	actuators jet velocity, based on flow rate
U_∞	free stream velocity
ρ	density of air
$C_\mu = 2*A_a/A_{cs}*(U_j/U_\infty)^2$	momentum coefficient
F_t	measured thrust force
F_d	measured drag force
$C_t = F_t/(1/2*\rho*U_\infty^2*A_{cs})$	thrust coefficient
$C_d = F_d/(1/2*\rho*U_\infty^2*A_{cs})$	drag coefficient
C_{d0}	C_d of baseline configuration (no actuation)
$D_{hydr} = 4*A_{cs}/L_c$	hydraulic diameter
Re	Reynolds number, based on D_{hydr}

Introduction

Significant improvements have been made in the last decades to reduce the drag of commercial vehicles (Cooper [2]), especially heavy trucks. Experiments were carried out in a wide range of Reynolds numbers (Cooper [2], Storms et al. [3]), up to on-the-road tests (Englar [4]) to check the validity of smaller-scale studies. The potential of further reducing fuel consumption and emissions led to numerous research projects applying active flow on heavy vehicles. Steady blowing was investigated (Coon and Visser [5]) as well as oscillatory forcing (Hsu et al. [6]) in combination with different configurations of added aft-bodies. All these approaches focus mainly on altering the spanwise structures of the flow. In contrast to this the type of actuation investigated preliminarily in this study is targeted at generating streamwise structures.

Experimental Setup

A 1/24th scale model of a Kenworth T-600 B with Great Dane trailer (Fig. 1a), was modified for this investigation. Main alterations were the addition of a pressurized chamber containing 20 actuators at the rear end of the trailer (Fig. 2a) and an aluminum rail connecting tractor and trailer, providing balance mount points of the model and a connection for the pressurized air, as shown in Fig. 1b.

The experiments were carried out in the open-return, suction wind tunnel at the AME Department of the University of Arizona. The test section is 122 cm wide, 85.5 cm high and 355 cm long. The model was mounted on a six-component balance using the standard pylon to which a pressurized air tube was attached and a separate pitch rod. A stationary false floor (Fig. 1a), 51 cm wide and 182.5 cm long was positioned approximately 2mm below the wheels of the model, 39 cm above the tunnel floor and starting approximately 30 cm upstream of the model.

Fig. 1a Truck model in wind tunnel

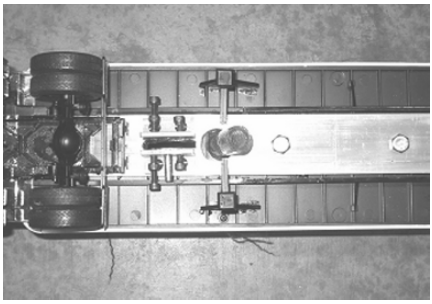

Fig. 1b Details: mount point and lines

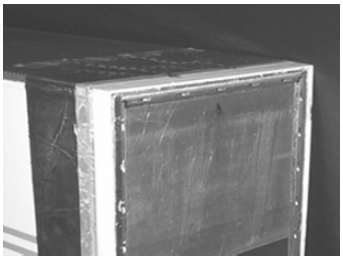

Fig. 2a Mounted actuators

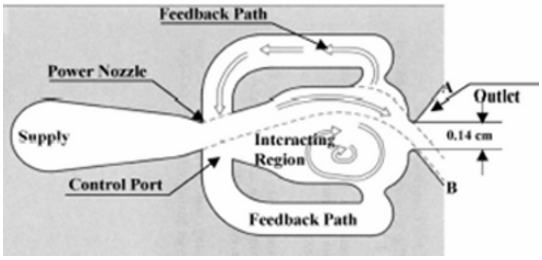

Fig. 2b Principle of actuator [1]

Active flow control was applied through fluidic actuators shown schematically in Fig. 2b. They were driven by pressurized air source and emitted oscillatory jets in the direction of streaming. For these actuators the frequency of the oscillations depends on the supplied flow rate and cannot be changed independently. It varied approximately between 1 and 2.5 kHz for the investigated range of C_μ.

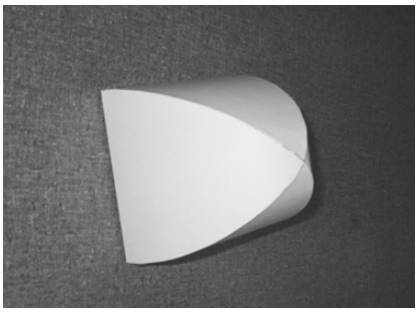

Fig. 3a Ellipsoid

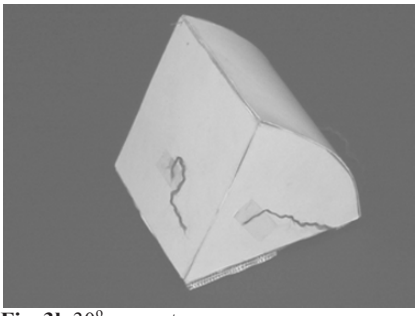

Fig. 3b 30° arc sector

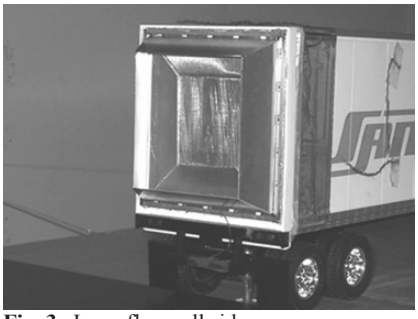

Fig. 3c Inner flaps, all sides

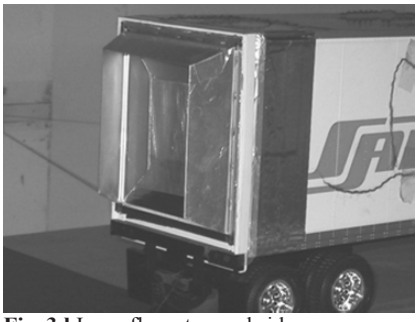

Fig. 3d Inner flaps, top and sides

Fig. 3e Outer flaps, top and sides

Fig. 3e Long flap

The main attraction of these actuators is their simplicity because they do not require moving parts and they proved themselves in laboratory tests associated with aeronautical applications. Five equally spaced actuators were mounted on each side at the very end of the trailer. The distance between the outer surface of the trailer and the center plane at which the jets oscillated, was approximately 6% of the width of the trailer, as shown in Fig. 2a.

In the first series of experiments various simple modifications to the trailer were investigated with the focus being on additions that will not impede the utility of the fundamental trailer design. Two different solid (closed) bodies were attached to the model. A three-dimensional ellipsoid of 100mm length with rectangular base (Fig. 3a), and a two-dimensional body formed by a 30° circular arc sector with its radius equal the vertical distance between the actuators (Fig. 3b). Both bodies filled the entire area between the actuators.

Five different types of flaps mounted onto the trailer's aft surface were investigated. A single long flap was formed by a sheet metal, 100mm long (the vertical distance between the actuators) and attached right below the top actuators at an angle of 20° to the horizontal, filling the entire horizontal space between the actuators shown in Fig. 3f. The other four configurations consisted of flaps either mounted flush with the outside surfaces, thus surrounding the actuators on the outside, or being mounted onto the trailer's aft surface and being surrounded by the actuators (Fig. 3d & e). The inclination of these flaps to the trailer's walls was 20°.

Two variations of these flap configurations were tested: first with flaps and active actuators on all four sides of the trailer and second with the bottom flaps removed and bottom actuators inactive (Fig. 3f). All configurations were investigated at three different Reynolds numbers and at four different momentum coefficients. The model was aligned parallel to the free stream in all cases.

Results

The drag coefficient of the basic configuration (without aft bodies) was approximately, C_D=0.62. This value varied little with Reynolds numbers over the range of Re considered. The various additions to the baseline configuration reduced the drag by 2-4% at the higher Re range, with the exception of the long flap that was suspended from the roof of the trailer and pulled air upward from the ground region into the wake of the trailer increasing the drag in that fashion by approximately 1-1.5% as shown in Fig 4.

The drag measured at different levels of actuation emanating from the entire circumference of the trailer's base is shown in figure 5. The jet momentum, or rather *the thrust that was measured in the absence of external stream was added to the drag* and the result was normalized by the particular baseline configuration of the appropriate geometrical addition at the Reynolds number at which the experiments were carried out. This normalization presumes that the same amount of compressed air could be used for jet propulsion and in the absence of deleterious interference one should recover the input momentum as thrust. Such thrust is also dependent on the velocity of the vehicle but this was not considered presently and thus the results may be somewhat pessimistic. Nevertheless any value that is lower than unity in Fig. 5 represents a net benefit to the system. Unfortunately the specific installation of the actuators around the periphery of the trailer's aft did not reduce the drag sufficiently to justify the momentum input.

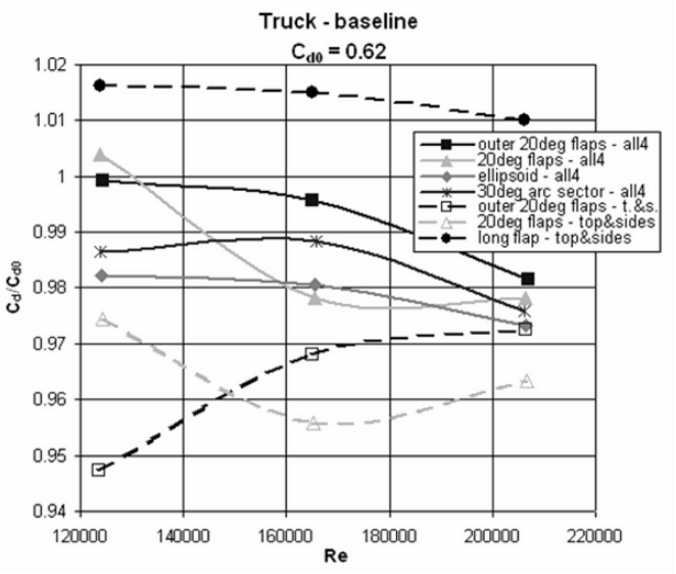

Fig. 4 The drag of a modified trailer relative to its basic configuration

In order to affect the base flow, the flaps or center-bodies were surrounded by the actuators generating a substantial discontinuity in the surface (backward facing step) around the circumference of the trailer's base. This arrangement was not conducive to drag reduction. For this reason one set of flaps was set flush with the trailer's sidewalls (see Fig. 3e) and although the actuation could only affect the external stream downstream of the flap's trailing edge its presence was somewhat beneficial provided the momentum coefficient, $C_\mu < 2\%$. In fact relative to the truck's original drag the reduction is in excess of 4% provided the alternative use of the momentum coefficient is not considered.

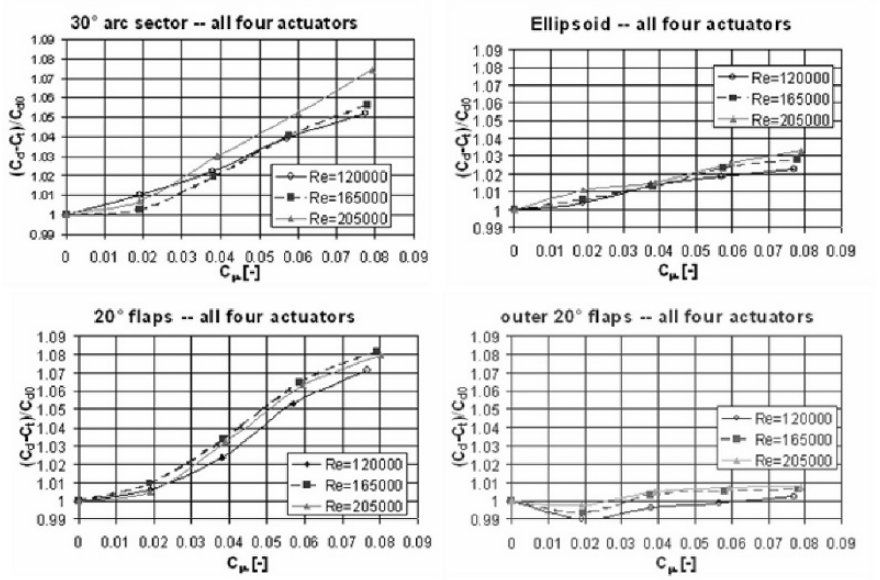

Fig. 5 The effect of four-sided actuation on the drag

The thrust was measured in the absence of an external stream and thus the penalty of considering it that way is too high and the results presented are overly pessimistic. Additional evidence for this pessimism is provided below in Fig. 7. Large differences in momentum recovered as thrust were observed for the different configurations shown in Figs. 5 and 6. A simple flow visualization study using tufts revealed that close to the center span or mid height of the trailer, the flow is deflected clearly inwards (Figs. 7b and d). This is caused by the entrainment of ambient fluid by the oscillating jets and is most visible in the absence of an external flow. In contrast, next to the corners of the trailer, the flow is jetting outwards (Figs 7a & c). This is easily explained by the oscillating jets from the top and one of the sides that intercept one another near the corner at an approximate angle of 90^o. This forces the flow away from the trailer, widening its wake and increasing the drag. This effect was also observed in the presence of the external flow at

different Re with different values of C_μ used. It is caused solely by the non-optimized positions of the actuators in combination with the direction of oscillation of the emitted jets.

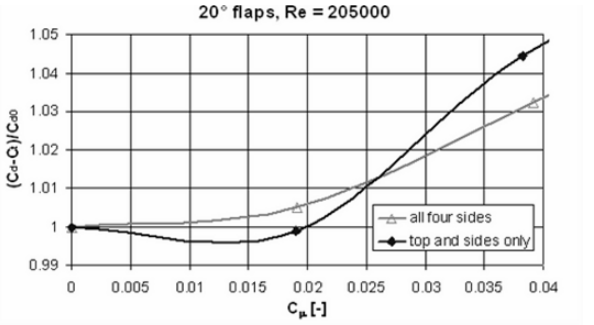

Fig. 6 Effect of actuator location

In order to test if the outflow from the corner has any effect on the drag the bottom flap that was interior to the actuators had been removed and the actuation was limited to the three remaining sides. At low momentum coefficient some benefit was drawn from the removal but it disappeared at higher C_μ (see Fig. 6).

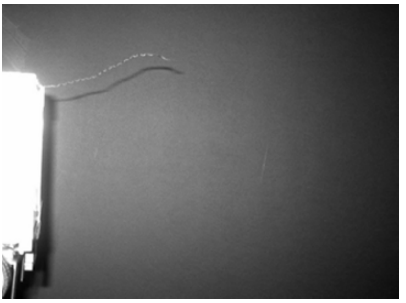

Fig. 7a Top right corner, side view

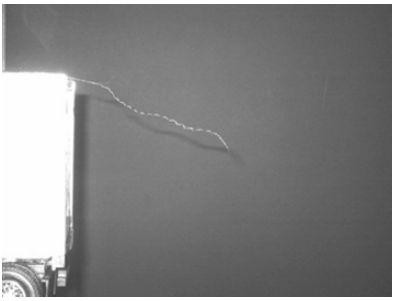

Fig. 7b Top center, side view

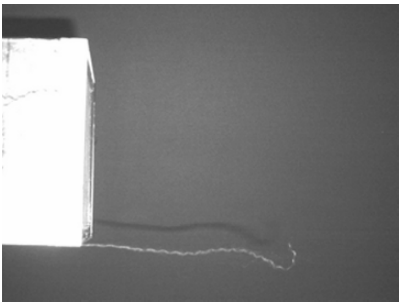

Fig. 7c Top left corner, top view

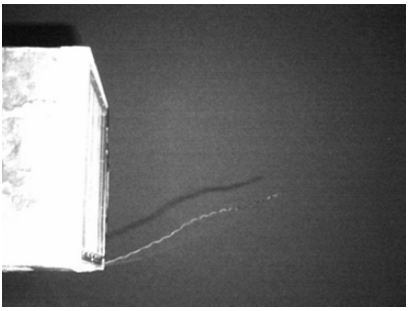

Fig. 7d Left center, top view

Concluding Remarks

The drag of a semi-trailer truck model was reduced by added aft bodies by up to 5.5% depending on the shape and size of the added body and the Re. When active flow control was added, its contribution to this reduction was minor. The maximum reduction obtained by active flow control was approximately 1% for the short flaps that were inclined at 20^o to the sidewalls and the top of the trailer.

One important factor of the low effectiveness of the actuation is due to the fact that the actuators close to the corners are interfering with one another, forcing the jets away from the truck into the free stream and thus increasing the (local) drag.

Another, possibly more important, factor is the orientation of the jets. An inclination of the jets towards the axis of the truck should in every case be beneficial. This was impossible to implement using them as add-ons on a small-scale model. Additionally, the length of the attached bodies/flaps should be optimized with respect to the formation of the streamwise vortices.

It seems that the structure of the wake behind the lower part of the trailer has a significant impact on the overall performance of the drag-reduction system. The investigated flap configurations generated significantly different results concerning effectiveness. Therefore detailed visualization studies of any modification are necessary for better understanding of the near wake and optimization of added bodies and active flow control.

In general, actuators providing streamwise vortices in the wake of a truck by oscillatory jets seem to be promising for reducing its drag, especially when the simplicity and robustness of the investigated actuators is considered.

In view of the preliminary nature of this experiment and the lack of any optimization, these results are quite promising. The interaction with the stationary "ground" surface has to be considered, proper flow diagnostics have to be used and finally the construction of actuators that are embedded conformally in the surface should be undertaken.

References

[1] Raman G and Raghu S **(2004) Cavity Resonance Suppression Using Miniature Fluidic Oscillators.** AAIA Journal ,Vol. 42, No. 11

[2] Cooper K (1985) The Effect of Front-Edge Rounding and Rear-Edge Shaping on the Aerodynamic Drag of Bluff Vehicles in Ground Proximity. SAE paper No. 850288

[3] Storms B, Satran D, Heineck J and Walker S (2004) A Study of Reynolds Number Effects and Drag-Reduction Concepts on a Generic Tractor-Trailer. AIAA paper No. 2004-2251

[4] Englar RJ (2004) Pneumatic Heavy Vehicle Aerodynamic Drag Reduction, Safety Enhancement, and Performance Improvement. In: McCallen R, Browand F, Ross J (eds.) The Aerodynamics of Heavy Vehicles:Trucks, Buses and Trains, Lecture Notes in Applied and Computational Mechanics, Springer-Verlag, Heidelberg

[5] Coon J and Visser K. (2004) Drag Reduction of a Tractor-Trailer Using Planar, Non-Ventilated Cavities. In: McCallen R, Browand F, Ross J (eds.) The Aerodynamics of Heavy Vehicles:Trucks, Buses and Trains, Lecture Notes in Applied and Computational Mechanics, Springer-Verlag, Heidelberg

[6] Hsu T-Y, Hammache M and Browand F (2004) Base Flaps and Oscillatory Perturbations to Decrease Base Drag. In: McCallen R, Browand F, Ross J (eds.) The Aerodynamics of Heavy Vehicles:Trucks, Buses and Trains, Lecture Notes in Applied and Computational Mechanics, Springer-Verlag, Heidelberg

Large Trucks Drag Reduction using Active Flow Control

Seifert A., Stalnov O., Sperber D., Arwatz G., Palei V., David S., Dayan I. and Fono I.

The Meadow Aerodynamics laboratory, School of Mech. Eng., Faculty of Engineering, Tel Aviv University, ISRAEL

Abstract Aerodynamic drag is the cause for more than two-thirds of the fuel consumption of large trucks at highway speeds. Due to functionality considerations, the aerodynamic efficiency of the aft-regions of large trucks was traditionally sacrificed. This leads to massively separated flow at the lee-side of truck-trailers, with an associated drag penalty of at least a third of the total aerodynamic drag. Active Flow Control (AFC), the capability to alter the flow behavior using unsteady, localized energy injection, can very effectively delay boundary layer separation. By attaching a compact and relatively inexpensive "add-on" AFC device to the back side of truck-trailers (or by modifying it when possible) the flow separating from it could be redirected to turn into the lee-side of the truck, increasing the back pressure, thus significantly reducing drag. A comprehensive and aggressive research plan that combines actuator development, computational fluid dynamics and bench-top as well as wind tunnel experiments was performed. The research uses an array of 15 newly developed Suction and Oscillatory Blowing actuators housed inside a circular cylinder attached to the aft edges of a generic 2D truck model. Preliminary results indicate a net drag reduction of 10% or more.

1. Scientific background

Active flow control (AFC) is a fast-growing, multidisciplinary science and technology thrust aimed at altering a natural flow state into a more desired flow state (or path). Flow control was simultaneously introduced with the boundary layer concept by Prandtl [1] at the turn of the 20th century. In the period leading to and during WW II, as well as in the Cold War era, flow control was extensively studied and applied mainly to military fluid related systems. Though the fluid mechanics aspect can be robust, steady-state flow control methods were proven to be of inherently marginal power efficiency, and therefore limited the implementation

of the resulting systems. Unsteady flow control using periodic excitation and utilizing flow instability phenomena (such as the control of flow separation [2]) has the potential of overcoming the efficiency barrier. Separation control using periodic excitation at a reduced frequency of the same order, but higher than the natural vortex shedding frequency of bluff bodies (such as an airfoil in post-stall or a circular cylinder), can save 90% to 99% of the momentum required to obtain similar gains in performance compared to the classical method of steady tangential blowing [2]. The feasibility of increasing the efficiency and simplifying fluid related systems (e.g., for high-lift, [3-4]) is very appealing. This becomes even more appealing if one considers that *1% saving* in the fuel consumption of the US fleet of large trucks (about 8 million trucks in 2004, [5]) is worth about *$1.5 Billion per year*, while the environmental and political effects are difficult to quantify. The progress in miniaturization, actuators, sensors, simulation techniques and system integration enables the utilization of wide bandwidth unsteady flow control methods in a closed-loop AFC (CLAFC) manner. See Collis et al. [6] for a comprehensive review of the subject. Experimental demonstrations are required to close the gap between the current theoretical understanding, the computational capabilities and real-world problems. The described study brings together AFC expertise, specifically actuator development and implementation for separation control, closer to real-life industrial applications.

The essential ingredients of an active separation control system, packaged as an "add-on" device that will be attached to the rear-end of large truck trailers, in order to reduce the aerodynamic drag by about 20-30% were recently completed and will be presented in the following sections. At highway speeds, the aerodynamic drag is responsible for roughly 65% of the fuel consumption, making the potential fuel saving about 15-20%. There has been considerable effort in the US to reduce the fuel consumption of trucks using shape changes, simple add-on devices and steady state AFC methods [7], but those have inherent limitations and can lead to only half the expected benefit of our suggested method. Hsu et al. [7] cite several research efforts focused on truck-trailer drag reduction. Adjustable inclination flat plates could be attached at the truck lee-side. These could reduce drag but are rather large, heavy and expensive. Their size raises functionality and compatibility issues. Periodic excitation was also mentioned in [7] but that research effort did not progress far. Steady blowing [8] was also applied to a modified aft-region of a truck-trailer and resulted in significant aerodynamic drag reduction, but at a marginal to zero or mostly negative energy efficiency due to reasons identified already by our research group [2]. It is expected, and substantiated by preliminary CFD analysis and experimental efforts already performed [9, 10], that the combination of steady suction and pulsed blowing could overcome the above identified efficiency barrier.

The current study is aimed at applying active flow control (AFC) technology as an "add-on" device attached to the aft-body of heavy-trucks and tractor-trailer configurations. The TAU-developed Suction and Oscillatory Blowing (SaOB) AFC actuators are used for drag reduction of heavy ground transportation systems. The above fluidic device is a combination of an ejector (jet-pump) and a bi-stable fluidic amplifier that was recently thoroughly studied and published [11, 12]. The

study is assisted by computational fluid dynamics (CFD) effort to narrow the huge parameter space. After completing the actuator development and adaptation to the speed range relevant to trucks, three stages of experiments were performed on a circular cylinder, the generic bluff-body [9, 10]. These studies resulted in a significant reduction of drag due to delay of boundary layer separation. A wide range of boundary conditions were tested and only the common results to all conditions were considered as valid. Successful wind tunnel demonstration on a two-dimensional (2D) equivalent of a blunt truck-trailer model was subsequently performed and is the main subject of the current paper. This stage is to be followed by a complete, small-scale, truck model with drag reducing devices and a full scale prototype of the "add-on" device for road testing will follow. The technology could lead to a revolutionary aerodynamic drag reduction of heavy road vehicles and could lead to new efficiency levels of aeronautical systems as well. The current research is especially appealing since it provides a valuable contribution to a slower production of "Green house" gases.

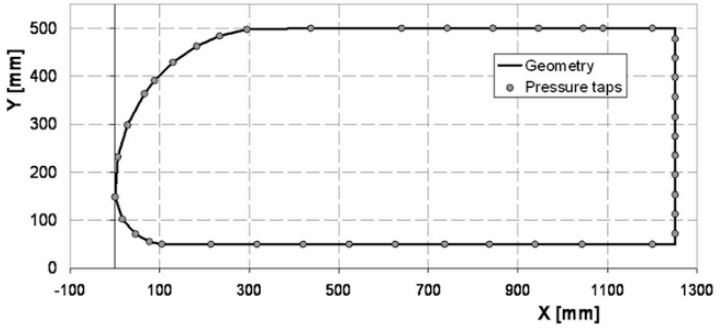

Fig. 1 A cross section of the 2D "truck" model, H=450mm, L=1250mm and its width, b=609mm. No control cylinders. Y=0 is the simulated road level, when present.

2. Description of the experiment

The experiments were performed on a generic 2D equivalent model of a large truck, along the lines of the GTS model [13]. Figure 1 shows a cross section of the model, showing also the location of the 43 pressure taps. The model height (H) is 450mm and its length is 1250mm. It spans the entire width of the wind tunnel test section, b=609mm. The model is made of aluminum beams and ribs and a skin of 2mm thick aluminum plates. The significant interference with the wind tunnel has not been taken into account in any manner. However, during the 2D truck experiments the ceiling static pressures were measured and could be used for evaluation of the wind tunnel interference with the use of future CFD effort. It is argued that since the flow accelerates more around our model, with respect to free flow conditions, the AFC results are conservative since the AFC effects are proportional to the flow linear momentum at the separation points. For control purposes, one or

two circular cylinders were attached to the aft region of the truck model. The cylinders were 76.2mm diameter and spanned the 609mm of the wind tunnel. The cylinders were installed such that were tangent to the aft body corners and extended one radius behind the aft plate line, their centers one radius below the upper cover plate or above the lower cover plate (see Fig. 7a with only the upper control cylinder sketched). The upper control cylinder was installed with an array of 15 SaOB actuators, as described in [9, 10]. An array of 96 suction holes with diameter of 2mm and spacing of 6mm were drilled in the cylinder. The wall thickness was close to 10mm, so the flow resistance was high. The flow was sucked into the cylinder by the ejector that is part of the SaOB actuator. The entire flow rate (the sum of the inlet and entrained-sucked flow) was ejected alternately out of two tangential, 1.7mm high, pulsed blowing slots connected to each actuator. Each actuator was 28mm wide and it controlled about 40 mm of the span of the cylinder. The lower control cylinder was used only for steady suction and was connected to an external suction pump. It had two staggered rows of 96 holes 2mm diameter each, spaced 7.5 deg apart along the cylinder arc (Figs. 10a and 10b).

A simulated road was placed under the 2D truck in some of the tests. The plate, with rounded leading edge positioned 67 cm upstream of the model, was 280 cm long, 4 mm thick, and extended 90 cm behind the model. A 3D wake rake was positioned 120 cm downstream of the model. It measured 29 total pressures and 2 static pressures, one close to each side-wall. The wake rake was mounted on a Y-axis traverse allowing vertical motion, with typical grid resolution or 20-25mm in the wake scans.

The experiments were performed in the Meadow-Knapp low-speed wind tunnel. The speed range is 4-60m/s, the turbulence level is about 0.1% and the test section dimensions are 1.5m (high) by 0.61m (wide) and 4.25m long. Pressures were measured by a PSI Inc. pressure scanner with 128 ports at a resolution of 0.001psi. Tunnel dynamic pressure was measured by a Pitot-Prandtl tube, positioned 110cm upstream of the model leading edge on the tunnel ceiling, connected to a Mensor pressure transducer (10” water full scale and resolution of 0.06%). The Reynolds number was monitored to 1% tolerance and dynamic pressures were also measured on the model aft region, to identify unsteady effects. The tunnel temperature was 24±2ºC. Air density and viscosity were calculated using standard formulae and the ambient temperature and pressure.

3. A brief review of recent related work

3.1 Suction and Oscillatory Blowing (SaOB) Actuator

The development of the SaOB actuator [11, 12] and its utilization for drag reduction on the circular cylinder (currently used as the aft-upper control device), were reported elsewhere [9, 10]. However, for the sake of completeness and due to the time-lag until these studies would become publicly available, some of the results are cited and discussed here.

The Tel Aviv University (TAU) suction and oscillatory blowing (SaOB) actuator was invented in October 2003, patented [14] and recently completed a two year study. Several size actuators were developed. A theoretical model for the valve operation was validated [11, 12]. Small size devices, suited for the current application with minor adjustments, were also developed and validated [9, 10]. A cross-section of the actuator can be seen in Fig. 2a and a sketch explaining the principle of operation is shown in Figs. 2b and 2c. The actuator is a combination of a bi-stable fluidic oscillator connected downstream of an ejector ("jet pump"). The purpose of the ejector is to create a suction flow, by increasing the flow entrained into the valve. Suction is probably the most efficient flow separation control method [15], but is difficult to generate efficiently. It has been shown that the ejector is indeed increasing the flow rate by a factor up to three with its entrances unrestricted. To create self-oscillations, the two control ports (Figs. 2a and 2c) were connected by a short tube, without any moving part or energy expenditure. The tube was later replaced by an S-shaped channel machined in a plate on which all the actuators were installed (referred hereafter as "mounting plate"). The SaOB actuator has a wide and appropriate frequency range (0.1 to 1.4 kHz) depending on the nozzle shape, the length of the feedback tube and the inlet flow-rate [11, 12]. Near-sonic actuator exit velocities have been measured, but currently the exit velocities are of the same order as the free-stream velocities. The inlet flow rate is controlled by a pressure regulator connected to shop air supply, to be replaced by the truck pneumatic system, by flow extracted from the truck turbocharger or by an auxiliary system connected electrically or mechanically to the rear wheels. The valve operation is insensitive to rain or dust conditions.

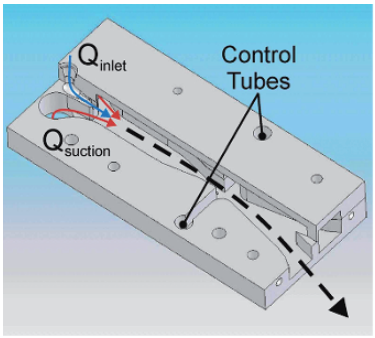

Fig. 2a Small size suction and oscillatory blowing actuator. Overall length is about 60mm

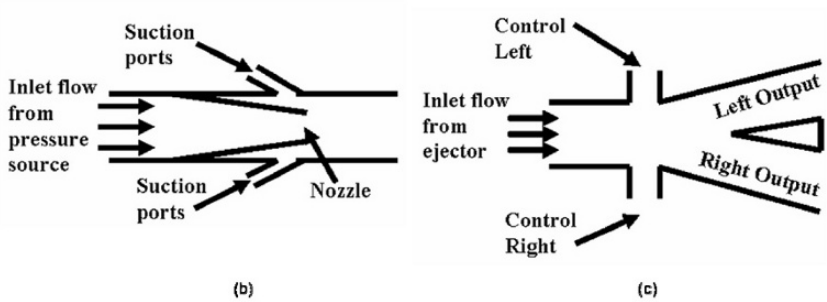

Fig. 2b,c A schematic rendering of the SaOB actuator: (b) ejector (c)

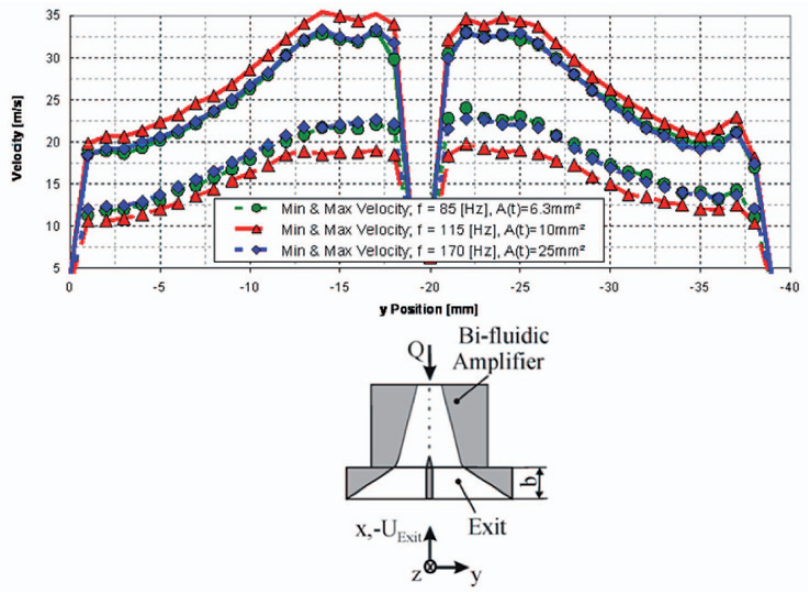

Fig. 3 Valve exit velocity profiles for three different tube diameters (maximum velocity = solid lines; minimum velocity = dashed lines; $p_{(inlet)}$=6 [psi]) measured with Hot-Wire-Anemometry; (right) Slot configuration drafted. Length of control tube, 80mm

During the course of the study reported in [9, 10], there were several cycles of modifications to the valve design. The main objective was to fit the valve into the cylinder while minimizing the pressure drop across it. This was achieved by redesigning the ejector nozzle to have a short converging-straight geometry and shortening the mixing chamber between the ejector and the oscillator to the minimum possible (Fig. 2a).

Following these modifications the valve was bench-top tested, initially only with exit restrictions, simulating the assembly in the control cylinder. Figure 3 shows the maximum and minimum flow velocity out of a single SaOB actuator with an exit assembly simulating the conditions that will prevail in the "add-on" device as well as in the control cylinder at half scale. The exit velocities were measured by a hot wire that was traversed along the exit slot. The cross section of the feedback tubes (all with L=80mm) was altered during those tests. It can be seen that the cross section of the feedback tube has a strong effect on the oscillation frequency. It has a weaker effect on the switching quality, defined as: $\kappa = \frac{U_{\max} - U_{\min}}{U_{average}}$.

3.2 Circular Cylinder with the SaOB Actuator Array

The 15 valve array was mounted on a plate, providing inlet pressure to all the valves, feedback for each valve self-oscillation and synchronization tubes between the valves. The cross section of the feedback tubes was 5.7mm^2 and their length was maintained at 80mm. The reader is referred to [9, 10] for more details. Figure 4 shows the velocity (a) and frequency (b) of oscillation of an actuator array installed in the circular cylinder and tested on the bench-top set-up. The valves were not all synchronized, the frequencies of the central 13 valves deviated by no more than 10% and the peak velocities deviated by a maximum of 20%. These results deemed sufficient to go ahead and test the valve array for the purpose of the cylinder and later the 2D truck model drag reduction while it is planned to continue improving the uniformity of the magnitude and frequency and the synchronization between the different valves.

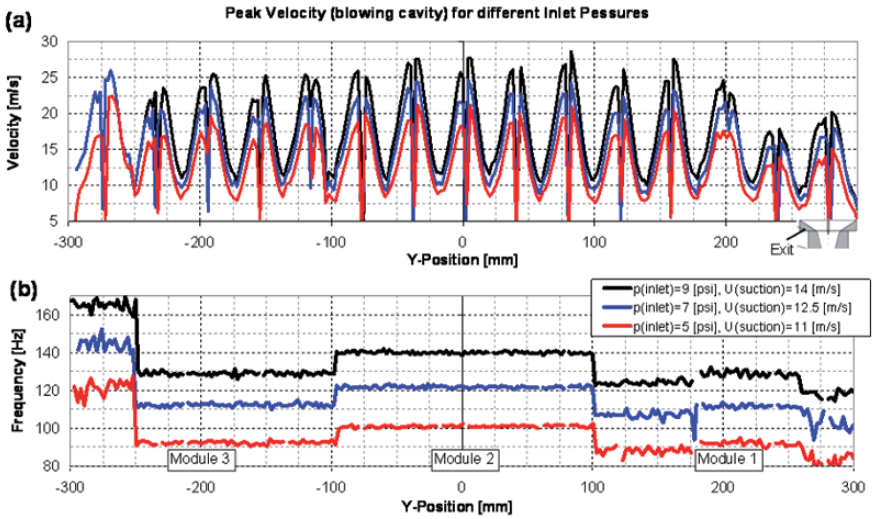

Fig. 4 Measurement of the output of a 14-valves array installed in a circular cylinder. (a) velocity, (b) frequency

The combination of oscillatory blowing and steady suction has never been tested before this project, but both methods are known to be very effective for the control of boundary layer separation [15]. A significant body of knowledge has been acquired by [9, 10]. These experiments established the drag reducing capability of steady suction through a 2D slot and later an array of holes in a wide range of boundary conditions. The data set also established that a 15 deg delay in separation region on the circular cylinder at Re=100,000 and Re=150,000 (associated with the target highway driving speeds) is possible with suction magnitude of about half the free-stream velocity. This enabled the definition of the configuration shown on the right side of Fig. 5. The suction holes are located 15 deg upstream of the pulsed blowing slot. The array of 15 SaOB actuators is mounted inside the 76.2mm diameter cylinder. Inlet flow is provided via common channel feeding all the ejectors' jets. These create low pressure in the half cylinder to the left of the valve-array, sucking flow through the holes. The entire flow is then ejected through the pulsed-blowing exit slots. The oscillation frequencies are in most cases larger than the natural vortex shedding frequencies on a circular cylinder at the current velocity range and significantly higher than the truck vortex shedding frequency.

Three series of wind tunnel experiments were performed on the circular cylinder (shown in Fig. 5, [9, 10]).

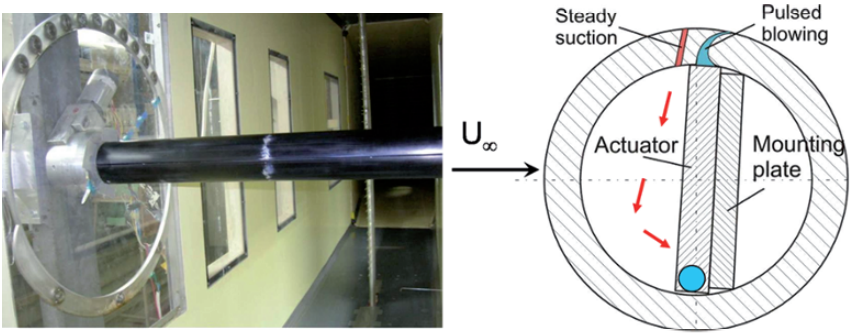

Fig. 5 The cylinder Setup with the suction holes (red) and the tangential slot (light blue) installed at the Meadow-Knapp Wind Tunnel (left), and a sketch of the experimental setup with the array of 15 SaOB actuators installed in the cylinder, the mounting plate for synchronization and pressure supply (right, light blue circle). The arrows indicate the path of the suction flow.

Figure 5 shows the experimental set-up of the cylinder in the Meadow-Knapp wind tunnel and a cross section of the 15-valves actuator array as installed inside the cylinder.

The cylinder was tested and a sample of the drag reduction data is presented in Figure 6 below.

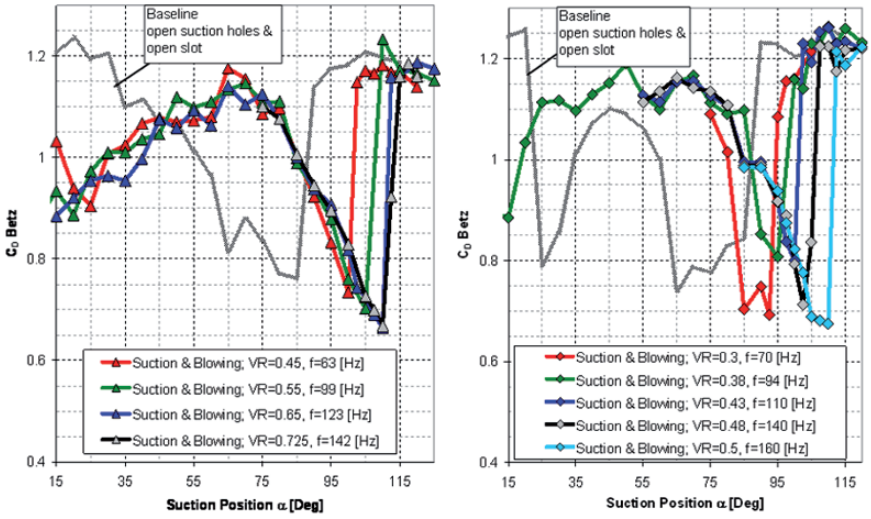

Fig. 6 Cylinder drag coefficient (C_D Betz – wake rake survey with static pressure correction) versus Suction Position (0 deg is the summit of the cylinder) in "free" (no truck model) laminar flow conditions; measured with Steady Suction and Oscillatory Blowing Actuation for two Reynolds numbers and different amplitudes (left) Re_d=100k (right) Re_d=150, blowing cavity is located $\Delta\alpha$=15 Deg downstream to the suction holes. VR is the velocity ratio between the suction and free-stream velocities.

The data shown in Fig. 6 indicates a drag reduction from about 1.1 to about 0.7, or a relative drag reduction of about 35%. This is obtained when the suction holes

are located at about 110 deg (relative to the free-stream direction) on the cylinder and the pulsed blowing slot at are positioned 15 deg downstream (at about 125 deg), where 90 deg is the summit of the cylinder. The energy efficiency of this drag saving, which was measured at flow velocity comparable to the highway speed of trucks indicates net positive energetic efficiency [9, 10]. For the acquisition of all the data presented below, net energy efficiency was the prime consideration. As shown in Fig. 7a, the add-on device will have a shape that resembles a -semi- to quarter-cylinder attached to the back side of truck-trailer. The advantage of having a complete cylinder at this stage of the study is the capability to conveniently alter the actuation location, which is shown to be very sensitive on the "free" cylinder (Fig. 6) and also in the "truck" results to be presented later in the paper.

3. Two dimensional (2D) truck experiments

3.1 Two dimensional (2D) truck with SaOB cylinder at upper- aft corner

Figure 7a shows a schematic cross-section of the 2D truck model, with the SaOB cylinder installed on its back-upper corner. Figures 7b and 7c present pictures of the model installed in the Meadow-Knapp wind tunnel, above a simulated road. The vertical distance between the model and the floor was allowed to increase from 50 to 55mm in order to compensate for boundary layer growth. It was validated that the boundary layers did not restrict the free-flow under the model. Wheels or moving floor were not used. These effects seem secondary since most of the effort was spent on the upper aft corner, least effected by the wheels or simulated road, moving or stationary. However, the mere presence of the simulated road is essential for simulating a side-view of the truck driving on a road. Several 50mm wide roughness strips (grit #60) were placed on the top and bottom plates of the truck model, to reduce Reynolds number effects. Figure 7d presents a close-up view of the cylinder. An array of 96 holes with 2mm diameter was positioned 15 deg upstream of a 1.7 mm (nominally) wide slot. The slots allowed almost tangential-downstream directed introduction of the pulsed blowing excitation. Each actuator controlled a span of about 40mm with two exits, as shown schematically in Fig. 3 (insert). The trailing-edge of the top and bottom cover plates were machined to create a back-step no thicker than 0.5mm, allowing a smooth transition of the flow from the covers to the cylinders.

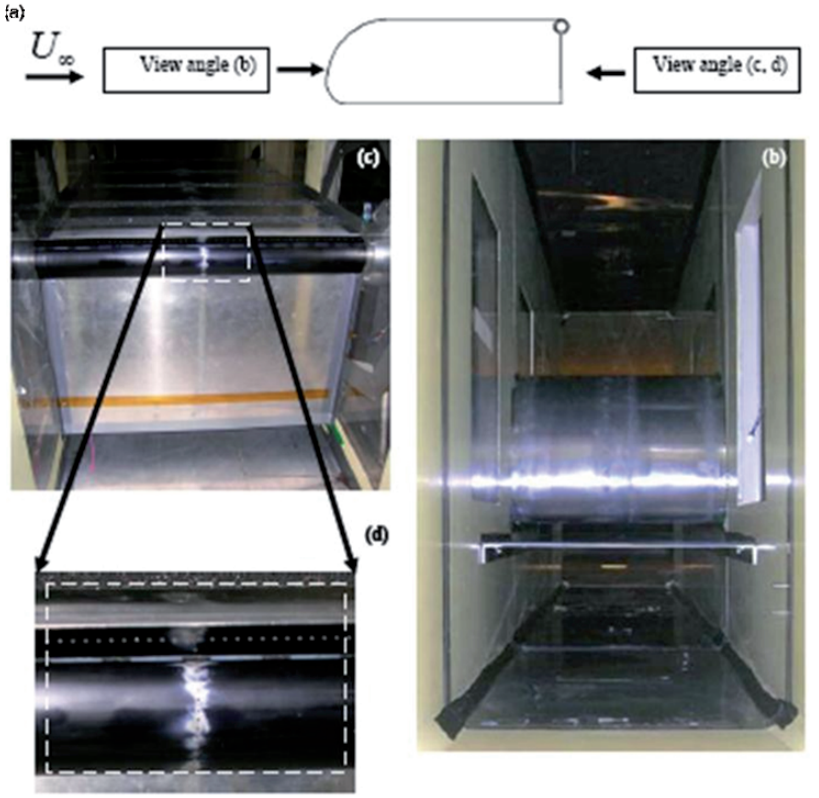

Fig. 7 The 2D truck model: (a) cross section (flow is coming from left to right); (b) front view showing the model installed in the tunnel 50-55mm above the simulated road; (c) a rear view showing the back plate and SaOB instrumented cylinder on the top-rear edge; and (d) close-up of the row of 96, 2mm suction holes and 1.7mm wide pulsed blowing slot on the cylinder (that was allowed to rotate for optimal actuation locations).

Of major importance was the determination of the optimal holes/slot location. Note that at this stage of the investigation the angular distance between the suction holes and pulsed blowing slots was fixed, 15 deg, based on the results of [9, 10].

The drag of the 2D truck model was calculated from the integration of the pressures around the model and from a 3D wake survey performed 1.2m behind the model. The wake flow was found to be quite 2D and the agreement between the two methods of drag evaluation was better than 2%, in most cases and in the absence of the simulated road. The drag reduction magnitudes were similar when evaluated either with the wake integration method or from the pressure drag. The aft-body "add-on" device was tested as a circular cylinder, due to the larger size and ease of installation of the 15 SaOB valve array inside it. A secondary major consideration was the capability to rotate the cylinder, bringing the holes/slot to an optimal location.

Figure 8a shows the form-drag of the 2D truck model with the SaOB cylinder installed at the upper-aft corner. The addition of the passive control cylinder at the aft-upper corner had a drag reducing effect of about 5% with respect to the baseline configuration shown in Fig. 1. The slot was just exposed when its location was 90 deg. With the control cylinder present but when the slot was hidden, Cdp=0.99±0.01. The passive effect of the slot, and its associated discontinuity, can be seen by the drag increase between 85 and 105 deg. At larger slot locations the drag returns to its undisturbed value, with a possible drag penalty of 0.01-0.02. At slot positions greater than 105 deg both slot and suction holes are open. Also shown on Fig. 8a are results of different levels of control applied by the array of SaOB actuators, with increasing level of input pressures, as indicated in the legend. A significant drag reduction develops in the range of tested pressures, up to 0.5Bar. An optimal holes/slot location can be identified around 130-132.5 deg, slightly increasing with the magnitude of the control authority. These results were obtained with a simulated road, similar to a truck with control applied only from the top-aft edge. It was later found that adding a second control cylinder at the lower-aft edge, *with simulated road* did not provide additional drag-reducing effect.

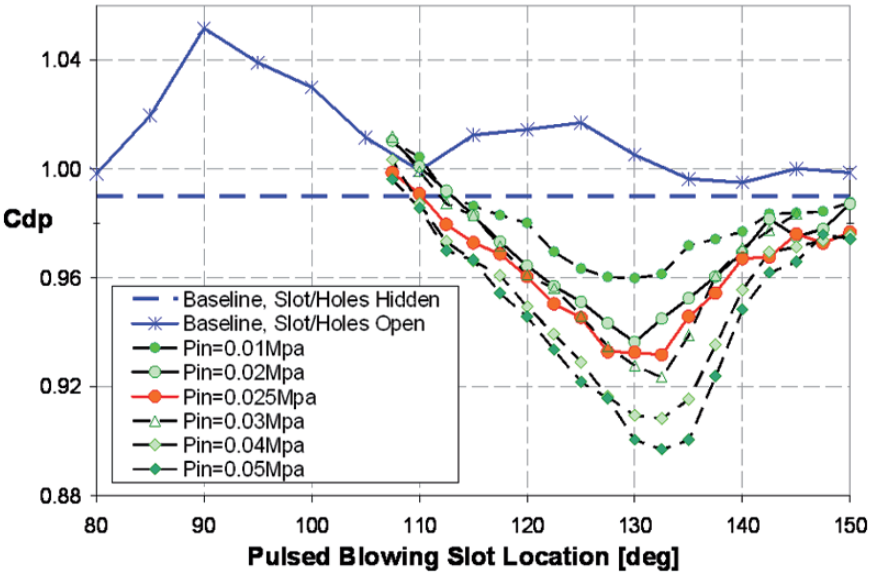

Fig. 8a The effect of the SaOB actuation on the drag of the 2D truck model at U=25m/s for different actuation levels indicated by the inlet pressures. The actuation location is altered via cylinder rotation, where 90 deg is the cylinder – upper plate junction.

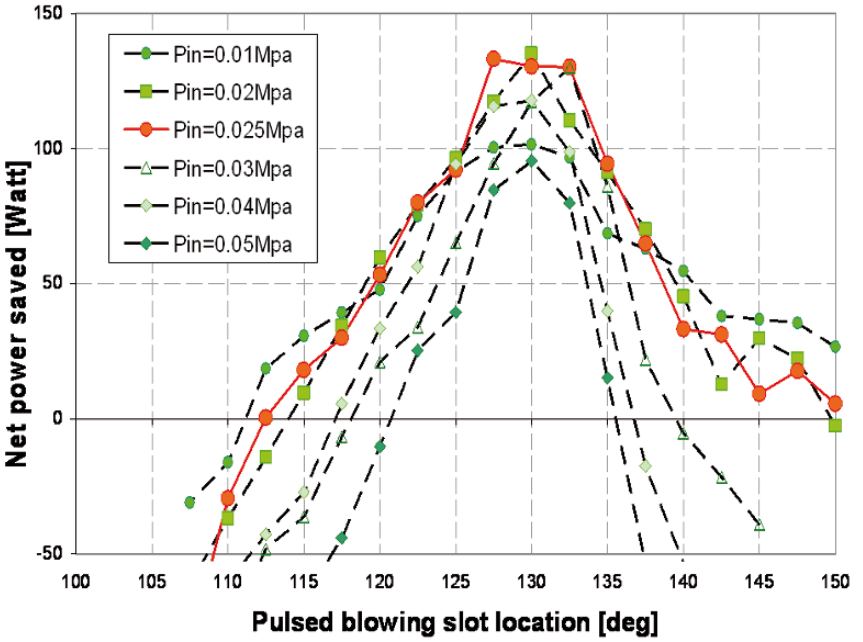

Fig. 8b The effect of the SaOB actuation on the required power to propel the 2D truck model at U=25m/s for different actuation levels indicated by the inlet pressures. The actuation location is altered via cylinder rotation, where 90 deg is the cylinder – upper plate junction. Reference power is about 2.57kWatt.

Despite the apparent capability of increased levels of inlet pressure to provide further drag reduction, one should consider the energy cost of the control input, since our aim is a reduction in *fuel consumption* and therefore total invested power should be a prime consideration. The net power saving was calculated according to: $Power\ saved = 0.5\rho U_\infty^3 S\Delta C_d - P_i Q_i/\eta$. Where ρ is the air density, U_∞=25m/s is the free-stream velocity, S=0.61x0.45m^2 is the 2D truck cross-section area, ΔC_d is the drag reduction at the same holes/slot position with respect to the baseline uncontrolled condition. The control power was taken as the product of the inlet pressure (*Pi*, measured at the supply line) and the inlet flow rate (*Qi*, measured by an orifice flow meter at the pressure regulator and neglecting the effect of the larger static pressure on the flow rate, making the actual flow rates smaller by 5-20% than those currently cited depending on the excess pressure). The pumping efficiency, η, was taken as 75%, as is in many common low-pressure compressors. In reality the control flow was provided by the lab shop air through a computer controlled pressure regulator. The data presented in Fig. 8b shows a rather insensitive (to the inlet pressure) peak power saving of around 130 watts for inlet pressures of 0.02-0.025MPa. With either lower or higher pressure levels, the power efficiency decreases.

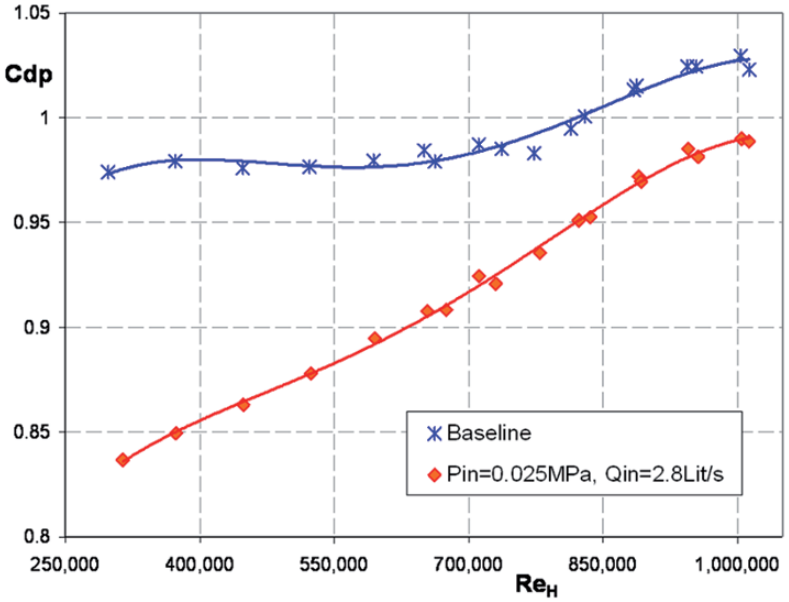

Fig. 9a The effect of the SaOB actuation on the baseline and controlled drag of the 2D truck model vs. the height Reynolds numbers for fixed actuation level. The actuation location is: pulsed blowing slot at α=130°, suction holes at α=115°, Pin=0.025 MPa, Qin=2.8 Lit/s where 90 deg is the cylinder – upper plate junction.

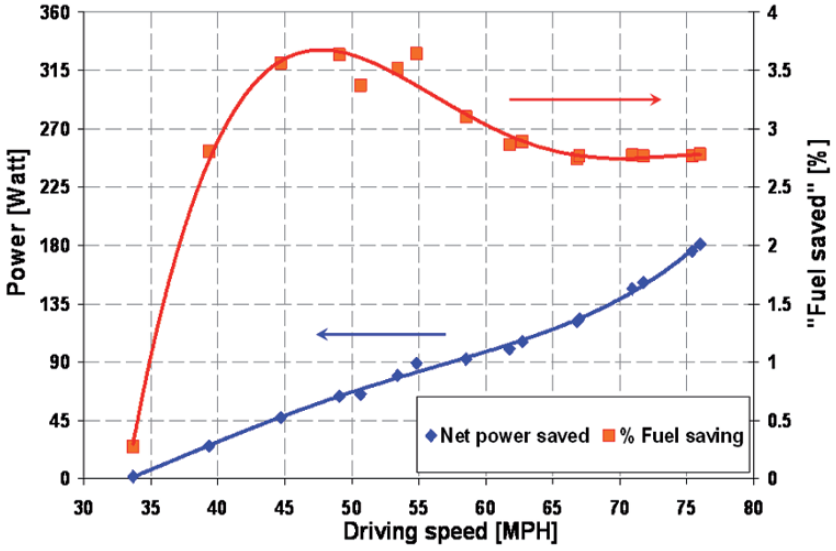

Fig. 9b The net flow power saved and equivalent "fuel" saving of the controlled 2D truck model vs. the driving speed for fixed actuation level. The actuation location is: pulsed blowing slot at α=130°, suction holes at α=115°, Pin=0.025MPa, Qin=2.8 Lit/s where 90 deg is the cylinder – upper plate junction. Same Re range as Fig. 9a.

While the data presented in Figs. 8a & b was obtained at a fixed free-stream velocity of 25m/s, it is important to evaluate the effectiveness of the drag reducing technology over the entire range of free-stream velocities, or driving speeds. Furthermore, this was done with one actuation condition, allowing the system just to be turned-on or off with no proportional control, for simplicity. Figure 9a presents form-drag data for the 2D truck model, with one upper control cylinder, the SaOB array installed on the upper-aft edge of the 2D truck model (as shown in Fig. 7a). Simulated road was present in this experiment. The drag slightly increases, from 0.98 to 1.02 with Re (based on the model height and the free-stream velocity) increasing from about 200,000 to about 1,000,000. Note that at the larger Re range the drag reaches a plateau. This Re, based on the height of the model, is considered minimal for Reynolds number free results. With fixed level of inlet pressure and fixed actuation locations, as indicated in the legend and caption of Fig. 9a, one can clearly note a significant drag reduction over the entire Re range. It is only natural to expect that the magnitude of the drag reduction will decrease as Re increases, due to the relative decrease between both the suction and pulsed blowing magnitudes when normalized by the free-stream velocity. Clearly aerodynamic drag reduction of about 20% is possible at low speeds, decreasing to about 5% at the highest speeds considered operational and legal for large trucks in the US highway system.

While the drag reduction is of interest, the power efficiency is our prime motivation. Figure 9b shows the net power saved and the percentage of net power saving. The latter is equivalent to about twice the expected fuel saving after considering friction resistance and wind averaged performance.

One can note a 45Watts power saving at 45MPH increasing to 180 watts saved at 75MPH. These power savings translate to more than 3.5% power saving at speeds between 45 and 55 MPH. At larger speeds the aerodynamic power saving (taking into account the invested power in the actuation system) saturates at about 2.8%. Considering that at these speeds (above 60 MPH) two thirds of the power is invested in overcoming aerodynamic drag, the equivalent net fuel savings is about 1.9%. While these numbers might appear small, they are still significant. The inlet pressure was optimal at about 50 MPH, so larger control authority would shift that peak to higher speeds, depending on the target speed range. Furthermore, the obtainable drag reduction due to the application of the control on the upper-aft edge with the simulated road present is smaller compared to its application on the sides of the truck, as will become clear from the subsequent discussion.

3.2 Two-dimensional truck with two control cylinders

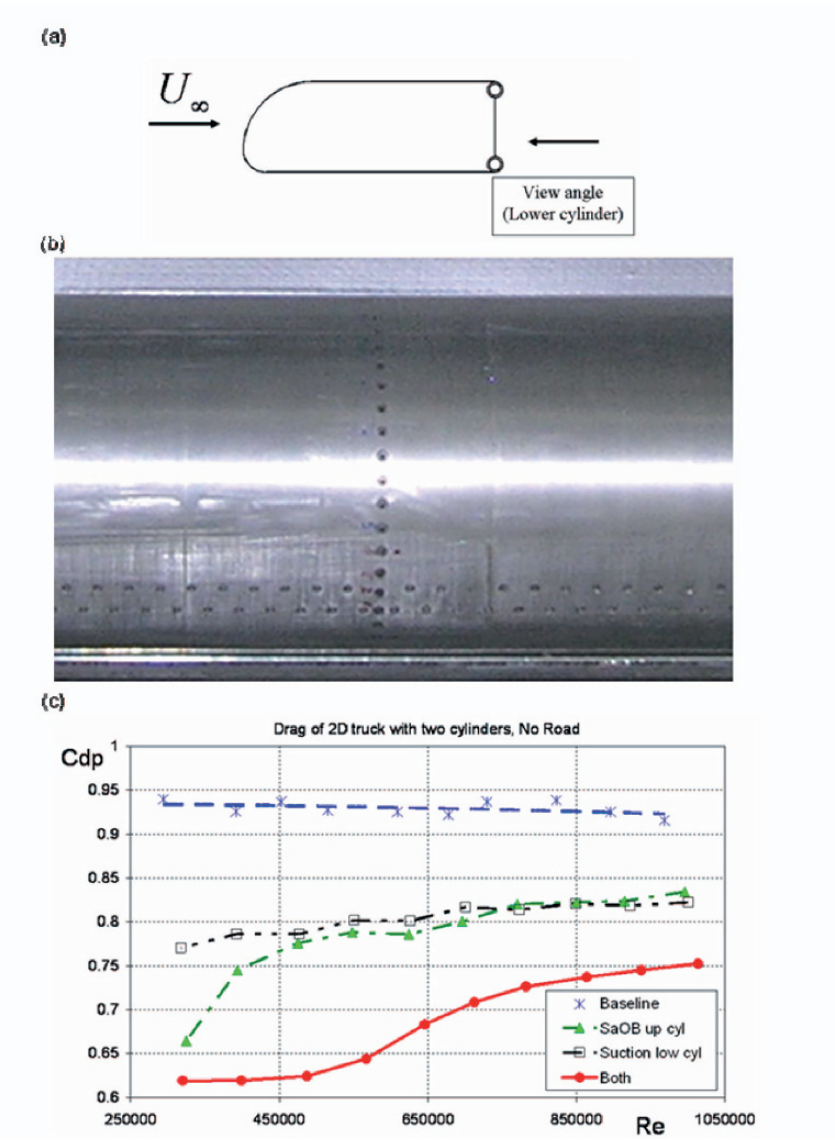

Fig. 10 (a) A sketch of the 2D truck model with two control cylinders, (b) a close-up rear-view of the lower aft-corner control cylinder, and (c) drag reduction due to SaOB array on top aft, Suction cylinder on bottom aft corners.(c) The actuation location is: pulsed blowing slot at α=130°, suction holes at α=115°, Pin=0.04 MPa, where 90 deg is the cylinder summit. Lower cylinder: two rows of suction holes, the 1st at α=-121°, the second at α=128.5°. Lower cylinder suction provides the same drag reduction as the SaOB array alone at Re~800,000. (c) Form drag coefficient vs. Reynolds number for four states: baseline, only the upper SaOB cylinder is turn on, only the lower suction cylinder is on, and both the cylinders are on.

To asses the effectiveness of controlling both vertical sides of the aft truck trailer, the simulated road was removed and a second control cylinder was mounted on the lower-aft edge of the 2D truck model, as shown in Fig. 10a. The lower control cylinder was also mounted on a rotary system to allow optimal control locations. However, for simplicity, cost and time considerations only steady suction was applied for the lower control cylinder. It should be noted that suction only (lower cylinder) is not as effective as SaOB valves (upper cylinder). Detailed comparison of the effectiveness of the two control methods (with suction only and with the SaOB valve array) can be found in [9, 10]. The suction was applied from two rows of staggered 2mm diameter holes, each containing 96 holes and spaced 7.5 deg in their angular locations (seen in Fig. 10b). The lower suction holes were just exposed for holes location of -90 deg. The same optimization procedure was applied to the lower cylinder in order to identify a condition which provides the same level of drag reduction that the upper SaOB control cylinder is capable of with inlet pressure of 0.04 MPa. This higher pressure level was selected based on the results shown in Figs. 8 and 9 and discussed above.

The data presented in Fig. 10c shows that the baseline-drag of the 2D truck model, with two control cylinders and without the simulated road is 0.93±0.01 regardless of the Reynolds number. The two control cylinders, when operated alone, can provide significant and similar drag reduction over the entire Re range, with the exception of the SaOB control that is more effective at low speeds. This difference might be associated with the oscillation frequency being somewhat low, and therefore optimal for low speeds. When the two control cylinders operate together, a very encouraging trend can be noted, i.e., that the drag reducing effects sum up. The data presented in Fig. 10c demonstrates about 20% aerodynamic drag reduction at highway speeds, translated to about 10% net fuel savings on large trucks, busses and tractor-trailer configurations.

A smaller 3D truck model with an array of SaOB actuators is currently being tested. Road tests will hopefully be conducted during the second quarter of 2008.

4. Conclusions and Recommendations

A comprehensive set of experiments were conducted with the aim of reducing the aerodynamic drag of large trucks by 20%. This effort included: (1) development, modeling and adjustment of the SaOB actuator to low-speed operation, (2) installation of a 15-valve actuator array in a circular cylinder, (3) comprehensive wind tunnel testing of the drag reduction effects on the circular cylinder under the effect of various boundary conditions, (4) the design and testing of a 2D truck model with and without simulated road, with and without control cylinders and finally (5) evaluation of the energy efficiency of control cylinder(s) drag reducing capability. Only stages (4-5) are currently discussed. Two related publications [9, 10] discuss stages (1-3).

It was found that the optimal location for introducing the suction through holes is about 15-20 deg downstream of the plate-cylinder junction. During the

cylinder alone tests it was found that suction with half the free-stream magnitude is capable of 15 deg separation delay. Therefore, the pulsed blowing was introduced 15 deg further downstream of the suction holes. One control cylinder positioned at the upper aft edge of the simulated trailer is capable of about 10% drag reduction and more. But if the power invested in the actuation is considered, the optimum is obtained at lower fluidic power input, where the aerodynamic drag reduction is roughly 6-7%. When two control cylinders were applied in a situation simulating a control applied to the two vertical edges of the aft-trailer region, 20% drag reduction is possible. This should lead to at least 10% net fuel savings.

Significant enhancement in power efficiency is expected when scale-up of the small-size model will be performed. This should originate from lower resistance of the suction holes (due to smaller wall thickness and rounded edges) and a factor of 2-4 power saving on the actuators' ejector due to the larger ejector-nozzle cross section.

Acknowledgment

The authors would like to thank S. Pastuer, E. Ben-Hamou, A. Blas, A. Kronish, S. Balvis, S. Moshel and M. Vaserman for the great technical support.
The research was funded by the Yeshaya Horowitz Fund and managed by RAMOT of Tel Aviv University. Three patents (one approved and two pending) exist.

References

[1] Prandtl L, "Motion of Fluids with Very Little Viscosity", Third International Congress of Mathematicians at Heidelberg, 1904, from Vier Abhandlungen zur Hydro-dynamik und Aerodynamik", pp. 1-8, Gottingen, 1927, NACA TM-452, March 1928.

[2] Seifert A, Darabi A and Wygnanski I, 1996, "Delay of Airfoil Stall by Periodic Excitation", J. of Aircraft. Vol. 33, No. 4, pp. 691-699.

[3] Pack Melton L, Schaeffler N, Yao C and Seifert A, "Active Control of Flow Separation from the Slat Shoulder of a Supercritical Airfoil", J. of Aircraft, 42 (5): 1142-1149 SEP-OCT 2005 (previously AIAA Paper 2002-3156).

[4] Pack Melton L, Yao C and Seifert A, "Active Control of Flow Separation from the Flap of a Supercritical Airfoil", AIAA J., 44 (1): 34-41 JAN 2006 (previously AIAA Paper 2003-4005).

[5] Traffic safety facts: large trucks, DOT HS 810 619.

[6] Collis S, Joslin R, Seifert A and Theofilis V, "Issues in active flow control: theory, simulation and experiment", Prog. Aero Sci., V40, N4-5, May-July 2004 (previously AIAA paper 2002-3277).

[7] Hsu T-Y, Hammache M & Browand F, "Base Flaps and Oscillatory Perturbations to Decrease Base Drag," Proceedings of the UEF Conference on The Aerodynamics of Heavy Vehicles:Trucks, Buses and Trains, Lecture Notes in Applied and Computational Mechanics Springer-Verlag, Heidelberg, September, 2004.

[8] Englar R, Advanced aerodynamic device to improve the performance, economics, handling and safety of heavy vehicles, SAE paper 2001-01-2072

[9] Sperber D, Dipl. Eng. Thesis, Technical University of Berlin, 2007.

[10] Sperber et al., "Drag reduction of a circular cylinder at transitional Reynolds numbers", in preparation.

[11] Arwatz G, Fono I and Seifert A, "Suction and Oscillatory Blowing Actuator", in "Proceedings of IUTAM Symposium on Flow Control and MEMS", London, Sep. 2006, Eds. Morrison, J.E., Birch, D.M. and Lavioe, P., p. 33-44, Springer 2008.

[12] Arwatz G, Fono I and Seifert A, "Suction and Oscillatory Blowing Actuator", accepted for publication, AIAA J., Nov. 2007.

[13] R McCallen, K Salari, J Ortega, L DeChant, B Hassan, C Roy, W Pointer, F Browand, M Hammache, T Hsu, A Leonard, M Rubel, P Chatalain, R Englar, J Ross, D Satran, J Heineck, S Walker, D Yaste, B Storms, "DOE's Effort to Reduce Truck Aerodynamic Drag-Joint Experiments and Computations Lead to Smart Design" AIAA paper June 2004.

[14] Seifert A, Pastuer S, "Method and mechanism for producing suction and periodic flow", US Patent 2006-0048829-A1, Granted 2005.

[15] Seifert A and Pack L, "Active Control of Separated Flow on a Wall-mounted "Hump" at High Reynolds Numbers", AIAA J., V. 40, No. 7, July, 2002, pp. 1363-1372. (Part of AIAA paper 99-3430).

Flow Separation Control on Trailing Edge Radii using Single Dielectric Barrier Discharge Plasma Actuators: An Application to Vehicle Drag Control

R. Spivey[1], R. Hewitt[2], H. Othman[2] and T. Corke[2]

[1] Mach Zero Associates, USA
[2] Center for Flow Physics and Control Aerospace and Mechanical Engineering Department, University of Notre Dame, USA

machzero@sbcglobal.net

Abstract As cruise speeds of ground vehicles has risen to as high as 70 miles per hour, overcoming the aerodynamic drag has become a significant percentage of the total power required. Engines have been increased in power and fuel tanks made larger to provide reasonable range between fuel stops. Heavy truck data in particular indicate that 2/3rds of the cruise power is needed to overcome drag. This paper focuses on reducing drag on class-8 trucks, but the principles can be applied to lighter trucks, busses, pick-ups, SUVs, and many other ground vehicles. The University of Notre Dame has developed unique actuators that have shown potential to maintain unseparated airflow around corners. This technology promises to reduce drag on ground vehicles thus increase fuel efficiency and gas mileage. This paper discusses these actuators and the preliminary wind tunnel tests that have been conducted at Notre Dame in 2007. The cost of fuel has risen so rapidly in the past few years that drag is now a major contributor to the cost of moving freight and consumer goods around the country. The use of these actuators can be applied to passenger cars and as well as many other types of ground vehicles.

Introduction

Over the past decade and a half much work has been conducted by the aerospace industry to control airflow in an effort to reduce the drag, improve handling qualities and lower the noise of aircraft. This paper applies that technology to ground vehicles. While the speed of ground vehicles is much less than that of aircraft, aerodynamics has become an important issue in today's energy-conscious world. The amount of fuel needed to move goods across the nation has risen sharply, just as the cost of that fuel has exploded. Data generated by the Department of Energy, show that 65% of the power required by a class-8 truck when cruising at 70 miles per hour is used to overcome aerodynamic drag. A significant amount of that drag is caused by (1) base drag, the air separation that occurs around the rear of the trailer; (2) gap drag, the drag associated with the area between the tractor and the trailer; and (3) the under-carriage, the area beneath the rig including the tires, the drive system and the structure that is needed to support the weight and utility of the rig.

Reducing the flow separation and momentum losses in these three areas will increase the truck's efficiency, resulting in a reduction of cruise power, fuel consumption and emissions. Figure 1 shows the truck locations where the application of Single-Dielectric Barrier Discharge Plasma Flow Control (PFC) could reduce drag.

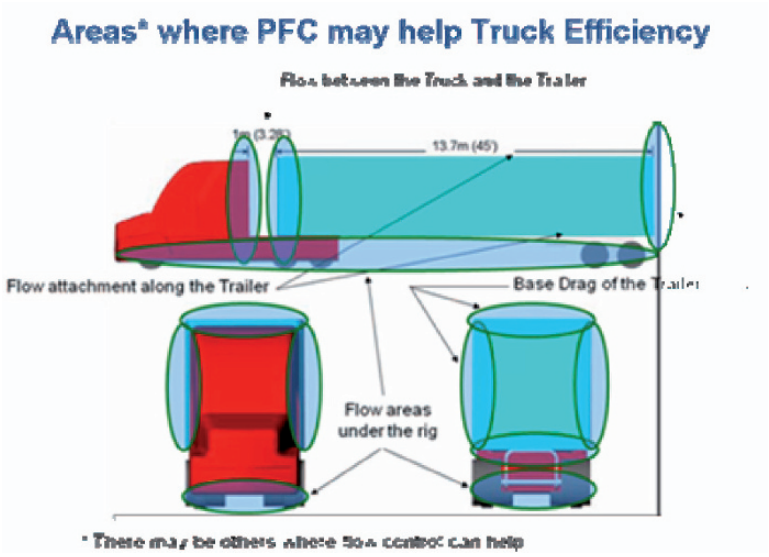

Fig. 1 Possible locations for PFC application to reduce flow separations and aerodynamic drag losses

Mach Zero Associates, a Fort Worth, Texas based, Small Business, has been working with the Department of Energy, truck and trailer manufacturing firms, truck leasing and operating companies, after-market businesses and the University

of Notre Dame to lay the groundwork to reduce this aerodynamic drag and improve the efficiency of long haul trucks. Class-8 Trucks are the large, 18-wheel vehicles that move freight around the country, fueling our commerce and providing an essential service to our nation's economy.

The University of Notre Dame's Center for Flow Physics and Control (FlowPAC) has developed the PDF actuator that has the capability of delaying flow separation around blunt objects. Test results show a 75-90% reduction in drag by incorporating two actuators on a cylindrical object causing the flow to remain attached far longer than expected (Thomas et al. [1]). These actuators use Single Dielectric Barrier Discharge (SDBD) plasma flow effects to maintain boundary layer stability, keeping the airflow attached around the cylinder, reducing the size of the wake and significantly decreasing the drag.

Figure 2 illustrates the flow around a four-inch cylinder with and without PFC application. The large wake fluctuations shown in the top photo are associated with the Von Karman vortex street that is the standard condition for cylinder wakes. In the lower photo, PFC actuators were located at the top and bottom (90° and 270° locations relative to the upstream stagnation line) of the cylinder at the flow separation locations. These effectively caused the flow over the cylinder to remain attached so that the flow pattern appears like that of an airfoil-shaped body. As expected, this transformation led to a significant drag reduction.

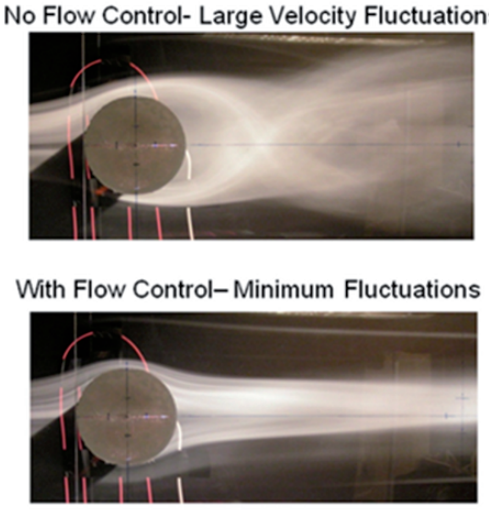

Fig. 2 Visualization records of the flow over a 4 in. cylinder at Re_D = 30,000 without (top) and with (bottom) PFC. (From Thomas et al.[1])

This paper will discuss early analyses and wind tunnel testing that was performed in an effort to determine the extent to which these actuators can reduce truck drag, thereby reducing the power required and fuel needed to move cargo throughout the country. The results are expected to lead to practical application of SDBD Plasma Actuator Flow Control (PFC) technology that is aimed at lowering the energy, emissions, power, fuel and turbulent airflow behind a class-8 truck.

Much work needs to be done, but the potential of reducing the enormous amount of carbon-based fuel that is consumed moving goods across the United States is well worth the effort.

SDBD Plasma Actuator Background

Based on the work at the University of Notre Dame Center for Flow Physics and Control (FlowPAC) over the last 15 years, much is known about the method of operation and capability of (SDBD) Plasma Flow Control (PFC). This flow control approach has been successful in a number of applications ranging from separation control, lift enhancement, drag reduction and flight control without moving surfaces [2-10]. A recent review of SDBD plasma actuators was given by Corke et al.[11].

Figure 3 illustrates the PFC actuator. It consists of two electrodes, one exposed to the air and one covered by a dielectric layer. The electrodes are supplied with an a.c. voltage that at high enough levels causes the air over the covered electrode to ionize. In the classic description, the ionized air is a "plasma", which is why these are referred to as "plasma actuators". The dielectric layer is very important to the design. The charge build-up on the dielectric prevents the discharge from collapsing into a constricted arc.

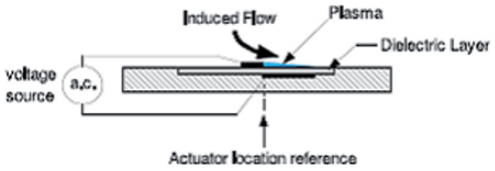

Fig.3 Plasma Flow Control actuator

The ionized air, in the presence of the electric field produced by the electrode geometry, results in a body force vector that acts on the ambient (neutrally charged) air [12, 13]. The body force is the mechanism for active aerodynamic control. If operated properly, there is very little heating of the air.

The asymmetric plasma actuator design in Fig. 3 produces a body force vector that induces a flow that is similar to that produced by a tangential wall jet. The mean velocity profile of the flow generated by this plasma actuator design is shown in Fig. 4. This accelerates the flow immediately adjacent to the wall. If applied to a separating boundary layer, it can cause the boundary layer to stabilize keeping the flow attached. Because the plasma actuator mechanism is through a body force, its effect is additive, namely N-actuators produce N-times the effect. Therefore additional actuators placed at stations downstream of a flow separation have the potential to maintain an attached flow over large distanced and sharp curvatures.

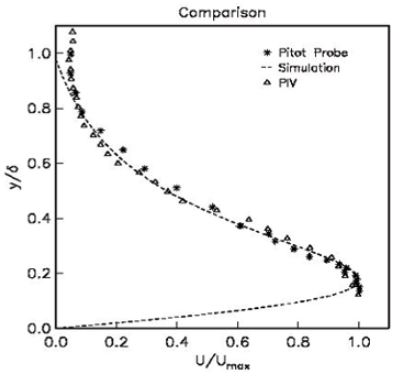

Fig. 4 Mean velocity profiles of the velocity component parallel to the wall (U) of flow induced by an asymmetric-electrode SDBD plasma actuator like that illustrated in Fig. 3 in still air. (from Post and Corke[6])

Motivation

Early analyses of using PFC on blunt bodies and airfoils have shown great promise in delaying airflow separation and reducing drag. While automobile gas mileage has increased over the years, class-8 truck mileage remains basically unchanged for almost 25 years. Much work has been done by the 21st Century Truck initiative that began in 2000, but the use of PFC has not been applied before. Most of the efforts that have been incorporated into production are passive shaping. These have been applied on the tractor but not on the trailer. There appears to be many locations on the tractor and trailer where the use of PFC can help reduce drag. In fact, if these actuators contribute as expected, redesign of both tractor and trailer may be in order. At this point in the research, most of the attention is being placed on after-market additions to existing designs to make them more fuel efficient.

From DOE documents, [14, 15] in the year 2003 the average class-8 truck used 4700 gallons of fuel while driving approximately 30,000 miles. However long haul rigs operating on the nation's freeway system averaged well over 100,000 miles. If two-thirds of that fuel was used to overcome aerodynamic drag, and based on an average diesel fuel cost of $2.50 per gallon, the fuel cost used to overcome the drag alone is approximately $30,000 per long haul truck per year. If the aft end of the truck trailer accounts for one-third of the total drag, then that drag itself contributes approximately $10,000 to the fuel cost per year per truck. The same can be said for the drag in the truck-trailer gap and the undercarriage. Any decrease in the aerodynamic drag of the tractors and trailers has the potential to greatly reduce the cost of operation, and the level of harmful emissions of the

trucks on our highways. The question at this point it is how much drag reduction can the achieved without impacting the utility of the rig.

This effort will utilize the approaches for plasma-based flow control from past experiments to design a combination of fairings and PFC actuators in strategic locations on the tractor and trailer to create more effective flow attachment and drag reduction. The overall plan is to determine the design parameters for the fairings, and the locations and strength of the actuators. Prototypes of these designs will then be built and tested in a wind tunnel at the University of Notre Dame. The most promising designs will ultimately be selected for tests at full-scale on trucks in over-the-road conditions to determine their ultimate impact and practicality.

Experimental Approach

The experiments were designed to determine the effectiveness of SDBD plasma actuators for turning flow around corners that would be representative of the aft edges of a tractor or trailer. Based on the results of the circular cylinder tests, [1] significant reduction in drag is possible if flow separations can be reduced or eliminated to allow the flow to negotiate sharp corners and fill the wake deficit region. The objective was to investigate the use of the plasma actuators to turn the flow around different radii. In order to simulate possible conditions on trucks, it was important that the boundary layer approaching the radius was turbulent. Therefore the test model consisted of a suspended flat plate of sufficient length, with a circular radius at the downstream edge. A schematic of the experimental setup is shown in Fig. 5. The flat plate setup was placed in an open return wind tunnel with a 2 foot square cross-section by 6 foot long test section.

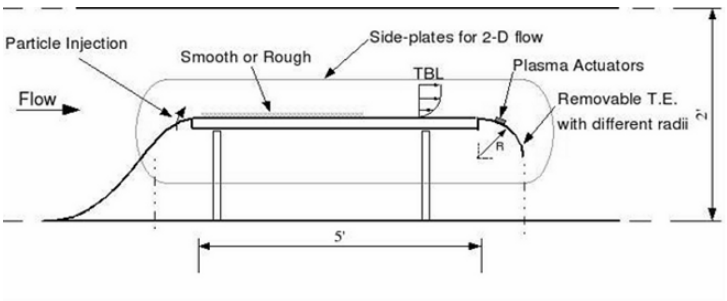

Fig. 5 Experimental setup for trailing-edge radius plasma actuator flow control.

The flat plate leading edge was located at the entrance to the test section, which was just downstream of the wind tunnel contraction. A second contraction was added to the leading edge of the plate to prevent flow from going under the plate. This was intended to better simulate a larger bluff body (like the aft end of a truck trailer). Side plates were used to limit 3-D side effects and maintain a 2-D mean flow across the spanwise direction of the flat plate. Two different types of

surface roughness were applied to the plate. One was course (No. 8) sand paper that was designed to trip the boundary layer to a turbulent state. The other was uniformly spaced 0.25 inch high wooden slats that both tripped the flow and produced rapid thickening of the boundary layer.

The trailing-edge radii were removable on the flat plate. Three radii were examined: 2.5 in (6.35 cm), 4.1 in (10.4 cm) and 5.0 in (12.7 cm). These were examined for three free-stream velocities of 6.6, 16.6 and 33 ft/s (2, 5 and 10m/s). The relatively low free-stream speeds were dictated by the ability to perform flow visualization, which gave a quick assessment of the degree to which the flow was turned by the plasma actuator, as well as the large blockage produced by the plate assembly in the test section.

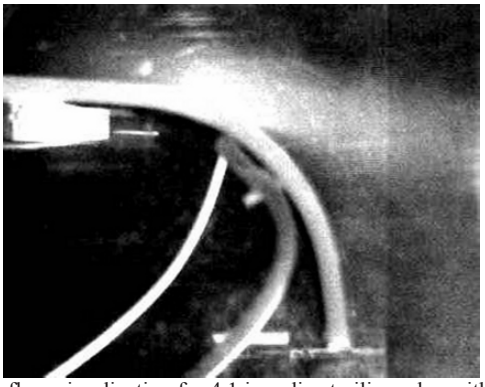

Fig. 6 Sample particle flow visualization for 4.1 in radius trailing edge without plasma flow control. Flow direction is from left to right.

The trailing edges were made by forming 0.25 inch thick Teflon sheets around circular mandrels. Teflon was chosen because it has excellent electrical properties to act as the dielectric layer between the electrodes in the SDBD plasma actuator. By using the whole radius material as the dielectric, the electrodes for the actuator could be located anywhere on the radius. The electrodes were made of 0.001 in (0.0254mm) thick copper foil tape. Generally, the downstream edge of the exposed electrode (flow side of the radius) was located just upstream of the separation location. The covered electrode dimension in the flow direction was 1 in (2.54 cm). The spanwise dimension of the electrodes corresponded to two-thirds of the width of the plate, and was centered in the spanwise direction.

The flow was made visible by introducing particles from a PIV particle generator part of the way up the second contraction ahead of the leading edge of the flat plate. The flow at the leading edge was carefully examined to insure that the particle injection did not cause the flow to separate on the second contraction or at the plate leading edge. An example of the particle flow visualization is shown in Fig. 6 for a 4.1 inch (10.4 cm) radius trailing edge. Here the flow is from left to right. It was illuminated by a sheet of light that was projected from the top at the spanwise centerline. This is a case without a plasma actuator. The flow is observed to naturally turn part way over the radius. Although there was a systematic

pattern to the degree with which the flow would turn as a function of the various parameters, the interpretation was felt to be too subjective. Therefore a surface flow visualization approach was also used.

A technique that visualized the flow on the surface of the trailing-edge radius was used to quantitatively determine the angle at which the flow separated. This technique involved applying a thin layer of an oil and china-white particle mixture that evaporated over time. The mixture was applied with the wind tunnel off. The tunnel was then quickly brought up to the set velocity. The liquid mixture was transported over the surface in response to the local surface shear stress vectors. After some time the liquid evaporated leaving the white particles in their final locations. The separation line was clearly visible from this technique. It was recorded by measuring around the circumference from the junction of the trailing-edge radius and the flat plate to the line of flow separation.

The approaching boundary layer was documented using a pitot-static probe attached to a motorized traversing mechanism. Examples of the mean profiles are shown in Fig. 7. These profiles were taken at the junction between the flat plate and the trailing-edge radius. The profiles are for the sand paper tripped boundary layer labeled "smooth", and the wall that was covered with the 0.25 inch wood slats, labeled "rough", at the highest free-stream speed of 33 ft/s (10 m/s). The boundary layer thickness for the "smooth" case is approximately 1.6 inches (4 cm). The "rough" wall increases the boundary layer thickness by approximately 60 percent at the downstream location. This is sufficient to investigate any influence of the boundary layer thickness on the ability of the plasma actuator to turn the flow around a radius.

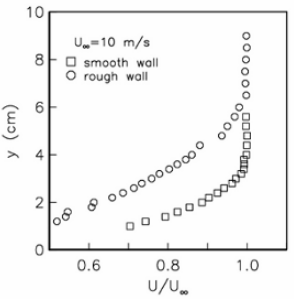

Fig. 7 Mean velocity profiles take at the junction between the flat plate and the trailing- edge radius for the two roughness conditions (sand-paper trip labeled "smooth") and the 0.25 inch wood slats (labeled "rough").

The effect of the plasma actuator voltage on the flow turning angle was investigated for the different parameters including the three radii and three velocities. An example of particle flow visualization images is shown in Fig. 8. This corresponds to the 4.1 in (10.4 cm) radius at the free-stream speed of 33 ft/sec (10m/s). The baseline (0 volts) indicates that there is a small amount of turning of the flow that occurs naturally. The plasma actuator was then located just upstream of that location. With the plasma actuator operating, the images clearly show an increase

in the angle of turning of the flow over the trailing edge radius as the voltage input to the actuator increases.

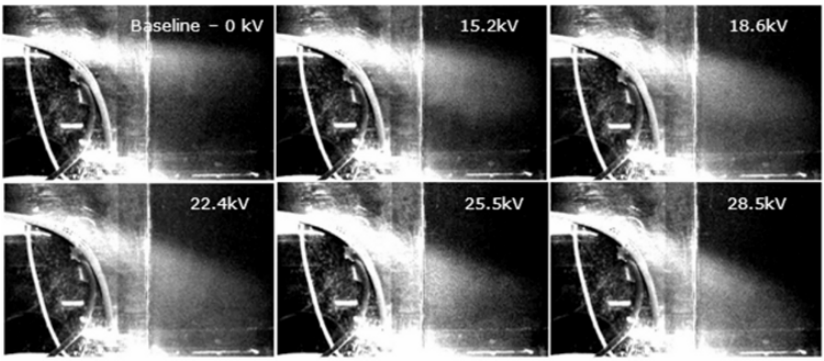

Fig. 8 Particle flow visualization showing the effect of plasma actuator voltage on the flow turning angle with 4.1 inch trailing edge radius

As previously mentioned, it was felt that the particle visualization was not sufficient to quantitatively indicate the turning angle of the flow. This was especially true at the higher velocity where there was considerable mixing of the separated shear layer. Therefore the surface flow visualization was used.

The surface visualization left a clear impression of the separation line on the trailing edge radius. Based on this, we defined a separation length, xs, as the distance along the circumference from the junction of the flat plate and the start of the radius to the separation location. Figure 9 illustrates this separation length.

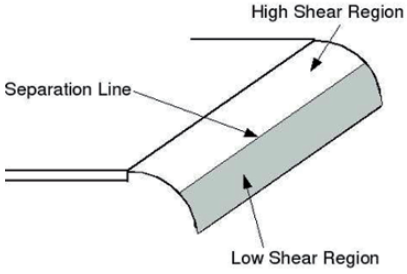

Fig. 9 Schematic showing the method of measuring the separation length, xs

The separation distances, xs, for the three radii as a function of the plasma actuator input voltage at the three free-stream speeds are shown in Fig. 10. The different freestream speeds are indicated by the different symbols. For any given radius, the change in xs is more a function of the plasma actuator voltage than the free-stream speed. Therefore we chose to fit a curve through the average of the values of the three free-stream speeds. For all three radii, the best fit curve relating the separation length to the actuator voltage was a straight line. Extrapolating the straight lines to the 0 kV actuator voltage gives the natural separation lengths for the three radii.

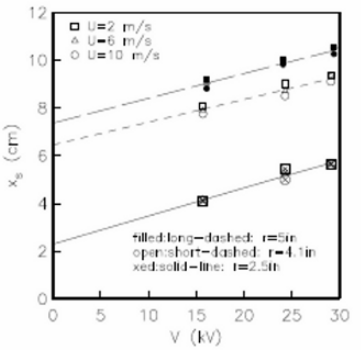

Fig. 10 Separation length, xs, for three radii as a function of the actuator voltage for three free-stream speeds

The separation lengths can be converted into turning angles of the flow by incorporating the trailing-edge radius, namely, $\theta = xs/r$. The flow turning angles, θ, that were converted from the xs values plotted in Fig. 10 are shown in Fig. 11. Again the effect of the different free-stream speeds is minimal, and the same straight-line fits that were used in Fig. 10 are again applied here. Extrapolating the straight lines to the 0 kV actuator voltage in this case gives the natural turning angle for the three radii.

We can observe a number of characteristics about the flow turning angle:

1. The natural flow turning angle decreases with increasing velocity
2. The response of the flow turning to the actuator input voltage increases with decreasing radius

In order to better illustrate these observations, we wished to subtract off the natural (actuator off) turning angles for the three radii. Figure 12 shows a comparison of the directly measured natural flow turning angles and the values obtained by extrapolating the straight- line fits to 0 kV in Fig. 11. These are observed to agree well, which substantiates the fit used in the previous figures.

We refer to the angle that the flow turns naturally for a given radius, as θ_0. These values have been subtracted from the turning angles produced by the plasma actuator previously shown in Fig. 11 to obtain the results plotted in Fig. 13. This figure indicates the flow turning increment. That is, it represents the added flow turning, above the natural amount that occurs without flow control that is actually produced by the plasma actuator. This representation clearly shows that the plasma actuator was more effective (larger slope) as the radius decreased.

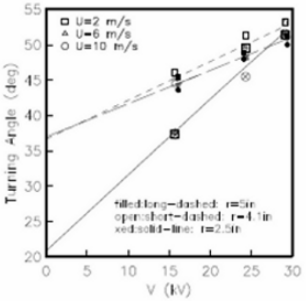

Fig. 11 Flow turning angle, θ, for three radii as a function of the actuator voltage for three free-stream speeds.

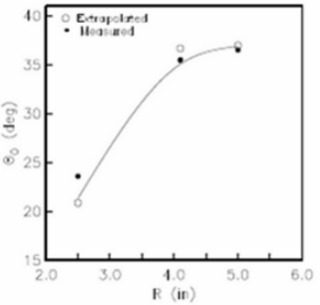

Fig. 12 Natural flow turning angle, θ, for three radii directly measured, and found by extrapolating values in Fig. 11 to a 0 kV actuator input.

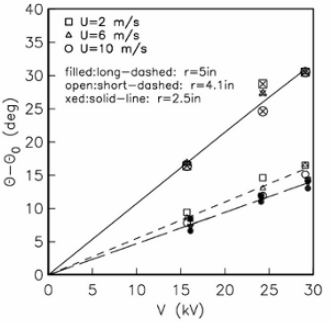

Fig. 13 Flow turning angle increment, $\theta-\theta_0$, for three radii as a function of the actuator voltage for three free-stream speeds.

The effect of the boundary layer thickness on the flow turning angle produced by the plasma actuator was found to be minimal. This is documented in Fig. 14 for the intermediate radius case.

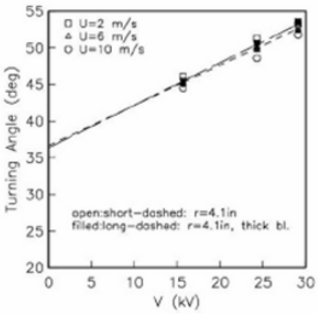

Fig. 14 Effect of the boundary layer thickness on the flow turning angle, θ, for an intermediate radius as a function of the actuator voltage for three free-stream speeds

Flat-plate Cylinder

One of the original objectives was to determine the effect that turning the flow around the trailing-edge radius had on the momentum recovery of the flow in the wake. The original setup was not sufficient to estimate this. Therefore a different setup was used that consisted of a suspended flat plate with a 2.5 in (6.35 cm) radius cylinder at the trailing edge. A schematic of the setup is shown in Fig. 15. Sand paper roughness like that used in the previous setup was used to trip the boundary layer to turbulence. Because the approach boundary layer to the cylinder was turbulent, it could be thought of as representing a super-critical Reynolds number condition for a circular cylinder. Under such as condition, the separation locations move from the top and bottoms of the cylinders, to positions approximately 23° further downstream. The lower blockage of this setup also allowed the measurements to be performed at higher free-stream speeds.

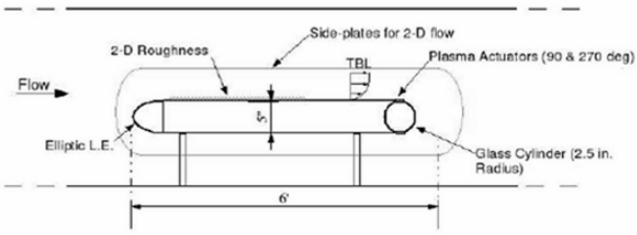

Fig. 15 Schematic of plate-cylinder setup used to measure mean velocity profiles resulting

Mean velocity profiles were measured in the wake of the plate-cylinder at a downstream location corresponding to 3 cylinder diameters. This was done at four free-stream speeds corresponding to 15, 20, 25, and 30 m/s. For these, the Reynolds number based on the cylinder diameter ranged from $128K \leq Re_D \leq 256K$, and the Reynolds number based on the x-length of the plate ranged from $1.5M \leq$

Rex ≤ 3.1M. Figure 16 shows mean velocity profiles for the four speeds for three conditions: (1) with the plasma actuator off, (2) with plasma actuators on at the 90° and 270° positions, and (3) with plasma actuators on at the 112° and 248° positions. In general the plasma actuator reduces the wake deficit compared to the base condition. In addition, the actuator is more effective when it is placed closer to the separation location (112° and 248°) than at the sub-critical cylinder separation locations from plasma flow control designed to turn the flow around the trailing edge radius.(90° and 270°). Finally for the fixed power applied to all of the free-stream conditions, the improvement of the wake deficit was less at the higher speeds.

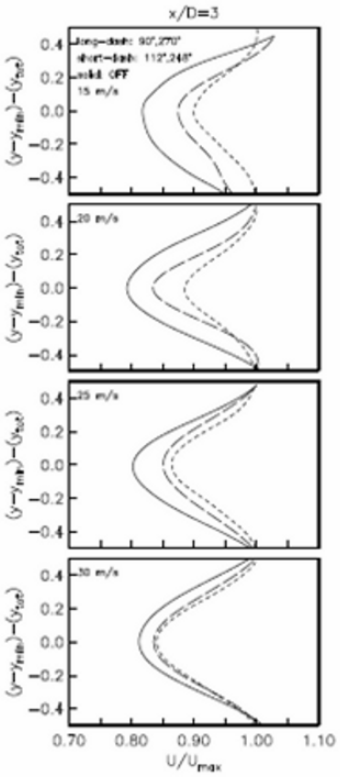

Fig. 16 Mean velocity profiles measured 3 trailing-edge cylinder diameters downstream of the plate-cylinder with the plasma actuator off (solid curve), and with it on in two arrangements (dashed curves). (128K ≤ ReD ≤ 256K, 1.5M ≤ Rex . ≤ 3.1M)

The results are further quantified by integrating the mean velocity profiles to obtain the momentum in the wake. This is shown in Fig. 17. In this figure, the momentum in the wake with the plasma actuator on (Momact) is normalized by the momentum with the actuator off (Mom0) as Momact/Mom0. The smaller the ratio, the larger the amount of recovered momentum and, presumably, the lower the drag.

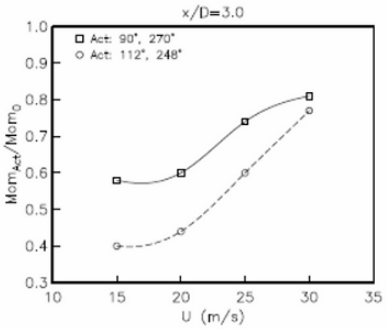

Fig. 17 Normalized momentum based on the mean velocity profiles in Fig. 16 for the two plasma actuator arrangements. ($128K \leq Re_D \leq 256K$, $1.5M \leq Rex \leq 3.1M$)

As expected based on the mean velocity profiles, the plasma actuators located closer to the separation location performed better and thereby recovered a larger amount of the momentum in the wake of the cylinder. Also as indicated by the mean velocity profiles, the effect is reduced at the higher velocity. However at 30m/s, which corresponds to 67mph, (a respectable truck interstate speed), 25 percent of the momentum in the wake is recovered. Further measurements are needed to determine the drag improvement and the relative improvement after accounting for the power supplied to the plasma actuators. However, at this stage, the results are encouraging.

Summary

The SDBD plasma actuators were effective in controlling flow separation around a trailing- edge radius in which the approaching flow is a turbulent boundary layer. The baseline separation location moves upstream with decreasing radius. A linear dependence of the separation location, and thereby the flow turning angle, on the plasma actuator voltage was found. For this, there was a minimum sensitivity to the free-stream velocity and approaching turbulent boundary layer thickness.

The response of the flow to turn a prescribed radius as a result of the plasma actuator was found to increase with decreasing radius. Using a plate-cylinder setup, up to a 50 percent recovery of wake momentum was measured. At the highest free-stream speed of 30 m/s (67mph) there still remained a 25 percent recovery in momentum.

While much more work is needed to determine the total impact of this technology to reduce the drag and fuel consumption of trucks and other ground vehicles, the research thus far is very promising. Additional tests are planned for later in 2008 based on the results obtained in this effort. Additional baseline tests are planned along with different placement of actuators and the use of several actua-

tors operating in tandem to build on the technology such that further, more representative testing can be done over the road on actual rigs.

References

1. Thomas FO, Kozlov A and Corke TC 2005, Plasma actuators for landing gear noise control, AIAA Paper 2005-3010, 11th AIAA/CEAS Aeroacoustics Conference, To appear AIAA J., 2008.
2. Corke T, Jumper E, Post M, Orlov D, and McLaughlin T 2002, Application of weakly-ionized plasmas as wing flow-control devices. AIAA Paper 2002-0350.
3. Huang J, Corke T and Thomas F 2003, Plasma actuators for separation control of low pressure turbine blades. AIAA Paper 2003-1027. also AIAA J., Jan. 2006.
4. Post M and Corke T 2003, Separation control on high angle of attack airfoil using plasma actuators. AIAA Paper 2003-1024, also AIAA J., 42, 11, p. 2177.
5. Post M 2004, Plasma actuators for separation control on stationary and oscillating wings. Ph.D Dissertation, University of Notre Dame.
6. Post M and Corke T 2004, Separation control using plasma actuators – stationary and oscillating airfoils. AIAA Paper 2004-0841.
7. Corke T, He C and Patel M 2004, Plasma flaps and slats: an application of weakly- ionized plasma actuators. AIAA Paper 2004-2127.
8. Corke T and Post M 2005, Overview of plasma flow control: concepts, optimization, and applications. AIAA Paper 2005-0563.
9. Huang J 2005, Documentation and control of flow separation on a linear cascade of Pak-B blades using plasma actuators. Ph.D., University of Notre Dame, Notre Dame, Indiana.
10. Huang J, Corke T and Thomas F 2005, Unsteady Plasma actuators for separation control of low pressure turbine blades. To appear AIAA J..
11. Corke T, Post M and Orlov D 2007, SDBD Plasma Enhanced Aerodynamics: Concepts, Optimization and Applications. J. Progress in Aerospace Sci., Vol 43, No. 7-8, Oct-Nov.
12. Enloe L, McLaughlin T, VanDyken, Kachner, Jumper E, and Corke T 2004, Mechanisms and Response of a single dielectric barrier plasma actuator: Plasma morphology. AIAA J., 42, 3, p. 589. Also AIAA 2003-1021.
13. Enloe L, McLaughlin T, VanDyken, Kachner, Jumper E, Corke T, Post M, Haddad O 2004, Mechanisms and Response of a single dielectric barrier plasma actuator: Geometric effects. AIAA J., 42, 3, p 585.
14. Bradley R et al, Technology Roadmap for the 21st Century Truck Program. http://www.doe.gov/bridge, December, 2000.
15. DOE Annual Report, Annual Energy Review 2004. DOE/EIA-0384(2004), www.eia.doe.gov/aer, August, 2005

Adaptive Control of Post-Stall Separated Flow Application to Heavy Vehicles

L. Cattafesta[1], Y. Tian[1] and R. Mittal[2]

[1] Interdisciplinary Microsystems Group, Department of Mechanical and Aerospace Engineering, Gainesville, FL 32611-6250, USA
cattafes@ufl.edu
[2] Department of Mechanical and Aerospace Engineering
The George Washington University
Washington D.C. 20052

Abstract This paper discusses two adaptive feedback control approaches designed to reattach a massively separated flow over a NACA airfoil with minimal control effort using piezoelectric synthetic jet actuators and various sensors for feedback. One approach uses an adaptive feedback disturbance rejection algorithm in conjunction with a system identification algorithm to develop a reduced-order dynamical systems model between the actuator voltage and unsteady surface pressure signals. The objective of this feedback control scheme is to suppress the pressure fluctuations on the upper surface of the airfoil model, which results in reduced flow separation, increased lift, and reduced drag. A second approach leverages various flow instabilities in a nonlinear fashion to maximize the lift-to-drag ratio using a constrained optimization scheme – in this case using a static lift/drag balance for feedback. The potential application of these adaptive flow control techniques to heavy vehicles is discussed.

Introduction

Flow separation incurs a large amount of energy loss and limits the performance of many flow-related devices (e.g., airfoils, automobiles, trucks etc.). Researchers have been trying to mitigate or eliminate flow separation for over a century because of its large potential payoff in practical applications. Numerous passive and active separation control strategies have been attempted with varying degrees of success. Passive techniques involve geometric modifications to alter the flow characteristics, while active methods involve the use of flow actuators to modify the flow and therefore require external energy addition.

Passive techniques are desirable because of their simplicity and, if properly designed, their effectiveness at design conditions. However, the performance of a passive control system usually degrades at off-design conditions. In the context of

heavy vehicles, "off-design" encompasses speed deviations and poor weather (e.g., wind, snow, or rain).

The main benefit of active techniques is their ability to "adapt" to off-design conditions. However, most of the active control approaches are open-loop in nature and, hence, are not really adaptive. Feedback control uses sensors to feed back information about the flow and/or vehicle states, and a controller automatically adjusts the actuator input to achieve a desired control objective. If the controller is adjusted or redesigned automatically during this process, it is called "adaptive." The primary disadvantage of this approach is its complexity, and its use thus represents a paradigm shift from conventional passive and active control. Nonetheless, the potential performance benefits and improved robustness warrants research.

This paper addresses a model problem that is representative of the separated flow behind a heavy vehicle. In particular, two adaptive feedback control approaches are discussed that seek to reattach a massively separated flow over a NACA 0025 airfoil with minimal control effort using piezoelectric zero-net mass-flux actuators and various sensors for feedback. One approach uses an adaptive feedback disturbance rejection algorithm in conjunction with a system identification algorithm to develop a reduced-order dynamical systems model between the actuator voltage and unsteady surface pressure signals. Its objective is to suppress the pressure fluctuations on the upper surface of the airfoil model, which results in reduced flow separation, increased lift, and reduced drag. A second approach leverages various convective and global flow instabilities in a nonlinear fashion to maximize the lift-to-drag ratio using a constrained optimization scheme – in this case using a static lift/drag balance for feedback. Experiments are described to elucidate the baseline uncontrolled and controlled flow physics, and the potential application of these approaches to heavy vehicles is discussed.

Experimental Configuration

As shown in Fig. 1, separation control experiments are conducted on a two-dimensional, $c = 15.24$ cm chord NACA 0025 airfoil mounted in an open-return, low-speed wind tunnel with a 30.48 cm by 30.48 cm by 60.96 cm test section. Six unsteady pressure transducers (Kulite LQ125-5A) are mounted beneath 2.2 mm diameter pinhole apertures at the mid-span location located at approximately 44.0%, 52.5%, 61.0%, 69.5%, 77.9% and 86.4% chord. A strain-gauge balance integrated into the model mount is used to measure the total lift and drag forces of the airfoil for varying angles of attack.

The airfoil contains four piezoelectric zero-net mass-flux (ZNMF) actuators with $h = 0.5$ mm wide slots located in the central 1/3rd spanwise region of the airfoil. Here we describe control experiments that only use actuator #1 located at the 3% chord location; the other unused actuators slots are covered. Details on the

synthetic jet actuators used in this research can be found in Gallas et al. (2003), Holman et al. (2003), and Gallas (2005).

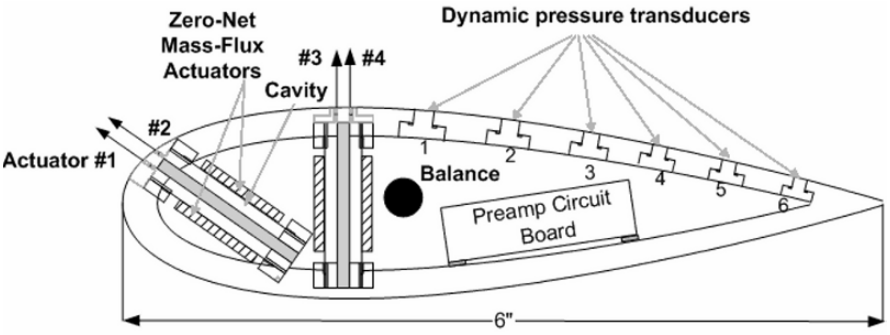

Fig. 1 Experimental setup of NACA 0025 airfoil showing four ZNMF actuators, a strain gage balance, and six dynamic surface pressure transducers.

The control system for the separation control experiments is implemented using a dSPACE (Model DS1005) DSP system with a 466 MHz PowerPC CPU. The dSPACE system has a 5-channel 16-bit A/D board (DS2001) and a 6-channel 16-bit D/A board (DS2102). The control algorithms are first programmed in Matlab/Simulink and C programs (C code S-functions) and then compiled and loaded on the dSPACE DSP processor.

The angle of attack (AoA) was greater than 10° for these experiments, corresponding to massive leading-edge separation or post-stall separated flow, as shown in Fig. 2. The chord Reynolds number, $\mathrm{Re}_c = \rho U_\infty c/\mu$, was 1E5 to 1.2E5. The BL is tripped in the leading edge region using 100 sand grit.

Problem Definition and Background

The objective of the control is to reattach the flow to the airfoil surface with minimal actuator power expenditure. A ZNMF actuator is a popular device for active flow control that requires no external flow source and works by alternately expelling and ingesting fluid through the actuator slot via a vibrating diaphragm (Glezer and Amitay 2002). Input sinusoidal oscillations are characterized by a dimensionless frequency $F^+ = fc/U_\infty$ and oscillatory momentum coefficient, $< C_\mu >= \left(\rho u_{j,rms}^2 h\right) \Big/ \left(0.5\rho U_\infty^2 c\right)$, where $u_{j,rms}$ is the rms jet velocity in the slot.

Although numerous studies are reported in the literature to determine the optimal forcing frequencies for effective separation control, the observed values of optimal F^+ vary over a wide range. For example, Greenblatt and Wygnanski (2000) concluded that the optimal range is $2 < F^+ < 4$. Seifert and Pack (1999) found

that the excitation frequency should be chosen such that $0.5 < F^+ < 1.5$ over a wide range of high Reynolds numbers. Conversely, Amitay et al. (2001) found that when the excitation frequency $F^+ > 10$, the lift-to-pressure-drag ratio was larger than when the excitation frequency $F^+ < 4$ for their unconventional airfoil.

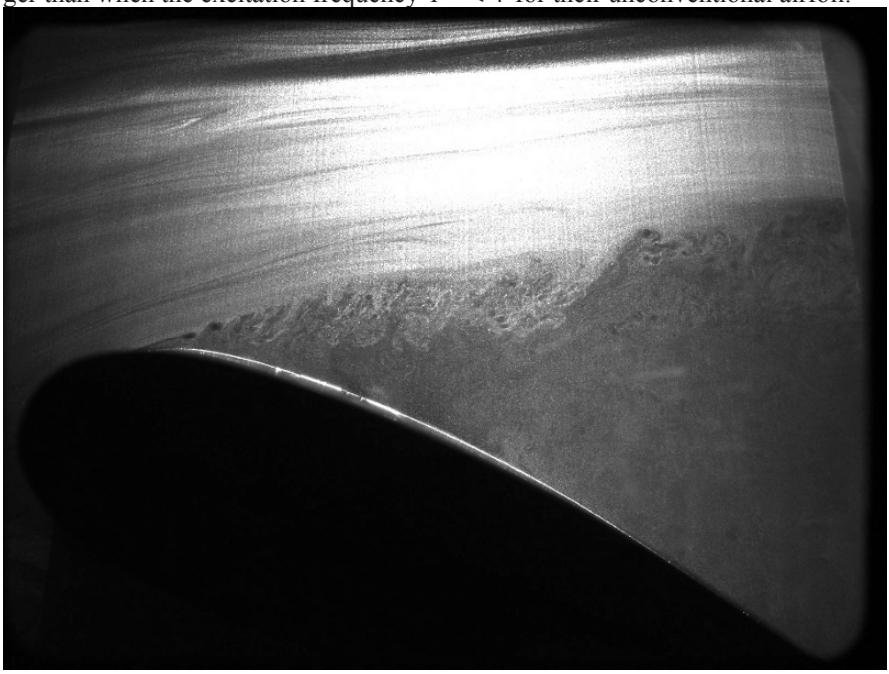

Fig. 2 Instantaneous laser light sheet visualization of the baseline uncontrolled post-stall separated flow on the airfoil at Re_c = 1E5 and angle-of-attack (AoA) = 20°.

For the case shown in Fig. 2, the optimal open-loop sinusoidal forcing for the present experiment is $F^+ = 15$ with $< C_\mu >= 3.16 \times 10^{-4}$, resulting in partial reattachment with an increase in lift-to-drag ratio from 1.1 for the baseline uncontrolled case to 1.76 (Tian 2007). Thus, it may appear that the present results are more in line with the findings of Amitay et al. However, this result is misleading since the optimal value of F^+ depends not only on the flow dynamics but also on the actuator. Figure 3 shows the normalized frequency response (i.e., the ratio of output rms jet velocity to input sinusoidal voltage) of actuator 1. Note that the actuator output is negligible below 500 Hz and peaks around 1100 Hz. So the optimal result of $F^+ = 15$, which corresponds to ~1000 Hz excitation, is at least partially explained by the fact that the actuator "works best" near this frequency. Nonetheless, the goal of the closed-loop control schemes is to at least match the performance of this optimal open-loop result, preferably with reduced actuator output, by relaxing the restriction to sinusoidal excitation.

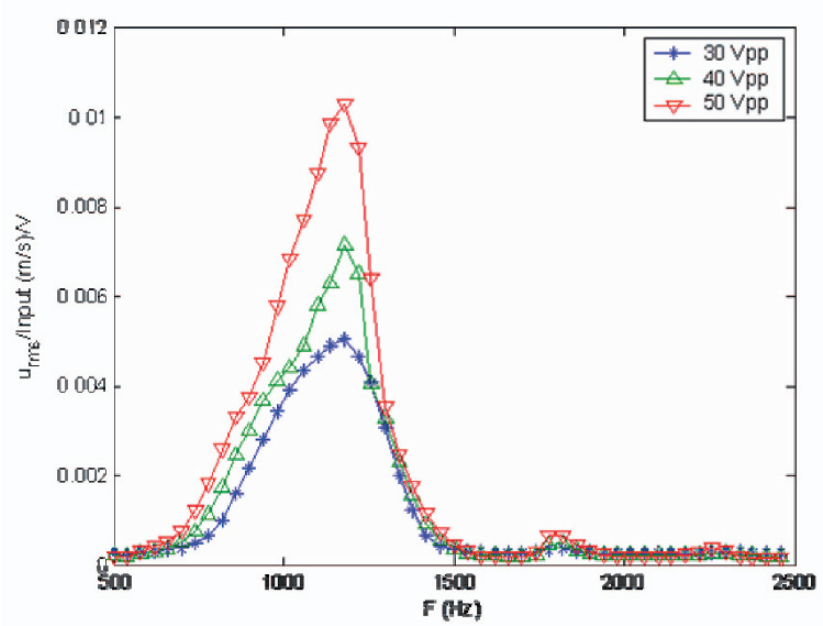

Fig. 3 Frequency response of ZNMF actuator 1. Note the actuator produces non-negligible output to sinusoidal inputs only in the range from 500-1500 Hz.

Results and Discussion

In this section we summarize the results for two algorithms used for real-time adaptive flow control. The first is a conventional adaptive disturbance rejection algorithm that includes an adaptive linear system identification model. The second approach uses a nonlinear constrained optimization strategy to adjust the parameters of a multi-frequency waveform to maximize the lift-to-drag ratio.

ARMARKOV Disturbance Rejection

As mentioned above, this algorithm contains two parts: system identification (ID) and control. The ID portion produces a low-order dynamical system model between the actuator voltage and the unsteady pressure signals, while the control algorithm seeks to suppress the power or mean-square value of the unsteady pressure fluctuations from one of the transducers. This approach is based on an inherent assumption that the unsteady pressure fluctuations are larger when the flow is

separated due to the passage of vortical structures over the surface of the model, the validity of which is demonstrated in Kumar and Alvi (2005).

A block diagram of the simultaneous ID and control algorithm is shown in Fig. 4. Here, both ID and control signals are input into the flow system, comprised of the actuator and airfoil, and the outputs of the system are assumed to be unsteady surface pressure measured by the transducers. The ID algorithm uses a band-limited input signal to the actuator with the performance pressure signal to develop an ARMARKOV system ID model (Akers and Bernstein 1997). The adaptive disturbance rejection algorithm uses the parameters identified in the system model combined with the measured airfoil surface pressures to tune or adjust the controller (Venugopal and Bernstein 2000). The ID and disturbance rejection algorithms are described in detail in the above references and in Tian et al. (2006b) and Tian (2007) for this problem.

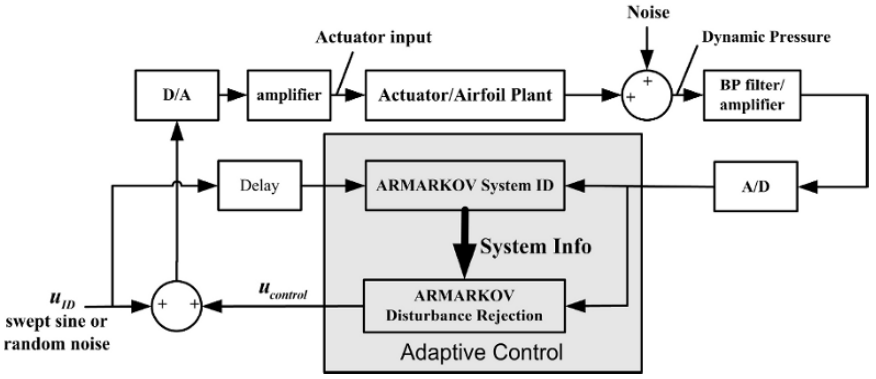

Fig. 4 Block diagram of adaptive system identification and disturbance rejection algorithm.

Constrained Nonlinear Optimization

Various optimization strategies are discussed in the literature (Press et al. 1992). After some experimentation with several extremum-seeking algorithms (Artiyur and Krstic 2003; Banaszuk et al. 2003), the downhill simplex method described in Press et al. was implemented to minimize the drag-to-lift ratio.

The benefits of the algorithm are its simplicity and applicability to multi-parameter constrained optimization and its faster convergence rate compared to extremum-seeking control for the present problem. The key steps of the algorithm are summarized as follows: 1) evaluate the cost function at chosen initial conditions, 2) use the lowest value as a reference and search for a lower value of the cost function, 3) move only in the downhill direction, and 4) terminate when some convergence criteria are met. The method thus finds a local minimum. To improve

the probability of finding the global minimum, multiple experiments are performed starting from different initial conditions. Again, the details of this algorithm are described in Tian et al. (2006a) and Tian (2007).

As explained in Tian (2007), the separated flow exhibits two dominant flow instabilities. The separated shear layer is characterized by convective Kelvin-Helmholtz (K-H) instabilities, which manifest themselves as the large-scale vortical structures with frequency $f_{SL} \sim U_\infty / \theta_0$, where θ_0 is the initial momentum thickness of the boundary layer just prior to separation (see Fig. 2). The large wake is characterized by a global instability, which manifests itself as a vortex street with frequency $f_{wake} \sim U_\infty / \theta_{wake}$, where θ_{wake} is the momentum thickness of the wake. The global wake instability interacts in a nonlinear fashion with the K-H instability. Since $\theta_{wake} >> \theta_0$, then $f_{wake} << f_{SL}$ so these two frequencies are widely separated in the post-stall case. This fact emphasizes the need for an actuator with sufficient bandwidth to excite both instabilities. The key assumption is that control will be more effective if both of these instabilities are excited, and this can only be achieved via a mult-frequency waveform.

Tian et al. (2006a) and Tian (2007) describe three such waveforms: amplitude modulation (AM), burst modulation (BM), and pulse modulation (PM). Each of these represents the product of a high-frequency carrier signal and a low-frequency modulation signal. For example, an AM signal is

$$e(t) = A \sin\left(2\pi f_c t\right) \frac{1 + \sin\left(2\pi f_m t\right)}{2},$$

which is characterized by three parameters: the amplitude A, carrier frequency f_c, and modulation frequency f_m. The use of such a complex waveform produces a rich spectrum of input disturbances due to flow nonlinearities, which in turn excites the K-H and wake instabilities. The goal of the simplex algorithm is to adjust these three parameters to minimize the drag-to-lift ratio.

Finally, to negate the preferential actuator output over a certain frequency range described above, the ZNMF actuator output jet rms velocity is "calibrated" using a constant-temperature hot-wire anemometer and current probes for each waveform type (AM, BM, or PM) to provide a look-up table that relates $< C_\mu >$ and actuator electrical power to the waveform parameters. In this manner, the optimization can be constrained to fix either $< C_\mu >$ or electrical power while A, f_c, and f_m are adjusted. This permits a fair comparison between different actuator waveforms.

Both adaptive controllers are able to completely reattach the separated flow at AoA=12°, as shown in Fig. 5, and L/D is increased to 7.0 ± 0.4. As the AoA is increased above 12°, the performance of the adaptive disturbance rejection controller, which is inherently linear, gradually deteriorates. Finally at AoA=20°, the

lift-to-drag ratio is essentially identical to that of the uncontrolled case ($L/D = 1.1 \pm 0.04$). In contrast, the nonlinear controller is more robust at higher angles of attack. In particular, at AoA=20°, $L/D = 2.18 \pm 0.07$ for AM with $< C_\mu >= 7.15 \times 10^{-6}$, $f_m = 61$ Hz and $f_c = 2405$ Hz. Optimal sinusoidal control was achieved with $< C_\mu >= 3.16 \times 10^{-4}$, resulting in $L/D = 1.76 \pm 0.03$. Note that slightly superior performance is achieved via nonlinear feedback vs. sinusoidal control but with a reduction in $< C_\mu >$ by a factor of 44! More details on these experiments are provided in Tian (2007).

Conclusions

The results of these experiments on a model post-stall airfoil problem show the potential of adaptive control of separated flow. In particular, the nonlinear controller appears most promising due to its ability to leverage multiple flow instabilities and therefore achieve control with very low energy expenditure.

The above closed-loop methodology appears to be applicable to heavy vehicles and would be a natural extension of previous open-loop control approaches (Hsu et al. 2004; Englar 2004). In particular, the massive wake behind a truck will likely exhibit similar flow instabilities as that of a post-stall airfoil, namely the K-H shear layer and global wake instabilities. Of course, the three-dimensional nature of the bluff body wake will be more complex. In addition, the objective function for control will differ from the lift-to-drag ratio. Since drag reduction is the main objective for a heavy vehicle, maximizing the average base pressure is perhaps a reasonable objective. Unsteady actuation around the rear perimeter of the vehicle appears to be a logical location for the actuators. In summary, it seems clear that further research on this topic is both warranted and required to understand the benefits and limitations of adaptive feedback flow control as applied to heavy vehicles.

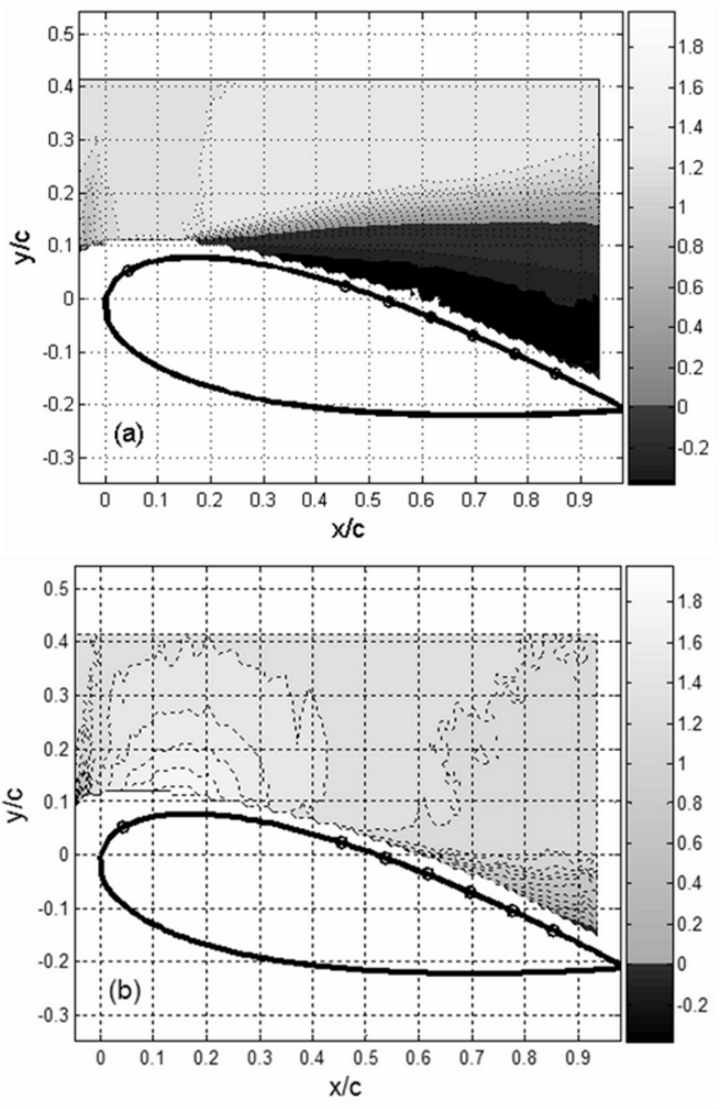

Fig. 5 Contours of streamwise velocity u/U_∞ for (a) baseline and (b) closed-loop control at AoA = 12° and Re_c =120,000.

References

Akers J and Bernstein D, "Time-Domain Identification Using ARMARKOV/Toeplitz Models", Proceedings of the American Control Conference, pp. 191-195, June 1997.

Amitay M, Smith D, Kibens V, Rarekh D and Glezer A, "Aerodynamic Flow Control over an Unconventional Airfoil Using Synthetic Jet Actuators," *AIAA Journal,* Vol. 39, No. 3, pp. 361-370, March 2001.

Artiyur K and Krstic M, Real-Time Optimization by Extremum-Seeking Control, Wiley-Interscience, 2003.

Banaszuk A, Narayanan S and Zhang Y, "Adaptive Control of Flow Separation in a Planar Diffuser," AIAA paper 2003-0617, January 2003.

Englar R, "Pneumatic Heavy Vehicle Aerodynamic Drag Reduction, Safety Enhancement and Performance Improvement," Proceedings of the UEF Conference on The Aerodynamics of Heavy Vehicles:Trucks, Buses and Trains, Lecture Notes in Applied and Computational Mechanics Springer-Verlag, Heidelberg, September, 2004.

Gallas Q, "On the Modeling and Design of Zero-Net Mass Flux Actuators," Ph.D. Thesis, Department of Mechanical and Aerospace Engineering, University of Florida, May 2005.

Gallas Q, Holman R, Nishida T, Carroll B, Sheplak M, and Cattafesta L, "Lumped Element Modeling of Piezoelectric-Driven Synthetic Jet Actuators," *AIAA Journal*, Vol. 41, No. 2, pp. 240-247, 2003.

Glezer A and Amitay M, "Synthetic Jets," *Annual Review of Fluid Mechanics*, Volume 34, pp. 503-529, January 2002.

Greenblatt D and Wygnanski I, "The control of flow separation by periodic excitation," *Progress in Aerospace Sciences*, Vol. 36, pp. 487-545, 2000.

Holman R, Quentin G, Carroll B and Cattafesta L, "Interaction of Adjacent Synthetic Jets in an Airfoil Separation Control Application", AIAA Paper 2003-3709, June 2003.

Hsu T-Y, Hammache M & Browand F, "Base Flaps and Oscillatory Perturbations to Decrease Base Drag," Proceedings of the UEF Conference on The Aerodynamics of Heavy Vehicles:Trucks, Buses and Trains, Lecture Notes in Applied and Computational Mechanics Springer-Verlag, Heidelberg, September, 2004.

Kumar V and Alvi F, "Efficient Control of Separation Using Microjets," AIAA Paper 2005-4879, June 2005.

Press W, Flannery B, Teukolsky S and Vetterling W, Numerical Recipes in Fortran, 2nd edition, Cambridge University Press, January 1992.

Seifert A, Pack L, "Oscillatory Control of Separation at High Reynolds Numbers," *AIAA Journal,* Vol. 37, No. 9, pp. 1062-1071, September 1999.

Tian Y, "Adaptive Control of Separated Flow," Ph.D. Thesis, Department of Mechanical and Aerospace Engineering, University of Florida, Gainesville, FL, August 2007.

Tian Y, Cattafesta L, and Mittal R "Adaptive Control of Separated Flow," AIAA Paper 2006-1401, January 2006a.

Tian Y, Song Q and Cattafesta L, "Adaptive Feedback Control of Flow Separation," AIAA Paper 2006-3016, June 2006b.

Venugopal R and Bernstein D , "Adaptive Disturbance Rejection Using ARMARKOV/Toeplitz Models," IEEE Transactions on Control Systems Technology, Vol. 8, No. 2, pp. 257-269, March 2000.

Investigation of Tractor Base Bleeding for Heavy Vehicle Aerodynamic Drag Reduction

Jason Ortega[1], Kambiz Salari[1], Bruce Storms[2]

[1] Lawrence Livermore National Laboratory, USA
[2] NASA Ames Research Center, USA
ortega17@llnl.gov

Abstract The drag reduction capability of tractor base bleeding is investigated using a combination of experiments and numerical simulations. Wind tunnel measurements are made on a 1:20 scale heavy vehicle model at a vehicle width-based Reynolds number of 420,000. The tractor bleeding flow, which is delivered through a porous material embedded within the tractor base, is introduced into the tractor-trailer gap at bleeding coefficients ranging from 0.0-0.018 for two different gap sizes with and without side extenders. At the largest bleeding coefficient with no side extenders, the wind-averaged drag coefficient is reduced by a maximum value of 0.015 or 0.024, depending upon the gap size. To determine the performance of tractor base bleeding under more realistic operating conditions, computational fluid dynamics simulations are performed on a full-scale heavy vehicle traveling within a crosswind for bleeding coefficients ranging from 0.0-0.13. At the largest bleeding coefficient, the drag coefficient of the vehicle is reduced by 0.146. Examination of the tractor-trailer gap flow physics reveals that tractor base bleeding reduces the drag by both decreasing the amount of free-stream flow entrained into the gap and by increasing the pressure of the tractor base relative to that of the trailer frontal surface.

1 Introduction

During the 1970s and 1980s, a number of first-generation drag reduction devices were designed to reduce the aerodynamic losses of heavy vehicles [5]. The result of this effort led to the development of a number of devices (front-end rounding, tractor aero-shields, body molding, and cabin side extenders) that improved the aerodynamics of heavy vehicle tractors. Additionally, a number of second-generation devices (tractor-trailer gap sealers, trailer side skirts, and boat-tails) were developed. Unfortunately, these devices did not enter into the market on a wide-scale basis, which was due not to their ineffectiveness in reducing drag,

but rather to operational, maintenance, and, ultimately, economic concerns. However, with rising fuel costs and potentially unstable fuel supplies, there is a renewed objective to further reduce heavy vehicle aerodynamic drag.

On a modern heavy vehicle, one of the main sources of aerodynamic drag is tractor-trailer gap drag, which occurs when the vehicle is operating in a crosswind and free-stream flow is entrained into the tractor-trailer gap. This flow entrainment imparts a momentum exchange to the heavy vehicle in the direction opposite of travel, resulting in a drag increase. Presently, cabin side extenders, which are 0.46-0.51 m wide vertical plates attached to the tractor base, are routinely utilized on modern heavy vehicles to mitigate flow entrainment into the gap. Wind tunnel measurements have shown that side extenders, when used in conjunction with a rooftop aero-shield and tractor side skirts, reduce the wind-averaged drag coefficient, C_{dwavg}, by about 0.15 [6]. Other devices, such as gap sealers and fillers are also effective in reducing tractor-trailer gap drag and provide additional reductions in the wind-averaged drag coefficient ranging from about 0.03-0.06 [6]. However, due to maintenance and operational issues, these devices are not commonly installed on modern heavy vehicles.

Despite their widespread use, side extenders are often damaged during routine shipping operations. Commercial fleets frequently comment that the large structural surfaces comprising the side extenders are easily bent or crushed when the tractor pivots too sharply relative to the trailer during loading maneuvers. When such damage occurs, the commercial fleets are forced to take the tractor out of operation for service and either remove or replace the side extenders, a task which can become extremely costly when such repairs are required for several thousand tractors in the larger shipping fleets. Consequently, there is a need to devise alternate drag reduction concepts that can both alleviate flow entrainment into the tractor-trailer gap and be less prone to damage during vehicle articulation. One such concept recently developed are side extenders that are about 38% shorter than those presently used and still provide nearly the same aerodynamic benefit [7].

Another proposed concept is tractor base bleed, in which a stream of low-speed flow is injected into the tractor-trailer gap at a velocity, U_b, over a large surface area, A_b, on the tractor base. Base bleed has been previously studied as a means of reducing the drag of bluff bodies, such as ballistic shells [18], blunt-base airfoils [28], backward facing steps [16], and circular cylinders [23]. The typical values of bleeding flow, defined by the bleeding coefficient, $C_\mu = U_b A_b / U_o A_o$, range from 0.0-0.28, where U_o is the free-stream velocity and A_o the characteristic area of the body. Bearman [3], Michel & Kost [20], and Wood [28, 29] showed that base bleed increases the pressure over the bleeding surface, thereby reducing the overall drag of the bluff body. When sufficient bleeding flow is injected into the separated wake, Bearman [3], Schumm, *et al.* [23], and Wood [28, 29] demonstrated that the strength of the shed vortex street can be reduced. In addition, base bleeding displaces the separated wake in the downstream direction [3, 24, 29, 30]. Further increases in bleeding can suppress vortex shedding entirely. Yao & Sandham [30] showed that bleeding over a large area at a low velocity is more effective in

reducing the drag than bleeding over a small area at a high velocity. Base bleed has also been shown to influence the stability characteristics of the separated wake [11]. Arcas & Redekopp [1], Hammond & Redekopp [10], Huerre & Monkewitz [11], and Sevilla & Martinez-Bazan [24] observed that, at a critical bleed rate, the wake transitions from being absolutely unstable to convectively unstable. And, Koch [14,15] showed that the transition from absolute to convectively unstable flow occurs slightly downstream of the region of reverse flow in the separated wake.

Although the previous studies elucidated the flow physics and drag reduction capability of base bleeding, the types of bluff bodies used were either two-dimensional or axisymmetric. In addition, the bluff bodies were isolated from the influence of other bodies and were oriented at zero degrees yaw with respect to the free-stream flow. It is therefore difficult to determine from these previously published results as to whether or not base bleeding is an effective means of reducing the drag of a tractor-trailer gap, which is surrounded by both a highly asymmetric, three-dimensional geometry and a moving ground plane and which is typically oriented at a finite yaw angle. Thus, the purpose of this study is to investigate base bleeding as means of reducing tractor-trailer gap drag. In particular, we wish to answer the following questions. Does tractor base bleeding reduce the drag of a heavy vehicle? How much bleeding flow is required to produce a modest drag reduction? How is the flow within the tractor-trailer gap altered as a result of base bleeding? How do the gap flow physics and the reductions, if any, in drag due to tractor base bleeding compare to those of traditional side extenders?

2 Wind Tunnel Measurements

As a first step in providing answers to these questions, we perform wind tunnel measurements on a 1:20 scale heavy vehicle model that employs tractor base bleeding. The model tractor, which is a detailed representation [27] of a Freightliner Columbia [8], is fabricated using a rapid prototyping technique (Fig. 1a) [25]. The engine grill and the air inlets on the bumper are sealed since Leuschen & Cooper [17] measured very little difference in the drag coefficient when the cooling airflow through these two regions was blocked. To prevent laminar flow separation, several lengths of 4×10^{-4} m diameter wire are laid over the leading edges of the tractor and 4.6×10^{-4} m diameter glass beads are bonded to the tractor nose, visor, aero-shield, window pillars, door columns, and engine grill. The tractor is attached to a 0.69 m long model freight van that includes cross members and a landing gear on the trailer underside. The trailer body is constructed from 0.006 m thick sheets of acrylic, while the trailer wheels are fabricated in the same manner as that of the tractor. The tractor-trailer gap is adjustable and, for this study, is set to 0.038 and 0.076 m. Force measurements are made by suspending the entire tractor-trailer model on a six-component force balance (Northrop MK XVA 0.75")

that is positioned near the upstream end of the trailer. The signals from the force balance are digitized and stored on a computer using BDAS 9.3 data acquisition software [4]. The resulting drag coefficients, $C_d = D / \frac{1}{2}\rho U_o^2 A_o$, are obtained to within $\pm 1.69 \times 10^{-3}$, which includes both the balance accuracy and the average measurement repeatability, where D is the drag force along the body axis, x_a, of the model, ρ the density of air, and $A_o = 2.47 \times 10^{-2}$ m^2 the characteristic area of the model.

Tractor base bleeding is provided by directing a compressed air supply into two 0.019 m NPT air supply lines that are connected to two smaller 0.006 m internal diameter tubes, which enter the model through the trailer underside (Fig. 1b). The bleeding flowrate is measured with a pneumatic in-line flowmeter (Omega FL7722A). Since the 0.006 m internal diameter tubes pass from the non-metric to the metric portions of the force balance, a service loop is incorporated into the tubing before it exits the upstream end of the trailer underside and is attached to two ports on the tractor underside. These ports direct the airflow into a plenum that comprises the entire model tractor cabin. On the base of the tractor cabin are threaded holes to which several different rapid-prototyped pieces can be affixed. For base bleeding configurations, perforated tractor bases with and without 0.02 m wide side extenders are employed. On these pieces, the bleeding surface area is about 19% of the characteristic area, A_o, of the model tractor. For cases in which there is no bleeding flow, aluminum duct tape is placed over the perforated holes or a separate non-perforated tractor base piece with or without side extenders is fixed to the tractor base. Within the plenum, 0.051 m thick packing foam is positioned against the perforated tractor base to provide a pressure drop for the bleeding flow as it exits the plenum, thereby ensuring a more uniform bleeding velocity profile. Four bleeding flowrates, corresponding to base bleeding coefficients of 0.0, 0.008, 0.013, and 0.018, are used in this wind tunnel study. Velocity measurements made in the gap using a multi-hole pressure probe (Cobra, Turbulent Flow Instrumentation) with no tunnel velocity demonstrate fairly uniform bleeding velocity (Fig. 2).

The drag coefficient measurements are made within the NASA Ames Fluid Mechanics Laboratory open-circuit wind tunnel, which has a contraction ratio of 9:1, a test section size of 0.813 m × 1.219 m, and a free-stream turbulence level of 0.15%. The wind tunnel is operated at a nominal dynamic pressure and tunnel speed of 1420 N/m^2 and 48.95 m/s, respectively. The resulting width-based

a)

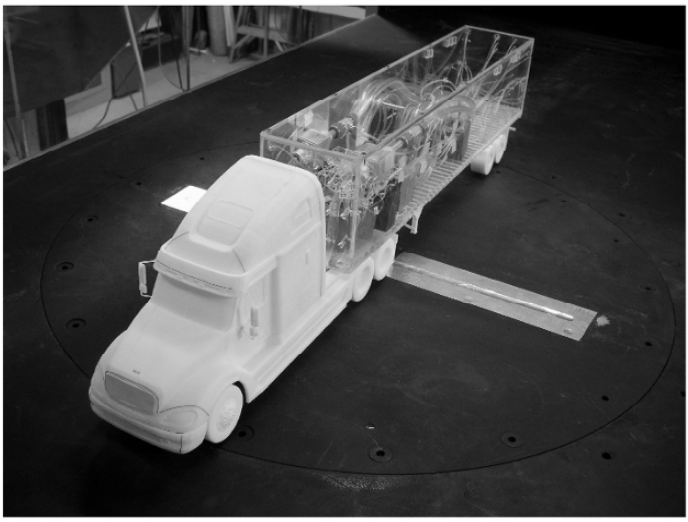

b)

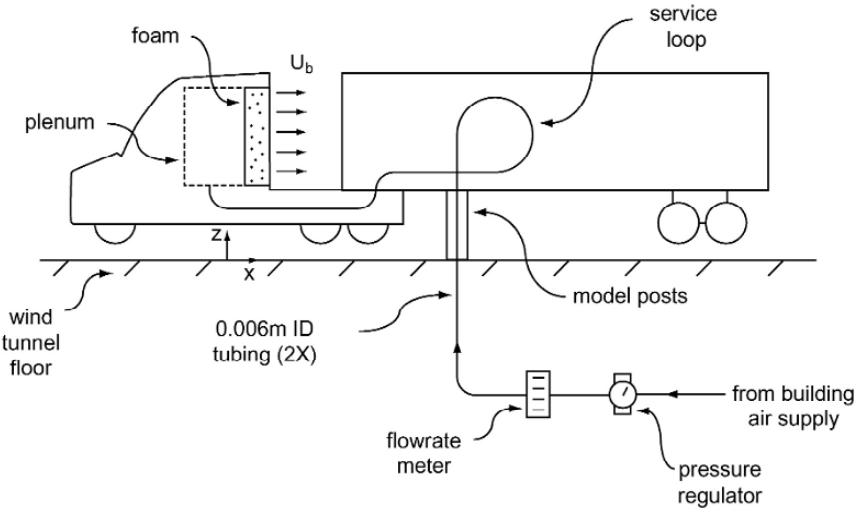

Fig. 1 a) 1:20 scale heavy vehicle model in the low-speed NASA Ames wind tunnel. b) Details of the tractor base bleeding system.

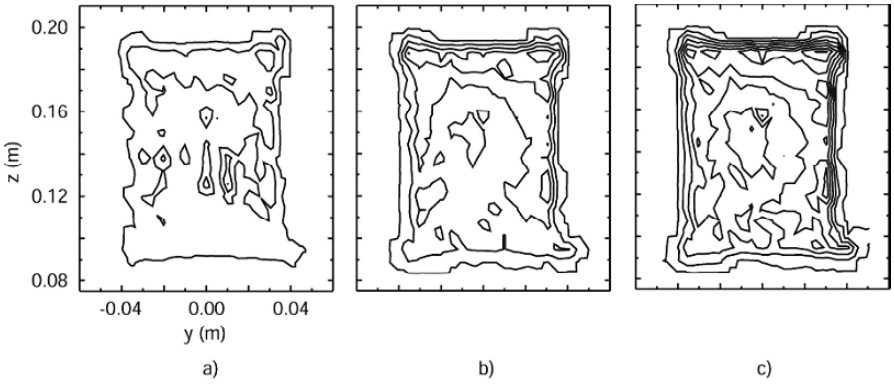

Fig. 2 Bleeding velocity contours in the x-direction made 0.019m downstream of the tractor base for C_μ equal to a) 0.008, b) 0.013, and c) 0.018 for a tractor-trailer gap distance of 0.076 m with no tunnel velocity.

Reynolds number, $Re_w = U_o w/\nu$, of the model is 420,000, where $w = 0.13$ m is the model width, and ν the kinematic viscosity of air. The percentage of blockage of the model in the tunnel test section is 2.5% at 0° yaw. The model is mounted at a height about equal to the boundary layer displacement thickness ($\approx 5.0 \times 10^{-3}$ m) above the tunnel floor on a turntable that is driven by a computer-controlled servo motor (Parker Compumotor), which can rotate the model to within ±0.05°. For each model configuration, force measurements are made at yaw angles ranging from ±8°. To assess the repeatability of the measurements, as well as hysteresis in the flow patterns over the model, the data are acquired on selective configurations for both increasing and decreasing yaw angle directions and are observed to show negligible hysteresis effects. Since the tractor bleeding flow generates forces on the model due to the effects of thrust and the expansion of the 0.006 m internal diameter tubing within the trailer, force measurements are first made at a zero tunnel velocity at each non-zero bleeding coefficient value. These forces are then subtracted from the subsequent measurements made at the corresponding bleeding coefficient values.

While the C_d data at each yaw angle is useful for evaluating the tractor base bleeding concept, it is somewhat cumbersome since the C_d distribution does not summarize the drag reduction performance into a single quantity that can be easily compared with that of other devices, such as side extenders. Taking the mean value of C_d over all measured yaw angles is also insufficient since it does not account for the fact that the crosswind velocities cause a vehicle traveling at a particular speed to experience certain yaw angles more than others. A quantity that resolves both of these issues is the wind-averaged drag coefficient, C_{dwavg} [12], which is computed for each base bleeding configuration (Fig. 3). It is apparent that the drag coefficient decreases as the bleeding coefficient is increased for both gap distances. However, a greater reduction in drag is observed for the larger gap distance both with and without side extenders. When $C_\mu > 0.006$, tractor base bleeding

with no side extenders at the larger gap distance yields a greater reduction in drag than that of side extenders alone with no bleeding flow. It should also be noted that the wind-averaged drag coefficients for the larger gap are greater than those of the smaller gap, indicating the presence of a larger amount of entrained flow into the tractor-trailer gap. Similar trends in the dependence of the drag coefficient upon gap distance, d_{gap}, were observed by Hammache & Browand [9], who investigated tractor-trailer gap flow dynamics on a simplified tractor-trailer geometry at a comparable Re_w of 270,000. At a critical gap distance of $d_{gap}/A_o \approx 0.5$, Hammache & Browand showed that the total vehicle drag increases sharply. In the present study, the values of $d_{gap} = 0.038$ and 0.076 m are below and about equal to the critical gap distance, respectively.

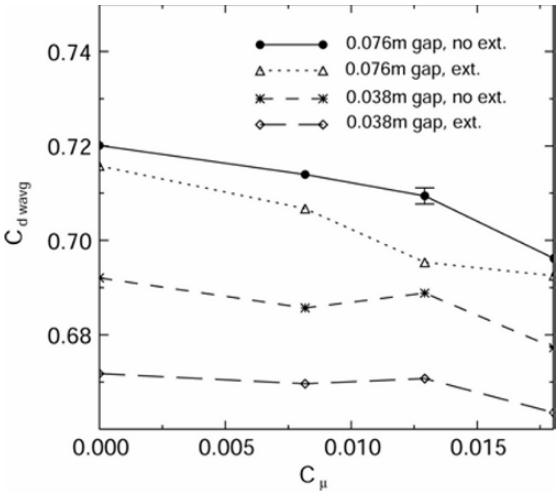

Fig. 3 Wind-averaged drag coefficient, C_{dwavg}, as a function of the tractor base bleeding coefficient, C_μ, for two tractor-trailer gap distances with and without side extenders

3 CFD Simulations

While the wind tunnel measurements demonstrate that tractor base bleeding can indeed reduce the drag of the heavy vehicle model, further investigation is needed both to demonstrate the effectiveness of this concept at a full-scale Reynolds number and to understand the changes in the gap flow physics arising from the base bleeding. For these reasons, we perform computational fluid dynamics (CFD) simulations on a full-scale Freightliner Columbia operating at highway conditions within a crosswind. The tractor-trailer gap distance is set to 1.02 m and a 13.6 m long freight van is attached to the tractor.

The simulations are performed within a computational domain that is 98m × 49m × 128m (Fig. 4), such that the heavy-vehicle cross-sectional area is 0.2% of that of the domain. To model the crosswind velocity, U_w , which is typically 3.1 m/s at vehicle mid-height [22], while the vehicle travels at a ground speed of U_g = U_o = 29.1 m/s, the vehicle is yawed to θ = $\tan^{-1}$ (U_w/U_g) = 6.1° and a velocity of $\sqrt{U_g{}^2 + U_w{}^2}$ = 29.3 m/s is specified at the inlet to the computational domain (Fig. 4). The resulting width-based Reynolds number is 5,000,000. Beneath the vehicle, a no-slip, moving ground plane boundary condition is prescribed at a velocity of U_g and a yaw angle of 6.1°. The no-slip surfaces of the tractor and trailer tires, which have a surface angular velocity boundary condition of 53 s^{-1}, intersect the ground plane, producing a tire contact patch that has a swept angle of 20° [2]. A slip boundary condition and a zero gradient boundary condition are specified along the walls and outlet, respectively, of the computational domain. To produce the tractor base bleeding flow, an inlet velocity boundary condition (U_b = 0.0-0.2U_o, v_c = 0, w_c = 0) is defined across the tractor base, which has an area that is 65% of that of the vehicle cross-section, A_o = 9.87 m^2. The corresponding bleeding coefficients range from 0.0-0.13. The other variables on the bleeding inlet boundary are computed by assuming a zero gradient normal to the inlet, such that the variables on the inlet nodes are extrapolated from the values of the interior nodes. To provide a performance comparison for the base bleeding concept, side extenders, which have a length of 0.38 m, are modeled in one vehicle configuration and compared with the baseline case. A finite-volume code [26] is used to solve the steady Reynolds averaged Navier-Stokes (RANS) equations for the flow about the heavy vehicle. The k−ω SST turbulence model [19] with a wall function is employed since a previous study by Pointer [21] demonstrated that this approach can adequately capture the value of C_d at a Re_w on the order of 10^6. The cell height adjacent to the vehicle is chosen to be 3.3 × 10^{-3} m, yielding a nominal value for y^+ [13] of 90 over the entire tractor-trailer surface. Meshes with about 25 × 10^6 cells are used in this study. The drag coefficient, which is typically averaged over 10,000-20,000 iterations, tends to oscillate by approximately ±0.007 about the average value, an effect possibly due to a lack of local mesh resolution.

A plot of the drag coefficient as function of the bleeding coefficient (Fig. 5) reveals that, in much the same manner as that of the wind tunnel measurements,

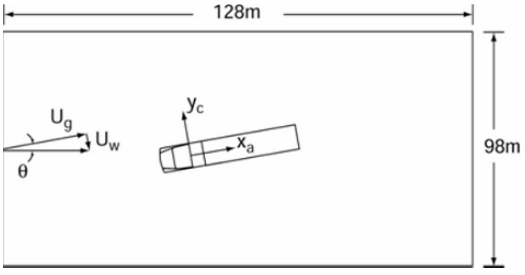

Fig. 4 Computational domain used for the full-scale CFD simulations

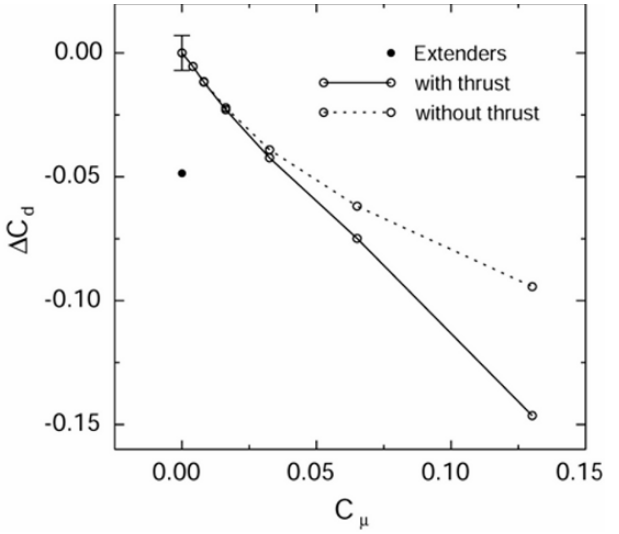

Fig. 5 Change in the drag coefficient as function of the bleeding coefficient for the CFD simulations

increases in bleeding flow decrease the drag coefficient. In addition, the drag reduction of $\Delta C_d \approx 0.025$ observed for $C_\mu \approx 0.018$ is about equal to that seen experimentally ($\Delta C_d \approx 0.02$) at 6° yaw for the larger gap distance despite the relatively large difference in Re_w. For the computational results, the drag coefficient decreases in a nearly linear fashion for the largest bleeding coefficients, values of which were not attainable in the wind tunnel measurements. The largest reduction in drag ($\Delta C_d = 0.146$) occurs at the maximum bleeding coefficient of 0.13. It is also evident that bleeding coefficients greater than 0.04 provide a larger reduction in drag than that of the side extenders ($\Delta C_d = 0.049$).

Obviously, a portion of the drag reduction produced by base bleeding is due to the thrust,

$$T = \int_{A_b} \rho U_b \mathbf{u} \cdot \mathbf{n} dA, \tag{1}$$

of the bleeding flow and not to modifications of the tractor-trailer gap flow physics, where **u** is the fluid velocity vector and **n** the unit normal vector of the vehicle surface. Removing this thrust contribution from the data in Fig. 5 demonstrates that, for the bleeding coefficients evaluated in this study, a significant drag reduction occurs solely due to changes in the gap flow physics.

One of the changes to occur is in the amount of free-stream fluid entrained into the tractor-trailer gap. The entrainment rate is computed by defining a rectangular control surface that encompasses the volume of the entire tractor-trailer gap (Fig. 6), but not the bleeding area over the tractor base. The entrainment flowrate,

$$Q_e = \int_{A_{in}} \mathbf{u} \cdot \mathbf{n}_{cs} dA, \tag{2}$$

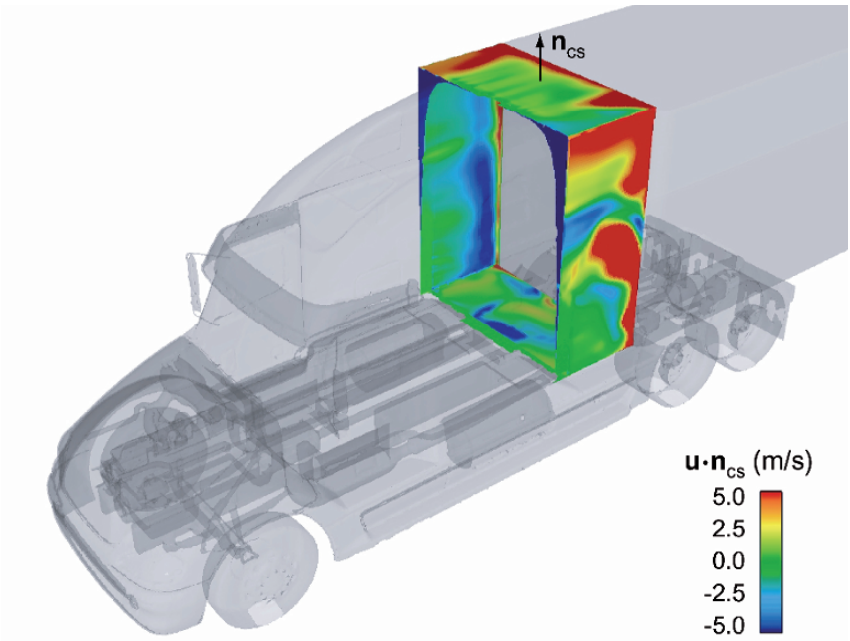

Fig. 6 Control surface defined for computing the flow entrainment rate, Q_e, into the tractor-trailer gap. The color contours on the surface denote the values of $\mathbf{u} \cdot \mathbf{n}_{cs}$ for $C_\mu = 0.0$.

is calculated over the control surface to determine the amount of fluid entering the gap from the free-stream, where $\mathbf{n}_{cs}$ is the normal vector of the control surface and the integration area, A_{in}, indicates that the integral is computed over those portions of the control surface in which $\mathbf{u} \cdot \mathbf{n}_{cs} < 0$. Without any base bleeding, the gap entrains free-stream fluid at a rate of $0.085 U_o A_o$, where a large portion of the entrainment occurs on the windward-downstream and bottom-upstream areas (Fig. 6) of the control surface. When side extenders are placed on the tractor base, $Q_e = 0.072 U_o A_o$. Due to the highly three-dimensional nature of the velocity field in the gap, the flow exits through distinct patches spread over the leeward and upper areas of the control surface. When $C_\mu > 0$, the bleeding flow reduces the amount of free-stream fluid entrained into the tractor-trailer gap (Fig. 7). (Note that the asymptotic decay of Q_e to what appears to be a value greater than zero is a result of the manner in which the control surface geometry is defined. The value of Q_e will likely be greater than zero for all C_μ because free-stream fluid will continue to enter the control surface through the upstream, vertical face.) A comparison of the contour plots of $\mathbf{u} \cdot \mathbf{n}_{cs}$ (Fig. 8) reveals that base bleeding significantly reduces the entrainment of free-stream fluid on the windward and bottom areas of the control

surface and produces an exit flow pattern that is more uniformly distributed over the downstream areas of the control surface.

The specific manner in which fluid entrainment is altered as a result of base bleeding can be understood by investigating the velocity field within the tractor-trailer gap. Prior to base bleeding, the windward shear layer separating from the tractor base impinges upon the trailer frontal face, producing a cross-stream flow in the form of a wall jet that spans the entire gap width (Fig. 9a,c). At the centerline of the gap, this wall jet has a maximum magnitude that is about $0.75U_o$ (Fig. 10). Since the flow re-circulates within the gap, a positive cross-stream velocity is present near the tractor base. As the amount of base bleeding is increased, the strength of the wall jet decreases. In addition, the cross-stream velocity profile becomes linear with the gap distance near the tractor base and the peak velocity of the positive-valued re-circulating flow diminishes. At a bleeding coefficient of C_μ = 0.13, the cross-stream velocity profile is linear throughout the entire tractor-trailer gap centerline, except within a thin boundary layer on the trailer frontal surface. Plots of the velocity field (Fig. 9b,d) show a relatively uniform gap flow, where the regions of large cross-stream flow are confined to the outer extents of the gap. It should also be noted that side extenders reduce the strength of the cross-stream flow, such that the maximum magnitude of the wall-jet is reduced to a value about equal to that which occurs when $C_\mu \approx 0.033$ (Fig. 10).

The shear layer that produces the wall jet within the gap leaves a distinct high pressure signature as it impinges upon the trailer frontal face (Fig. 11a). Away from this impingement zone, the pressure is considerably lower in magnitude, except for a region on the leeward side of the gap. When bleeding flow (C_μ = 0.13)

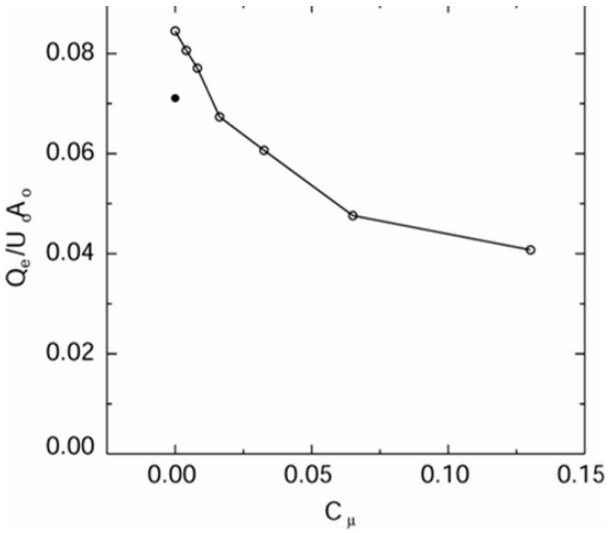

Fig. 7 Non-dimensional flow entrainment rate into the tractor-trailer gap as function of the bleeding coefficient. The symbol • denotes the configuration with side extenders (C_μ = 0.0).

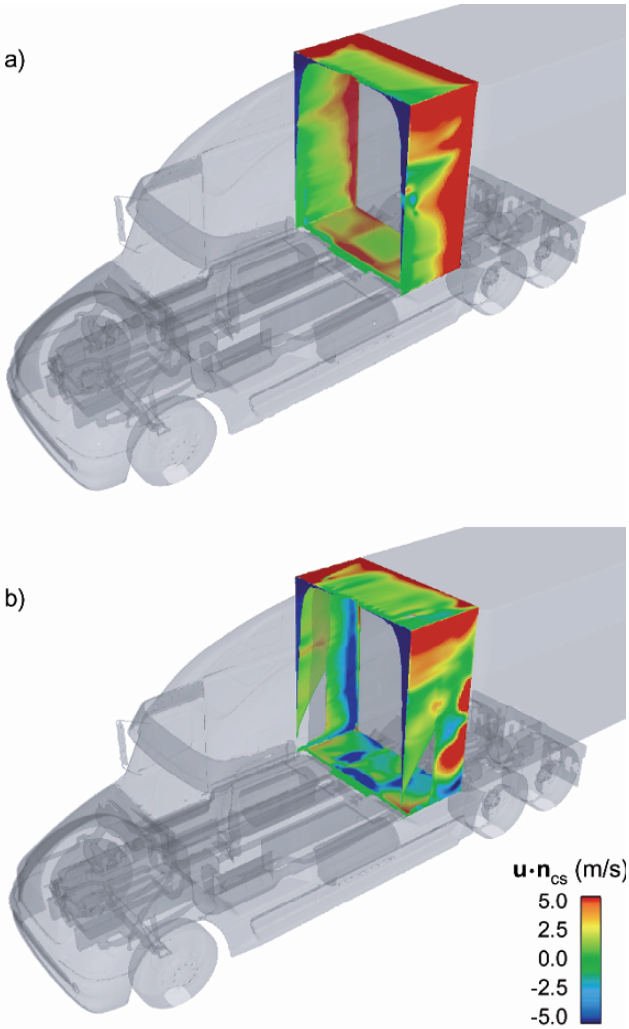

Fig. 8 Contours of $\mathbf{u} \bullet \mathbf{n}_{cs}$ over the control surface for a) a bleeding coefficient of $C_\mu = 0.13$ and b) for side extenders ($C_\mu = 0.0$).

is applied to the tractor base, this high pressure signature is diminished (Fig. 11b) and replaced with a more uniform pressure distribution that extends over nearly the entire trailer frontal face. The application of side extenders also reduces the pressure signature from the windward shear layer (Fig. 11c), though not to the extent seen for $C_\mu = 0.13$.

Plots of the pressure coefficient acting in the body axis-direction, $C_{pa} = |\mathbf{n} \bullet \mathbf{n}_a|(P - P_o)/ \frac{1}{2}\rho U_o^2$, (Fig. 12) along the vertical centerline of the tractor base and trailer frontal face demonstrate that the pressure increases on both surfaces as the bleeding coefficient is increased, where P is the fluid pressure, P_o the free-stream

pressure, and $\mathbf{n}_a$ is the unit body-axis direction vector. Calculating the average value of C_{pa} over the tractor base, trailer frontal face, and trailer base shows that the average pressure coefficient acting in the body-axis direction on the tractor base increases more rapidly than that on the trailer frontal face as C_μ is increased (Fig. 13). This subsequently reduces the difference between the average pressure coefficients on the tractor base and trailer frontal face, which is, in turn, responsible for the reduction in drag on the entire vehicle. In fact, for $C_\mu > 0.053$, the average pressure coefficient on the tractor base is greater than that of the trailer frontal face. The side extenders reduce the difference between average pressure coefficients over the tractor base and trailer frontal face, as well. However, the average pressure coefficient on the trailer base exhibits little sensitivity to either the bleeding flow or the side extenders.

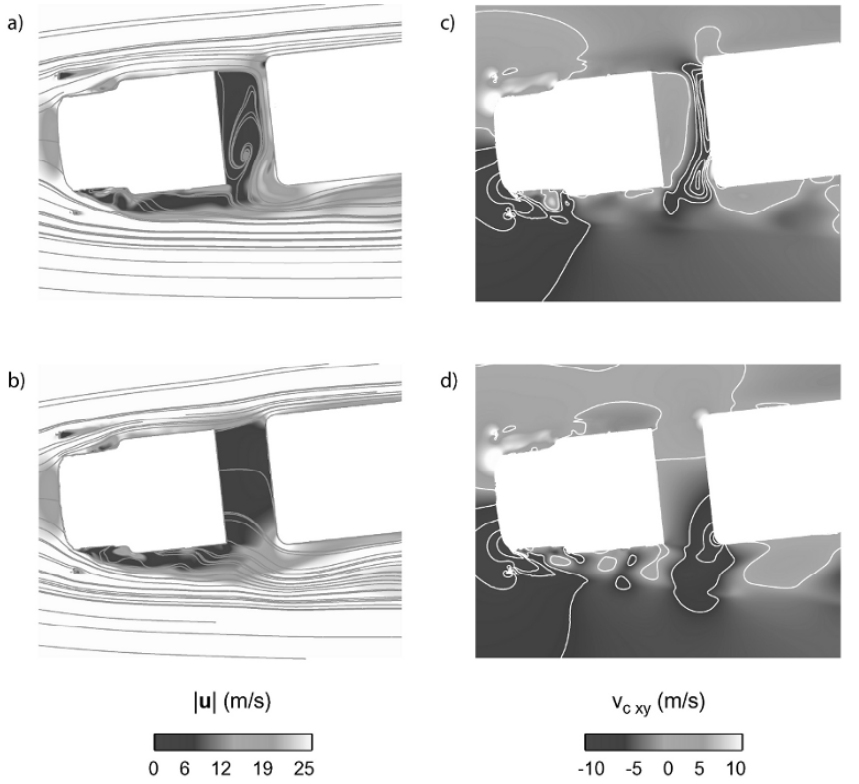

Fig. 9 a-b) Velocity magnitude and streamlines and c-d) cross-stream velocity at the mid-height of the tractor-trailer gap for C_μ equal to a,c) 0.0 and b,d) 0.13. Note that additional negative-valued contours are applied in c-d) to highlight the cross-stream gap flow.

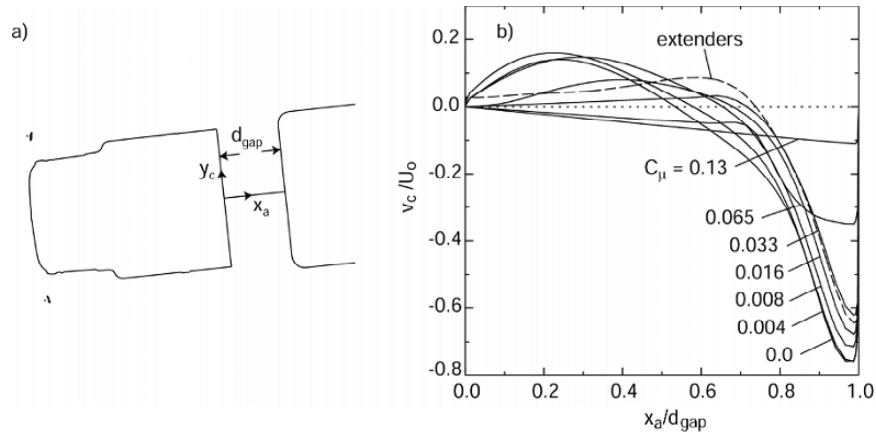

Fig. 10 a) Horizontal cross-section at the mid-height of the tractor-trailer gap. b) Non-dimensional cross-stream velocity through the gap as function of the bleeding coefficient.

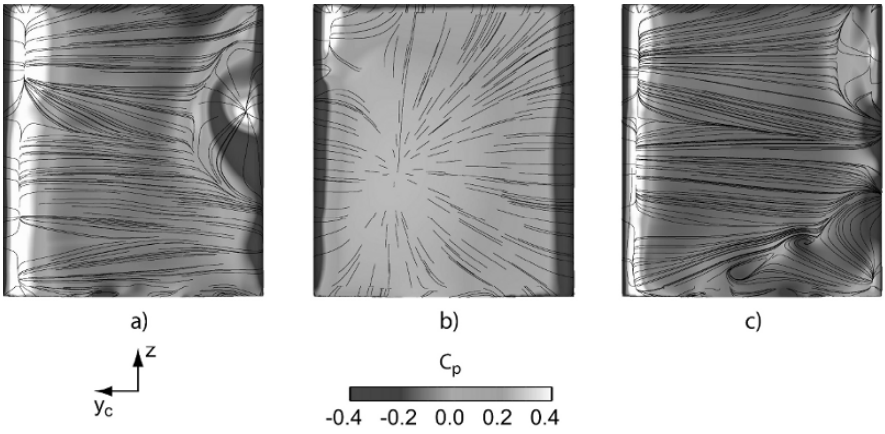

Fig. 11 Pressure coefficient and surface streamlines on the trailer frontal face for C_μ equal to a) 0.0 and b) 0.13 and for c) side extenders.

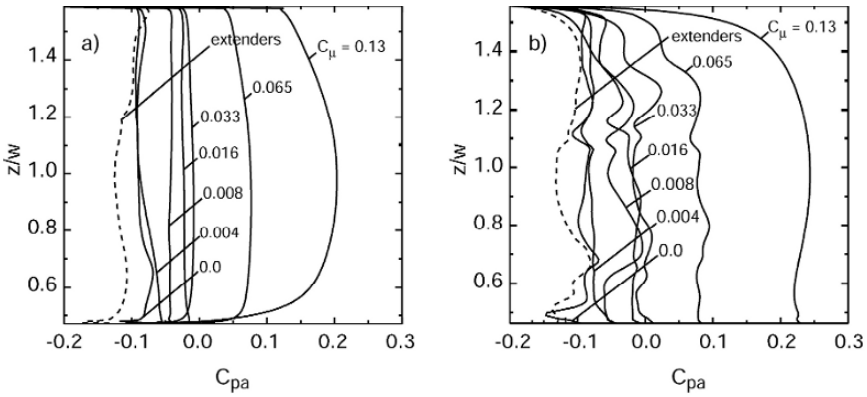

Fig. 12 Pressure coefficient in the body-axis direction on the a) tractor base and b) trailer frontal face centerlines as a function of the bleeding coefficient.

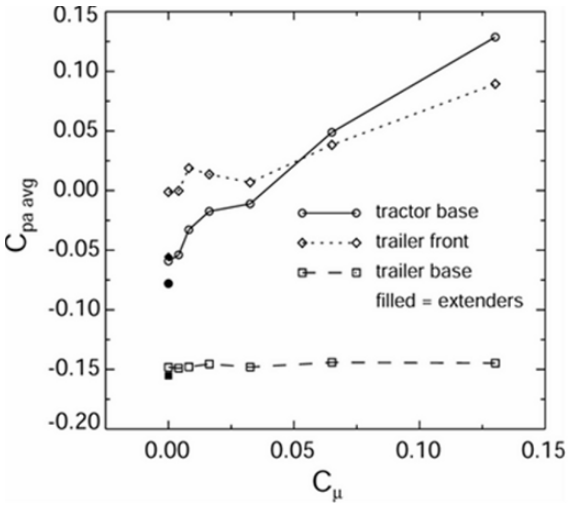

Fig. 13 Average pressure coefficient in the body-axis direction over the tractor base and trailer frontal surface and base as a function of the bleeding coefficient.

4 Conclusions

Through this investigation, we have studied the drag reduction capability of tractor base bleeding. Both the 1:20 scale wind tunnel measurements and the full-scale CFD simulations demonstrate that tractor base bleeding reduces the drag coefficient of a heavy vehicle. For bleeding coefficients greater than 0.04, the simulations show a reduction in the drag coefficient that is larger than that of side extenders. The simulation results also highlight the flow physics within the tractor-trailer gap that contribute to this drag reduction. As the bleeding coefficient increases, the rate of fluid entrainment from the free-stream into the gap decreases, which reduces both the pressure signature of the impinging windward shear layer on the trailer frontal face and the strength of the cross-stream wall jet within the gap. Lastly, tractor base bleeding reduces the difference between the average pressure coefficients on the tractor base and trailer frontal face, which is the mechanism responsible for the drag reduction.

The reason for selecting tractor base bleeding as a drag reduction concept is to alleviate the maintenance and operational issues that often arise with conventional side extenders. It is evident through the results of this investigation that tractor base bleeding may, in fact, offer an alternative means to side extenders in reducing tractor-trailer gap drag. However, the base bleeding concept is not without its own set of concerns and a number of questions remain unanswered regarding its feasibility, some of which are: how much power is required to produce the bleeding flow? Would it be more efficient to utilize solar energy or energy stored from regenerative braking to produce the bleeding flow? Can a base bleeding system be designed robustly enough so as to require a minimum level of maintenance? Under normal operating conditions, does tractor base bleeding provide a net reduction in fuel usage? Lastly, how much would a bleeding system add to the price of a tractor? Obviously, we are not in the position to answer these important questions at the present time. However, if these questions can be adequately and cost-effectively addressed, tractor base bleeding may, in the future, offer commercial fleets a viable drag reduction alternative.

Acknowledgments

The authors would like to thank Dennis Acosta and Kurt Long of NASA Ames Research Center for their assistance in performing the wind tunnel measurements. This work was performed under the auspices of the U.S. Department of Energy by Lawrence Livermore National Laboratory under Contract DE-AC52-07NA27344. UCRL-PROC-235892.

References

[1] Arcas D, Redekopp L, Aspects of wake vortex control through base blowing/suction. Phys. Fluids 16(2), 452-456 (2004)

[2] Axon L, Garry K, Howell J, An evaluation of CFD for modelling the flow around stationary and rotating isolated wheels. SAE 980032, SAE International Congress and Exhibition, Detroit, Michigan, February 23-26 (1998)

[3] Bearman P, The effect of base bleed on the flow behind a two-dimensional model with a blunt trailing edge. Aero. Quart. 18, 207-224 (1967)

[4] BDAS 9.3 Software Package, Aerospace Computing, Inc. (2006)

[5] Cooper K, Truck aerodynamics reborn: lessons from the past. SAE 2003-01-3376, SAE International Truck and Bus Meeting and Exhibition, Fort Worth, Texas, November 10-12 (2003)

[6] Cooper K, Commercial vehicle aerodynamic drag reduction: historical perspective as a guide. In: McCallen, R.C., Browand, F., Ross, J. (eds.) The Aerodynamics of Heavy Vehicles: Trucks, Buses, and Trains, pp. 9-28. Springer, Heidelberg (2004)

[7] Gill R, Freightliner, LLC, private communication (2007)

[8] Freightliner, http://www.freightlinertrucks.com/trucks/find-by-model/columbia/ (2007)

[9] Hammache M, Browand F, On the aerodynamics of tractor-trailers. In: McCallen R, Browand F, Ross J (eds.), The Aerodynamics of Heavy Vehicles: Trucks, Buses, and Trains, pp. 185-205. Springer, Heidelberg (2004)

[10] Hammond D, Redekopp L, Global dynamics of symmetric and asymmetric wakes. JFM 331, 231-260 (1997)

[11] Huerre P, Monkewitz P, Local and global instabilities in spatially developing flows. Ann. Rev. Fluid Mech. **22**, 473-537 (1990)

[12] Ingram K, The wind-averaged drag coefficient applied to heavy goods vehicles. Transport and Road Research Laboratory Supplementary Report 392 (1978)

[13] Kays W, Crawford M, Convective heat and mass transfer. McGraw-Hill, Inc., New York (1993)

[14] Koch W, Organized structures in wakes and jets—an aerodynamic resonance phenomenon? In: Bradbury L, Durst F, Launder B, Schmidt F, Whitelaw J (eds.), Turbulent Shear Flows 4, Springer (1983)

[15] Koch W, Local instability characteristics and frequency determination of self-excited wake flows. J. Sound Vib. 99, 53-83 (1985)

[16] Leal L, Acrivos A, The effect of base bleed on the steady separated flow past bluff bodies. JFM 39(4), 735-752 (1969)

[17] Leuschen J, Cooper K, Full-scale wind tunnel tests of production and prototype, second-generation aerodynamic drag-reducing devices for tractor-trailers. SAE Paper 06CV-222, (2006)

[18] MacAllister L, The aerodynamic properties and related dispersion characteristics of a hemispherical-base shell, 90-mm, HE, T91, with and without tracer element. BRL Memo. Report 990, Aberdeen Proving Ground, MD (1956)

[19] Menter F, Zonal two equation k-ω turbulence models for aerodynamic flows. Paper No. AIAA 93-2906, Proc. 24th Fluid Dynamics Conf., Orlando, Florida, USA, 6-9 July (1993)

[20] Michel G, Kost F, The effect of coolant flow on the efficiency of a transonic HP turbine profile suitable for a small engine. ASME 82-GT-86 (1982)

[21] Pointer W, Evaluation of commercial CFD code capabilities for prediction of heavy vehicle drag coefficients. Paper No. AIAA-2004-2254, 34th AIAA Fluid Dynamics Conference and Exhibit, Portland, Oregon, 28 June-1 July (2004)

[22] SAE wind tunnel test procedure for trucks and buses. SAE J1252, SAE Recommended Practice (1979)

[23] Schumm M, Berger E, Monkewitz P, Self-excited oscillations in the wake of two-dimensional bluff bodies and their control. JFM 271, 17-53 (1994)
[24] Sevilla A, Martínez-Bazán C, Vortex shedding in high Reynolds number axisymmetric bluff-body wakes: local linear instability and global bleed control. Phys. Fluids 16(9), 3460-3469 (2004)
[25] Solid Concepts, Inc., www.solidconcepts.com (2006)
[26] STAR-CD v. 3.24-3.26. CD-Adapco Group, www.cd-adapco.com (2007)
[27] Turbo Squid, www.turbosquid.com (2006)
[28] Wood C, The effect of base bleed on a periodic wake. J. Roy. Aero. Soc. 68(2), 477-482 (1964)
[29] Wood C, Visualization of an incompressible wake with base bleed. JFM 29(2), 259-272 (1967)
[30] Yao Y, Sandham N, Direct numerical simulation of turbulent trailing-edge flow with base flow control. AIAA J. 40(9), 1708-1716 (2002)

Drag Reduction on a Generic Tractor-Trailer using Active Flow Control in Combination with Solid Flaps

Christian Navid Nayeri[1], Johannes Haff[1], David Greenblatt[2], Lennart Loefdahl[3] and Christian Oliver Paschereit[1]

[1] Berlin Institute of Technology, Herrmann-Föttinger-Institut, De-10623 Berlin, Germany, christian.nayeri@tu-berlin.de, johannes.haff@gmx.de, oliver.paschereit@tu-berlin.de,

[2] Faculty of Mechanical Engineering, Technion - Israel Institute of Technology, Technion City - Haifa 32000, Israel, davidg@technion.ac.il

[3] Chalmers University of Technology, SE-41296 Göteborg, Sweden, lennart.lofdahl@chalmers.se

Abstract An experimental investigation was carried out to assess the drag reducing potential of active flow control in conjunction with flat panel flaps attached to the trailer of a generic tractor–trailer model. The experiments were carried out in a wind tunnel with a $1/10^{th}$ scale generic tractor-trailer model at Reynolds numbers up to 640,000 based on the model width. Active flow control was achieved by means of constant blowing, constant suction and oscillatory blowing and suction. A secondary objective was to make short base flaps with active flow control as effective as long flaps with no active flow control. Measurement techniques such as flow visualizations, loads by means of a 6-component balance, LDA and PIV were employed. The results show that constant blowing at a momentum coefficient of 11.13% is able to achieve higher drag reduction than long flaps with no active flow control. The analysis of the flow field in the wake showed that constant blowing deflects the shear layer between the free stream and the wake region downward and hence reduces the size of the wake. The flaps at the side of the truck did not appear to have any substantial drag reducing effect.

1 Introduction

In recent years the economy of tractor-trailer configurations has improved significantly. After the implementation of drag-reducing devices on the tractor, further investigations were aimed at drag reduction by optimisations of the trailer. In

addition to the development of side skirts and components which close the gap between the tractor and trailer it was recognized that, in particular, the trailer end contains a high drag-reducing potential.

Therefore additional components were installed at the trailer end to reduce the area thereby reducing the dead air region and hence pressure losses. In the past, the influence of several different components (e.g. boat-tailing, boat tail plates, base flaps) was investigated with respect to the drag reduction and the application to in-service trucks.

Several studies showed the drag reducing potential of flaps and that longer flaps can reduce the drag more than short flaps [1, 3, 4, 6]. Some authors attempted to increase the drag reducing effect through combination with active flow control (AFC). Englar [2] showed that Coanda blowing can be applied on trailers to reduce trailer drag. Hammache and Browand [5] investigated the effect of oscillatory forcing and found that additional drag reduction is only achieved at flap tilt angles higher than 9-10 degrees. Seifert [8] applied constant suction and oscillatory blowing to a two dimensional truck model with a fluidic device integrated in the rounded trailing corner.

The main objective of this paper is to investigate combinations of active flow control with short flat flaps with the goal of obtaining additional drag reduction. The results are compared to a passive baseline configuration with short flaps. The experiments were performed with a generic tractor-trailer model using constant suction (CS), constant blowing (CB), zero mass flux forcing (ZMF) and oscillating blowing (OB). Detailed information about the flow behaviour in the trailer wake is given by using LDA and PIV techniques for the CB configuration.

2 Experimental Setup

The experiments were performed in a closed loop 500kW-powered wind tunnel at the Hermann-Föttinger Institute. In the closed test section of 2m x 1.4m x 10m (W x H x L) a maximum velocity of U_{max}=40m/s can be achieved. The turbulence level is below 1 %. The corresponding Reynolds number is 640,000 based on the model width of $W_{trailer}$ = 0.25m at U_{max}. A six component external balance was used to determine the drag. The distance between the model wheels and the wind tunnel floor was 3mm. The floor of the wind tunnel was stationary.

Additionally, LDA and PIV-measurements were used to gain insight into the structure of the flow field in the wake of the trailer.

A $1/10^{th}$ scaled model corresponding to the longest legal European tractor-trailers was designed and constructed of medium density fibreboard. The edge radius at the front of the truck is 80mm on the roof and 40mm on the remaining edges. The dimensions of the model and the coordinate system are shown in Fig. 2.1. The model was mounted on a turntable such that yaw angles between ±30°

could be realized. The back of the model was equipped with a 1mm slot at the base of the trailer that was used for active flow control. The internal trailer volume was used as a plenum and air entered through a flexible tubing system in the bottom of the trailer. Any additional forces which were generated through blowing or suction (e.g. forces through the tubing, jet blowing) were accounted for in the drag measurements. To reduce the effect of the boundary layer thickening on the wind tunnel floor, the truck was mounted at the beginning of the test section near the contraction.

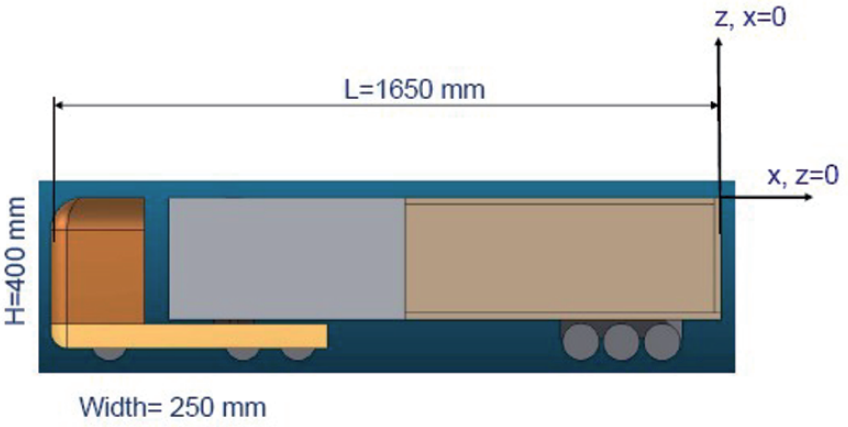

Fig. 2.1 Schematic representation of the generic tractor-trailer model

3 Baseline Configuration

As a baseline configuration the model was used without any drag reduction devices. Drag measurements were performed with different yaw angles between $\psi = \pm 30°$ to simulate side wind effects (not shown here).

The only differences between the baseline configuration and those described in the sections below, were the modifications to the base of the trailer. The gap between the tractor and trailer was always kept constant and was typical for European tractor-trailers. The drag of this configuration at $\psi = 0°$ was measured at $C_D = 0.477$.

4 Long Base Flap Configuration without AFC

The drag reduction geometry and generic model used here were designed and investigated by Zühlke [10]. In his studies the base flaps were attached to all 4 sides of the trailer without any gap or step and no AFC was applied. The flap length of 63mm corresponded to one quarter of the trailer width. This length was chosen as it is a good compromise between length and drag reduction [1]. However, it was also shown by Cooper [1] and Göring [3] that longer flaps can provide more drag reduction. The test program carried out by Zühlke [10] consisted of several configurations with different deflection angles between 10° and 20°. The maximum drag reduction was achieved with flaps deflected by 12°. All results presented in this paper were compared with this configuration in order to quantify the benefit of additional AFC. For the sake of convenience this configuration is referred to as "passive long flaps" (PLF) for the remainder of this paper. This passive configuration showed a drag reduction of $\Delta C_D = 8.22\%$ compared to the baseline. Zühlke [10] showed that for deflection angles larger than 12° the drag increased again. It is assumed that at higher deflection angles the flow is not able to stay attached to the flap resulting in a larger wake. Flow visualisation, performed with china clay and tufts provided some details about the flow behaviour. Based on tuft visualization, it was observed that the flow is attached to the whole flap surface whereas only the lower part of the side-flaps exhibited a separated flow. The visualisations with china clay confirmed these results. The flow is fully attached up to the trailing edge of the flap over the whole flap surface. A surprising observation was that the flow did not separate at the corners where the side flaps adjoin the top flap.

5 Short Base Flap Configuration with AFC

For the configuration with AFC short flaps of 40mm length with a deflection angle of 20° were applied. The motivation for these modifications compared to the PLF-configuration was to achieve more drag reduction with shorter flaps. The combination of a short flap, a higher deflection angle and AFC was intended to reduce the wake size. Shorter flaps increase the acceptance of drag-reducing components from an industrial viewpoint as the overall truck length is limited in Europe. In contrast to the PLF-case the flaps were not directly attached to the trailer but rather formed a small slot so that blowing or suction could be employed (Fig. 5.1). The trailing edge of the trailer was formed by an aluminium skirt with a thickness of 1mm. This arrangement resulted in a slot width of b_{slot}=1mm between the skirt and the flap surface. The slot extended over the top and both sides of the

trailer whereas the bottom side was only equipped with a flap without any gap. At the upper corners of the trailer where the side flaps adjoin the upper flap no slot was implemented along a length of 20mm as this area was needed to fasten the base to the back of the trailer. This reduced the total length of the effective slots.

Within the test program four different AFC methods were applied: constant suction, constant blowing, zero mass flux and oscillating blowing. The intention was to investigate their drag reducing effect in combination with the short base flap configuration. However, only the CB results are discussed here in detail, as the other methods did not produce meaningful drag reduction.

Equation 5.1 defines volumetric suction rates (Q) as a dimensionless parameter C_Q, where b_{slot} is the slot height, l_{slot} the total effective slot length, b_{flap} the length of the flap, l_{flap} the total length of all flaps and U_j is either the amplitude of the oscillatory jet fluctuation or the velocity of the constant blowing or suction.

$$C_Q = \frac{Q}{A_{flap} \cdot U_\infty} = \frac{U_{slot} \cdot A_{slot}}{A_{flap} \cdot U_\infty} = \frac{U_{slot} \cdot l_{slot} \cdot b_{slot}}{U_\infty \cdot l_{flap} \cdot b_{flap}} \cong \frac{U_{slot} \cdot b_{slot}}{U_\infty \cdot b_{flap}} \tag{5.1}$$

Equation 5.2 defines a dimensionless momentum parameter C_μ.

$$C_\mu = \frac{U_{slot}^2 \cdot A_{slot}}{0.5 \cdot U_\infty^2 \cdot A_{flap}} \cong \frac{U_{slot}^2 \cdot b_{slot}}{0.5 \cdot U_\infty^2 \cdot l_{flap}} \tag{5.2}$$

The first method tested was constant suction using the slot configuration described above. The underlying mechanism of suction is generally to remove low momentum fluid from the boundary layer in order to attach the flow to the flap surface. However, CS did not yield any drag reduction for this configuration. Therefore further tests were performed with two other orientations of the suction slots: suction orthogonal to the trailer surface and suction orthogonal to the flap surface. For these two cases longer flaps of the baseline were used. The suction rate was increased up to a maximum C_μ of more than 20%. However, these CS-cases even increased the drag (see Table 5.1). This failure is believed to be caused by the rather thick boundary layer at the trailing edge of the trailer which was measured to be δ_{99}=40mm.

The remaining three AFC methods (CB, ZMF and OB) were only applied to the short base flap configuration. The ZMF method was realised by using actuators developed at the Illinois Institute of Technology [7] which produces a sinusoidal signal. OB means that in addition to the sinusoidal signal produced by the actuators a constant blowing volume flow is superimposed. The application of ZMF provided only a small drag reduction of $\Delta C_D = 2.52\%$. Slightly more reduction was achieved with OB: $\Delta C_D = 3.35\%$. The best results were achieved with CB which was even better than the PLF-case. This confirms the idea of using a short and more deflected flap in combination with AFC. However the necessary

blowing corresponded to a very high value of C_μ = 11.13%. The jet blowing effect, which was accounted for in the drag values, was in this case 0.75% of the drag coefficient.

Table 5.1 Drag values and AFC parameters, $\psi = 0°$ (* C_D-value without AFC, ** $\Delta C_D = (C_D - C_{D,BL})/C_{D,BL}$ with $C_{D,BL} = 0.477$)

Configuration	C_D [ ]	ΔC_D **	C_μ [%]	C_Q [%]
CS parallel to the trailer surface	0.487	2.10 %	-	1.76
CS orthogonal to the trailer surface	0.496	3.98 %	-	1.76
CS orthogonal to the flap surface	0.489	2.52 %	-	1.76
Baseline Configuration (BL)	0.477	-	0	-
Long Base Flap Configuration without AFC	0.438	-8.22 %	0	-
Short Base Flap Configuration with AFC (CB)	0.435 (0.470*)	-8.81 %	11.13	-

In Table 5.1 the drag values obtained for $\psi = 0°$ are summarized for the different methods investigated. To get a better understanding of how the short flaps with CB influence the wake of the trailer, visualizations with china clay, LDV and PIV measurements were performed. With the results a comparison of the flow behaviour with and without blowing is discussed in the following. Measurements were made at C_μ = 0% (no blowing) and at C_μ = 11.13%, which provided the highest drag reduction

At first visualisations with china clay were carried out to see if the flow attached to the flap surface. The free stream velocity was U_∞=38m/s and the yaw angle was ψ=0°. For the case with no blowing Fig. 5.1 shows that the flow is not attached. It seems that the flow separates right at the trailing edge of the trailer where there is a gap similar to the baseline configuration (not shown here). Although the flow is not attached a small reduction in drag of ΔC_D= -1.47% was measured.

The visualization in Fig. 5.2 shows clearly how the flow field is affected when constant blowing is applied. The flow attaches for approximately 2/3 of the flap length. The surface streamlines visualized with china clay indicated an axial flow on the flap except at the corners. At the corners, where the top and side flaps adjoin, the streamlines indicate a vortex. This is attributed to the lack of slots for blowing at the corners.

Fig. 5.1 No blowing

Fig. 5.2 Blowing with C_μ = 11.13%

The vortex at the left corner rotates in clockwise direction. Further testing should be performed with an improved blowing slot, which allows AFC also at the corners to avoid the development of these vortices because they generate a low pressure area near the base. Low base pressures leads to an increased pressure drag. These vortices were only observed on the short flaps as flow visualization with china clay on the long flaps with no AFC (not shown here) indicated that no vortices were generated. In that case the flow was fully attached also at the corners.

It is worth noting that the flow even reattaches on the flap directly behind the slot at the beginning of the flap surface although there is a gap of 2mm between the surface of the trailer (aluminum skirt) and the surface of the flap. Fig. 5.2 was obtained at the optimum blowing rate. Higher blowing rates led to an increase in drag. It is not clear if a lower deflection angle leads to a fully attached boundary layer with better results than the 20°-configuration. Therefore further parameter studies have should be performed.

Quantitative results obtained with a 2D-LDA-System are presented below. The coordinate system used here is equal to that in Fig 2.1. The LDA-Probe was positioned underneath the wind tunnel and allowed measurements through a piecewise transparent floor for a $y/H > -0.05$ (y=0 corresponds to the centre line of the model).

LDA contour plots of the mean and fluctuation axial-velocity components (Fig. 5.3) are shown for $x/H = 0.825$ behind the trailer with view towards the rear end of the trailer. Because of the symmetric flow field, data for only one half of the trailer is shown. The black marking lines inside the plots define the right half of the trailer contour. Note that in the range of $0.325 < y/H < 0.45$ and $0.7 < z/H < 0.75$ the data is erroneous due to an increase of scattered laser light resulting in a poor signal-to-noise ratio, and therefore should be ignored.

The contour plots of the non-dimensionalized mean axial velocity U/U_∞ in Fig. 5.3 show that CB entrains high speed fluid from above the trailer down into the wake region. Thereby the dead air is moved down which leads to decreasing velocities in the lower regions.

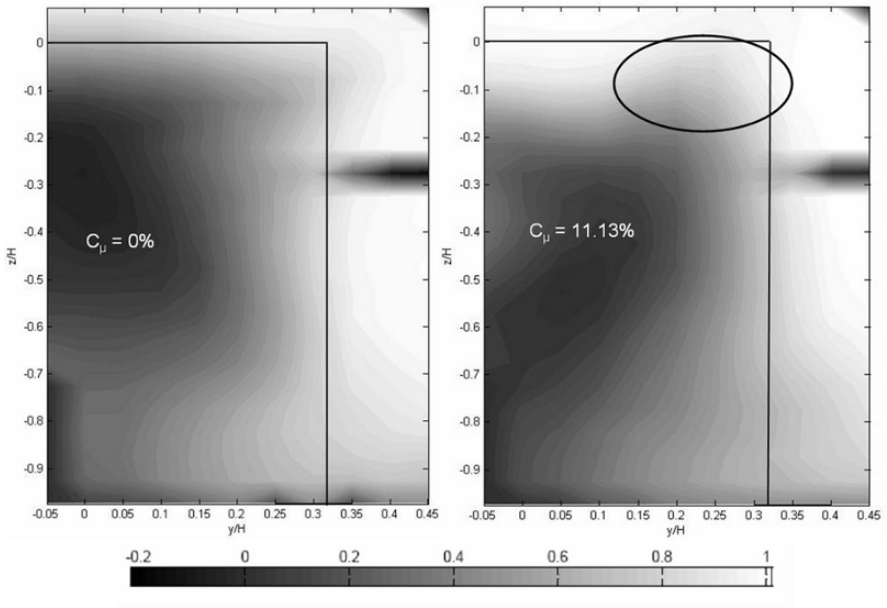

Fig. 5.3 Non-dimensionalized mean axial velocity distribution, U/U_∞, in the wake of the trailer at $x/H = 0.825$. The trailer is indicated by the solid line.

The different flow behaviour on the upper corner (see black ellipse) is due to the fact that no CB was applied there. It seems that the vortices, which were observed with the china clay visualization, influenced this part of the separation area strongly.

Additionally, CB leads to an increase of the wake extension in *y*-direction which is expected to have a negative effect with regard to the drag. The investigations of the long base flap configuration with no AFC also showed a flow separation on the bottom of the side flaps. Perhaps the ground flow influences the remaining flow field behind the trailer in a negative manner. It is speculated that the only reason why CB in combination with the short flaps has a drag reducing effect only because of the reduced wake in the upper region of the flow field.

The analysis of the contour plots of the axial fluctuations, U_{rms}, shown in Fig. 5.4 underlines the above interpretations. The upper region of the trailer wake is the most influenced area, where the turbulence level is significantly decreased, i.e. free stream fluid is moving downwards. The whole upper region, $y/H \approx 0.9\text{-}1.1$, of the trailer wake shows low turbulence levels whereas the corner region contains higher turbulence levels (see white ellipse in Fig. 5.4).

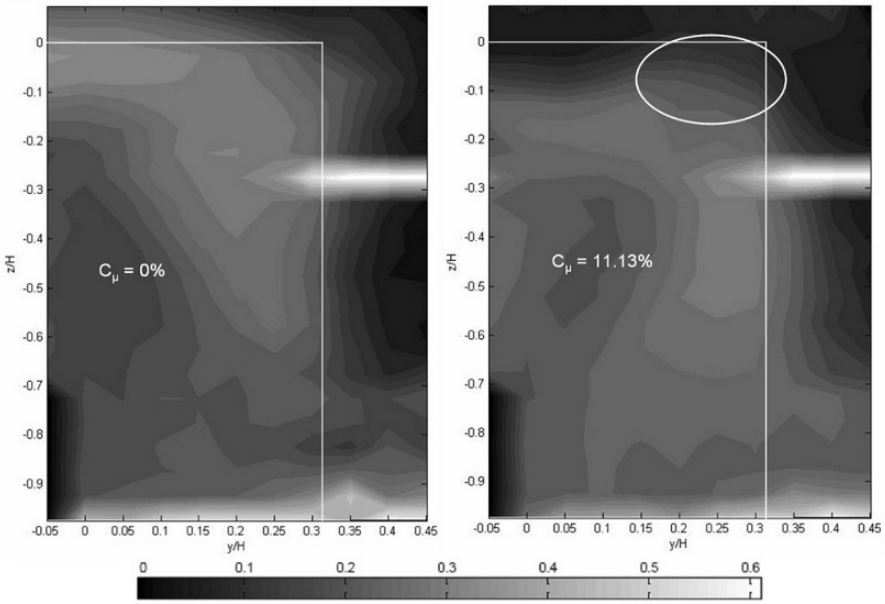

Fig. 5.4 Non-dimensionalized fluctuating axial velocity component, U_{rms}/U_{∞}, in the wake of the trailer at $x/H = 0.825$

The LDA data of Fig. 5.3 and 5.4 were made with 11x22=242 measurement points whereas Fig. 5.5 consists of 12x12=144 measurement points.
Fig. 5.5 shows the results of other LDA measurements take from the side of the wind tunnel. The figures show an *x*-*z*-plane at y/H= 0.05. The range was limited to the upper part of the trailer.

Without CB the flow seems not to be influenced by the flap. The contours of the axial velocity are essentially parallel to the upper trailer surface. The increasing velocity field at higher *x/H*-values is due to the mixing within the shear layer. Surprisingly, without control there region with a relatively high axial velocity somewhat below the flap at z/H≈-0.15. In the LDA results of Figs. 5.3 and 5.4 this region was not captured as the measurement were made further downstream at x/H=0.825. When control is applied, this region is eliminated. In combination with CB the separation area behind the trailer shows a different flow behaviour. The flow seems to be attached to the flap surface and high speed flow is deflected downwards into the wake.

However, Fig. 5.5 gives no definitive information about the flow behaviour directly on the flap surface because the resolution of the measurement grid was not fine enough.

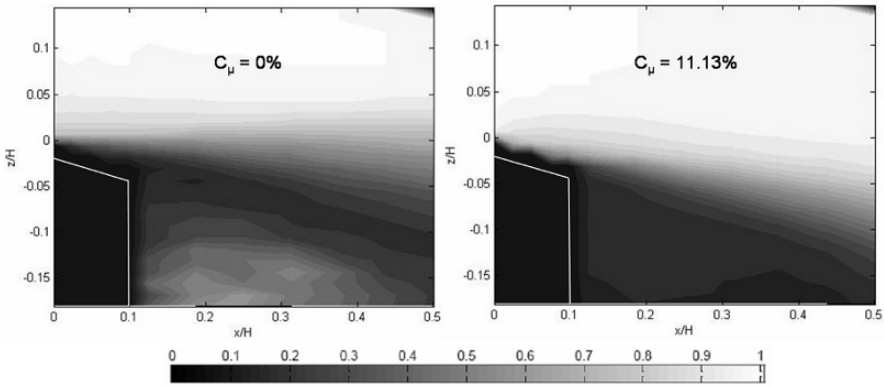

Fig. 5.5 Contours of the non-dimensionalized mean axial velocity component, U/U_∞, in the *x*-*z*-plane at y/H=0.05

The vector field and the mean spanwise vorticity (ω_y) field are plotted in Fig. 5.6. The data is based on PIV measurements and is averaged over 200 samples. The plots show that when no AFC is applied the shear layer between the free stream (indicated by the vorticity) and the wake region is orientated parallel to the axial direction. The vectors indicated a large area with recirculation. When constant blowing is activated a strong deflection of shear layer downwards takes places. This is consistent with the results of the LDA-measurements (in the PIV case the measurement grid is much finer). Moreover, the size of the recirculation area is decreased. The strong reverse flow which existed in the passive case disappears with CB activated.

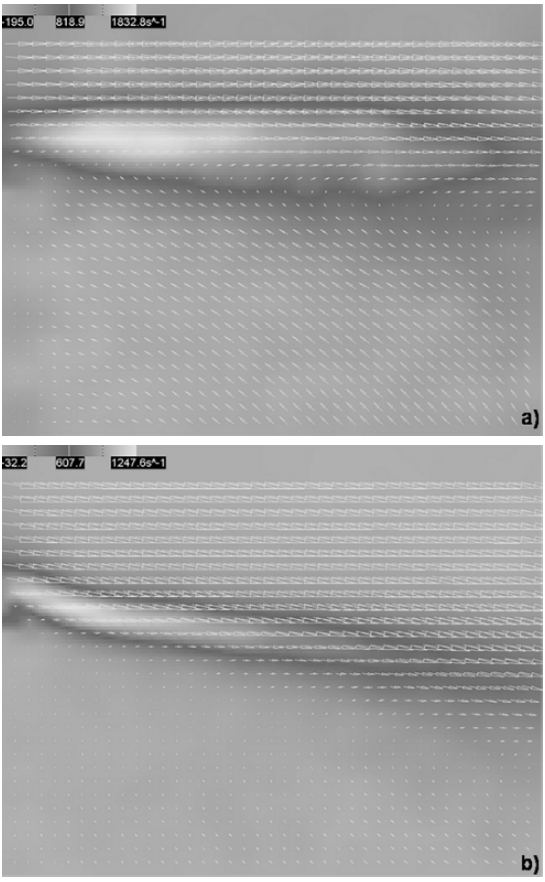

Fig. 5.6 Mean vector and spanwise vorticity field. The axial extension of the area shown corresponds to 0.4 *y/H*. a) $C_\mu = 0\%$; b) $C_\mu = 11.13\%$

6 Concluding Remarks

The present study considered the combined effect of passive and active drag reducing methods applied to a generic model of European tractor-trailer. It was shown that short base flaps combined with constant blowing through a slot at the trailing edge of the trailer could achieve a higher drag reduction than 36% longer flaps without active flow control. However, it appears that there is more potential for drag reduction as the effective slot length for blowing was not optimal. Further investigations should address this point. It is believed that the necessary momentum coefficient $C_\mu = 11.13\%$ can be reduced this way. The results also showed

that the flaps at the sides of the trailer were not as efficient as the flap at the top as they did not reduce the size of the wake in the spanwise direction. This could be attributed to the combination of two adverse effects: the vicinity of the ground (wind tunnel floor without a moving belt) with its boundary layer and the short effective length of the blowing slot. Both effects can reduce the effectiveness of the blowing as they disturb the flow.

The flow region at the lower region of the wake where the interaction between the boundary layer of the ground and the wake takes place needs also to be studied.

References

[1] Cooper K (1985) The Effect of Front-Edge Rounding and Rear-Edge Shaping on the Aerodynamic Drag of Bluff Vehicles in Ground Proximity. SAE paper No. 850288, Detroit Michigan

[2] Englar R (2004) Pneumatic Heavy Vehicle Aerodynamic Drag Reduction, Safety Enhancement and Performance Improvement. Proceedings of the UEF Conference on The Aerodynamic of Heavy Vehicles:Trucks, Buses and Trains, Lecture Notes in Applied and Computational Mechanics Springer-Verlag, Heidelberg

[3] Göhring E, Krämer W (1991) Fahrwiderstandsreduzierende Maßnahmen zur weiteren Optimierung der Wirtschaftlichkeit von Sattelzügen – Teil 1. ATZ Automobiltechnische Zeitschrift 93, pp. 434-439

[4] Gustavsson T (2006) Alternative approaches to rear end drag reduction. KTH, Department of Aeronautical and Vehicle Engineering, Royal Institute of Technology, Stockholm

[5] Hsu T-Y, Hammache M & Browand F (2004) Base Flaps and Oscillatory Perturbations to Decrease Base Drag. Proceedings of the UEF Conference on the Aerodynamic of Heavy Vehicles: Trucks, Buses and Trains, Lecture Notes in Applied and Computational Mechanics Springer-Verlag, Heidelberg

[6] McCallen R C, Salari K, Ortega J et al (2004) DOE's Effort to Reduce Truck Aerodynamic Drag – Joint Experiments and Computations Lead to Smart Design, Portland, Oregon

[7] Nagib H, Kiedaisch J, Wygnanski I et al (2003) First-In-Flight Full-Scale Application of Active Flow Control: The XV-15 Tiltrotor Download Reduction. RTO-MP-AVT-111

[8] Seifert A, Arwatz G, Palei V et al (2007) Heavy Trucks Base-Drag Reduction Using Active Flow Control. Tel Aviv, Heavy Vehicle-Aerodynamics II Conference, 2007, Lake Taho, USA

[9] Storms B, Ortega J, Salari K et al (2007) An Experimental Study of Tractor Base Bleed for Heavy Vehicle Aerodynamic Drag Reduction. Lawrence Livermore National Labority

[10] Zühlke O (2008) Investigation of aerodynamic devices to reduce aerodynamic drag of a generic tractor trailer. , Diplomathesis, ISTA (HFI), TU-Berlin

Advanced Aerodynamics and Cooling System Solutions for Higher Fuel Efficiency and Decreased Emissions

Ilhan Bayraktar

Oshkosh Truck Corp., USA
ibayraktar@oshtruck.com

Abstract Auxiliary load systems, fuel and lubrication systems, and cooling systems are an integral part of any truck, and contribute to the overall design and energy use/management. Research and development appropriate to this topic include advanced aerodynamics, heat exchanger technologies, heat pipe/two-phase flow systems, advanced pumps and compressors, and other advanced thermal and fluid management concepts to improve electric powertrain cooling, enhance drivetrain performance, reduce energy usage, improve system energy management, and reduce component and system weight, volume, and aerodynamic drag in hybrid power trains and hybrid vehicle systems. The current study presents a cooling system and vehicle aerodynamics integration through the substitution of more efficient hardware and better integration with existing vehicle systems. Several aerodynamic add-on devices are tested for drag reduction. Practical vehicle designs are developed and software simulations are conducted to determine improvements in aerodynamic efficiency. Coastdown testing is conducted to determine the drag reduction achieved with aerodynamic modifications. Weight reduction and energy consumption improvements projected for a practical aerodynamic refuse vehicle are calculated. Improved aerodynamics and cooling system designs are integrated into the current vehicle technology and tested to quantify the benefits.

Optimization of Aerodynamic Properties of High-Speed Trains with CFD and Response Surface Models

Siniša Krajnović

Chalmers University of Technology, Department of Applied Mechanics, Göteborg, Sweden, e-mail: sinisa@chalmers.se

Abstract A new procedure for optimization of aerodynamic properties of trains is presented. Instead of large number of evaluations of Navier-Stokes solver, simple polynomial response surface models are used as a basis for optimization. The suggested optimization strategy is demonstrated on two flow optimization cases: optimization of the train's front for the crosswind stability and optimization of vortex generators for purpose of drag reduction. Besides finding global minimum for each aerodynamic objective, a strategy for finding a set of optimal solution is demonstrated. This is based on usage of generic algorithms onto response surface models. The resulting solutions called Pareto-optimal help to explore the extreme designs and to find tradeoffs between design objectives. The paper shows that accuracy of the polynomial response surfaces is good and suitable for optimization of train aerodynamics.

1 Introduction

The Swedish national rail administration Banverket has in 2004 launched a new research program called "Gröna Tåget" (Eng. Green Train). One of the aims of this program is to develop a new high-speed train for Nordic conditions (meaning strong winter, large temperature differences during the year and sparsely populated region). Although the maximal speed of the new train will be 250 [km/h] compared with 200 [km/h] for the existing Swedish high-speed train X2000, the energy consumption for propelling the train should decrease by $20-30\%$. Besides, the aero-acoustic noise generated by the new train must not increase or even better should decrease. However, the aerodynamic drag increases with speed by power of two and aero-acoustic noise by power of six. The new train needs also to be lighter in order to reduce energy requirement. Although trains in past were probably unnecessary heavy, cutting in weight must be done with largest possible care in order to retain train's stability. This cannot be done without careful

consideration of crosswind stability. Another way to achieve drag reduction is to use some form of flow control, active or passive, ones the shape optimization has reached its limitation due to practical constrains. Design and placing of devices for flow control can be done in almost infinite number of ways and even here an intelligent optimization strategy is required. External aerodynamic consideration of modern high-speed trains is not constrained to drag, stability and noise but includes also upraise of ballast, slipstreams, design of air-conditioning inlets etc. This makes optimization of aerodynamic properties of trains a true multi-objective optimization problem (MOP). The present paper describes the efforts of the author to develop a numerical technique that is capable of finding one or even better a set of optimal designs of trains or its parts (e.g. train's front or flow control devices). Several aerodynamic objectives are known to be in conflict. For example, a shape of a vehicle with low drag produces often high lift. Well rounded fronts of trains which are beneficial for drag reduction can deteriorate lateral stability. The reason for this is that the rear of the train is identical with its front and rounded rear produces position of separation that varies in time and as such produces oscillating lateral forces [1,4].

2 Optimization Approach

The optimization strategy suggested in the present paper is based on construction of simplified models called metamodels or surrogate-based models. The idea is to investigate the behaviour of the aerodynamic objective functions in the design domain using evaluation of Navier-Stokes solver (denoted NS in the following text) in small sequence of design points. The design points chosen for NS simulations are not chosen in random but using special strategy called design of experiments (DOE). Ones the results from NS simulations are available the construction of metamodels can begin using regression technique. There are several different metamodels but the present paper deals only with so called polynomial response surfaces (PRS) which are low order polynomial functions. Finally, the optimization itself is now based on the resulting PRS models and not on actual NS evaluations. This results in a radical simplification of the optimization procedure as the global behaviour of aerodynamic properties is represented with simple polynomials instead of complex evaluations of non-linear differential equations. A metamodel is model of a model and the natural question is if the simplification made in such a model has filtered to much information making it unsuitable for aerodynamic optimization applications. The aim of the present paper is to investigate this.

2.1 Choice of design variables

Greatest care should be given to the choice of design variables that will be varied in the optimization procedure as their number defines the number of required NS evaluations and thus computer effort required. There are today two competing approaches for description of designs. The first one is based on prescribing limited number of points on the surface of the body controlling the geometry and than prescribing rules for change of their coordinates in space. This is implemented in a CAD toll which than provides required number of designs. Ones the geometries are available they are transferred into a meshing tool that produces numerical grids for NS solver. The second approach is using so called morphing tools directly on the grids used for NS simulations. In this approach changes in the grid are governed by rules defined in the morphing tool. Again, the user prescribes these changes in the grid using limited number of points that in turn govern changes in larger sets of computational cells. Although there is large activity in development of these tools there is yet no tool that is sufficiently robust and that provides necessary flexibility in the design process or accuracy in the resulting computational grids. Therefore the present paper uses simple description of designs in terms of physical design variables such as lengths, angles and radiuses.

In the present work two shapes are optimized, train's front and vortex generators.

2.1.1 Crosswind stability

The aim of the first case is to optimize the shape of the front of a generic train for the crosswind stability. The shape of the train is the one studied in experiments by Chiu and Squire [2] and numerical studies by Hemida and Krajnović [6] and [7] .The profile of the cross section of this model is defined by the equation

$$|y|^n + |z|^n = c^n \tag{1}$$

The coefficient of curvature, n , varies linearly along the front of the train according to the equation:

$$n = \frac{2-q}{b} z + q \tag{2}$$

where q is the value of n at the body of the train, far from the front and b is the length of the front. The second equation that describes the shape of the front from a lateral side is

$$\frac{z^2}{b^2} + \frac{y^2}{c^2} = 1 \tag{3}$$

Here, b is the length of the front, $c = h/2$ and $h = 3.0$ [m] is the height of the train (see Fig. 1b). The length of the train excluding the front and the rear (which are identical) is 30 [m].

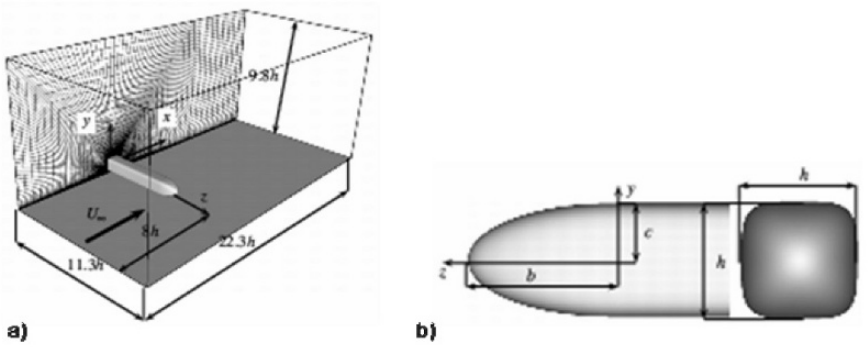

Fig. 1 a) Computational domain for the case of train influenced by a crosswind at 90^o yaw angle. b) Shape of the front of the train from a side and from in front of the train.

The design constraints were $0.64h \le b \le 1.28h$ and $4 \le n \le 6$. Such constrains were chosen in order to represent realistic length of the nose and the roundedness of the cross section of the train. The choice of the length of the train's front was in particular chosen to represent different rail vehicles from a commuter train to a high-speed train. The flow at 90^o yaw angle of the crosswind is studied in the present paper. The computational domain and the train are shown in Fig.1. A constant velocity U_∞ of 25 [m/s] is used at the inlet of the computational domain. Wall functions are used at tunnel walls and on the surface of the train while the outlet velocity condition was homogeneous Neumann.

The origin of the coordinate system is located in the centre of the cross section of the train body and on the later wall where the train was mounted. Objective functions in the present paper are drag force coefficient C_D, rolling moment coefficient C_{MR} and yawing moment coefficient C_{MY}. Drag force is the force in the z direction while rolling and yawing moments are moments acting around z and y axis, respectively. The moment canter is chosen to be at $x = 1.26$, $y = -1.95$ and $z = 0$ which is approximate position of the contact of one wheal with the track. When computing the moment coefficients the reference length and cross-sectional area of the train are chosen as $l = 3$ [m] and $A = 10$ [m/s], respectively, following the practice in train aerodynamics. However the exact cross-sectional area of the train normal to z direction was used for computation of drag coefficients.

2.1.2 Flow control

The second shape that is optimized in the present work is that of vortex generators (VG) placed on the rear of an ICE 2 high-speed train with the purpose of decrease of pressure drag (Fig. 2). Vortex generators act as small wings producing longitudinal tip vortices shown in Fig. 2b. The function of these longitudinal vortices is to sweep the high energy air from the inviscid portion of the flow-field or higher portion of the boundary layer to the inner parts of the boundary layer. As the energy is added from the high-energy air to the retarded air inside the boundary layer, the separation is delayed leading to an increased base pressure and lower drag of the train. In the present study a relatively short train is used containing only 1.25 car lengths of a real ICE2 train. Due to such a short train, the aerodynamic drag is dominated by the pressure drag and we expect the vortex generating devices to decrease the total drag.

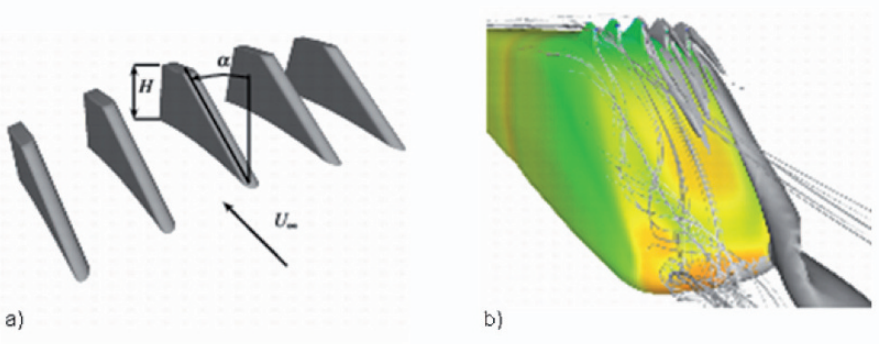

Fig 2 a) An example of VGs used in the present study with two design variables, α and H. b) The resulting flow over the rear of the train. An isosurface of streamwise vorticity component ω_x and streamlines produced from the cores of vortices behind the vortex generators are shown on the right and the left side of the figure, respectively. The body of the train is coloured with the surface pressure.

The shape of VGs is shown in Fig. 2a and in the present study two design variables: the height, H, of the VG and the angle, α, of the upstream slanted surface of VGs were varied. The design constraints were at first set as 6 [cm] $\leq H \leq$ 30 [cm] and $24^o \leq \alpha \leq 46^o$. However, later two additional designs were added with the height $H = 38$ [cm], to original six designs. The inlet and the floor boundary condition was 56 [m/s] corresponding to 200 [km/h]. The roof and the lateral walls were treated as slip surfaces while the outlet was homogeneous Neumann boundary condition for the velocities. Wall functions were used as boundary condition on the surface of the train.

The objective functions for VG case were drag and lift coefficients. Although the aim is to reduce drag the lift force should not become to large to deteriorate the

train's stability. Thus the problem was treated as a multi-objective optimization problem.

2.2 Exploration of the design space

In the present study center composite design (CCD) was used as DOE. The two DOEs are presented in Figs. 3 and 4, for the optimization of the front of the train and the VGs, respectively. Nine designs were first used for optimization in both cases. However, the number of designs for VGs was later increased to eleven. Here x_1 and x_2 are design variables normalized between -1 and 1 and between -1 and 1.67 in case of optimization of train's front and VGs, respectively.

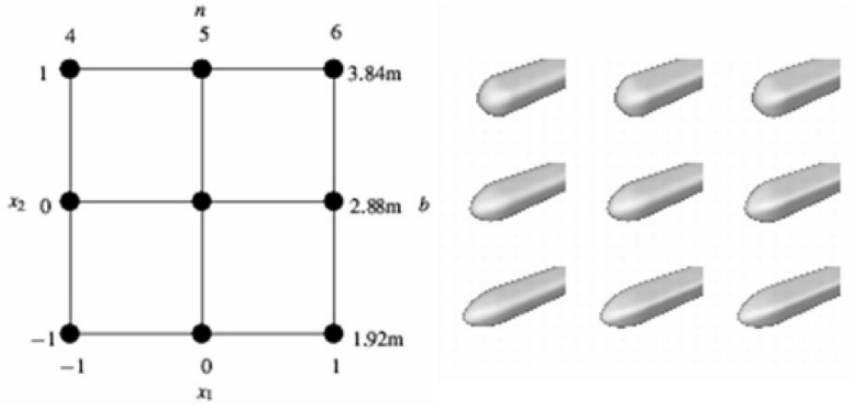

Fig 3. Canter composite design for the optimization of the front of the generic train.

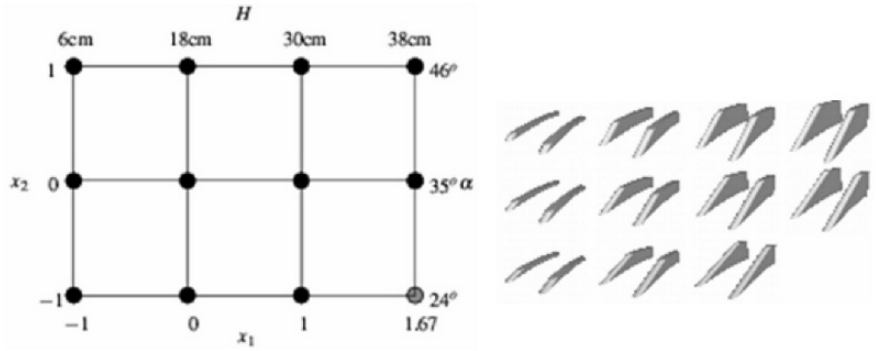

Fig 4. Canter composite design for the optimization of the VGs.

Reynolds-Averaged Navier Stokes (RANS) simulations were performed using the standard $k-$ model in optimization of train's front. However, four different

turbulence models were used for optimization of VGs. These are the standard $k-\varepsilon$ model, the RNG $k-\varepsilon$ model, the realizable $k-\varepsilon$ model and the Reynolds Stress Model (RSM) and tehy were all implemented in commercial solver Fluent 6.3. The standard $k-\varepsilon$ model was found to produce poor results for VG case. On the other hand the RNG $k-\varepsilon$ and the RSM model produced too much numerical noise due to incomplete convergence which prevented construction of a reasonable fit of RSs in the DOE points. Thus, only the results of simulations using the realizable $k-\varepsilon$ are presented in the present paper for VG case.

2.3 Polynomial response surface approximation

The approximation of the true response in a PRS is represented by low order polynomials which in the present paper are quadratic. A quadratic RS model reads

$$\hat{C} = \beta_0 + \sum_{i=1}^{n} \beta_i x_i + \sum_{j=1}^{n} \sum_{i<j}^{n} \beta_{ij} x_i x_j + \sum_{i=1}^{n} \beta_{ii} x_i^{\,2} \tag{4}$$

where n is the number of design variables and $\beta_i, \beta_{ii}, \beta_{ij}$ are the regression coefficients. The regression coefficients are determined by a least square regression. The RS can be expressed in matrix notation as $\hat{C}=\mathbf{x}^T\mathbf{b}$ where $\mathbf{b} = (\mathbf{X}^T\mathbf{X})^{-1}\mathbf{X}^T\mathbf{y}$ and $\mathbf{X}$ is the matrix containing the experimental designs.

In order to measure the goodness of fit both the coefficient of multiple determination R^2 and R-square adjusted (R_a^2) were used in the present work. The coefficient of multiple determination R^2 measures the fraction of variation in data captured by response surface.

$$R^2 = SS_R/SS_T = 1 - SS_E/SS_T \tag{5}$$

where SS_E is the sum of squared approximation errors at the n_p sampling points, SS_T is the true response's sum of squared variations from the mean $\overline{C}$, and SS_R is the approximation's sum of squared variations from the mean, i.e.

$$SS_E = \sum_{i=1}^{n_p} (C_i - \hat{C}_i)^2, \quad SS_T = \sum_{i=1}^{n_p} (C_i - \overline{C}_i)^2, \quad SS_R = SS_T - SS_E = \sum_{i=1}^{n_p} (\hat{C}_i - \overline{C}_i)^2 \tag{6}$$

A better suited measure for assessing predictive accuracy is the R-square adjusted (R_a^2) defined as

$$R_a^2 = 1 - \frac{SS_E/(n_p - n_\beta)}{SS_T/(n_p - 1)} \tag{7}$$

where n_β is the number of regression coefficients. Both R^2 and R_a^2 range between zero and one, and the higher value indicate better predicting accuracy of the response surface.

Although the full model was fitted at first, it is possible that this is not an appropriate model, i.e. it is possible that a model based on a subset of regressors in the full model may be superior. In the present work, a backward elimination procedure based on the t statistic is used to discard terms and improve the prediction accuracy. The t statistics of the fitting coefficient is defined as its value divided by an estimate of the standard error of the coefficient.

In the backward elimination we begin with a model that includes all candidate regressors (i.e. full quadratic model in the present work) and than the partial t statistics are computed for all regressors as if they were last to enter the model. The smallest of these partial t-statistics is compared with preselected value, t_{out} and if it is less than t_{out}, that regressor is removed from the model. A rule of thumb saying that regressor terms with absolute value of t larger than 2 are significant at a 95% confidence interval, was used in the present paper. Thus the regressor terms are removed from the model if regressor's t is smaller than 2 and if R_a^2 increases after regressor's removal.

2.4 Variable selection and backward elimination

This chapter demonstrates improvement of models (in form of PRS) using backward elimination procedure.

According to Table 1, the full quadratic response surface model for the drag coefficient has R_a^2 of 0.9850. Determination of the mixed-term regressor β_{12} involves a large standard error (exposed by $t = 0$ in Table 1). Discarding this term leads to an increase of R_a^2 to 0.9888. Thus elimination of this term improves the fit. The quadratic-term regressor β_{11} has also $t < 2$. However, discarding this term leads to reduction of R_a^2 to 0.9865 and the regressor β_{11} is not removed from the model. Thus the best quadratic PRS of the drag coefficient is

$$\hat{C}_D = 1.33 + 0.06x_1 - 0.02x_2 - 0.01x_1^2 - 0.05x_2^2 \tag{8}$$

2.4.1 Improvement of the model for the case of the train's front

Table 1 Backward elimination procedure for response surface approximation of the drag coefficient. Optimization of the train's front at 90^o yaw angle.

Coefficient	t (full)	t $(-\beta_{12})$	t $(-\beta_{11})$
β_0	231.41	267.21	313.86
β_1	20.15	23.27	21.24
β_2	-5.83	-6.74	-6.15
β_{12}	0	–	–
β_{11}	-1.22	-1.41	–
β_{22}	-9.49	-10.96	-10.00
Removed regressors	R^2	R_a^2	
—-	0.9944	0.9850	
β_{12}	0.9944	0.9888	
β_{11}	0.9916	0.9865	

Similar procedure of backward elimination is made for the rolling and the yawing moment coefficients. The results of the procedure are presented in Tables 2 and 3 and the resulting PRS model are

$$\hat{C}_{MR} = 1.75 + 0.11x_1 + 0.04x_2 - 0.04x_1^2 + 0.1x_2^2 \tag{9}$$

$$\hat{C}_{MY} = 7.75 + 0.76x_1 + 0.3x_2 - 0.05x_1^2 + 0.87x_2^2 \tag{10}$$

Contour plots of PRS in Eqs. 8,9 and 10 together with their global minima are presented in Fig. 5.

Minimization of PRSs was performed using constrained nonlinear optimization in MATLAB. The $\hat{C}_D$ obtains its minimal value of 1.188 at $n = 4$ and $b = 3.84$ [m], i.e. for the longest and most rounded train. On the other hand the optimal $\hat{C}_{MR}$ and $\hat{C}_{MY}$ are obtained for the most rounded train with an intermediate length of $b = 2.70$ [m] and $b = 2.71$ [m], respectively. The minimal $\hat{C}_{MR}$ and $\hat{C}_{MY}$ found for these designs are 1.6 and 6.92, respectively.

Table 2 Backward elimination procedure for response surface approximation of the rolling moment coefficient.

Coefficient	t (full)	$t\ (-\beta_{12})$	$t\ (-\beta_{11})$
β_0	85.42	98.63	97.37
β_1	9.95	11.49	8.91
β_2	3.27	3.77	2.92
β_{12}	0	–	–
β_{11}	-1.80	-2.08	–
β_{22}	5.15	5.94	4.60
Removed regressors	R^2	R_a^2	
—-	0.9789	0.9438	
β_{12}	0.9789	0.9579	
β_{11}	0.9562	0.9299	

Table 3 Backward elimination procedure for response surface approximation of the yawing moment coefficient.

Coefficient	t (full)	$t\ (-\beta_{12})$	$t\ (-\beta_{11})$
β_0	183.17	195.92	234.33
β_1	32.65	34.92	32.50
β_2	13.02	13.92	12.96
β_{12}	0.71	–	–
β_{11}	-1.25	-1.33	–
β_{22}	21.55	23.05	21.45
Removed regressors	R^2	R_a^2	
—-	0.9982	0.9953	
β_{12}	0.9979	0.9959	
β_{11}	0.9970	0.9953	

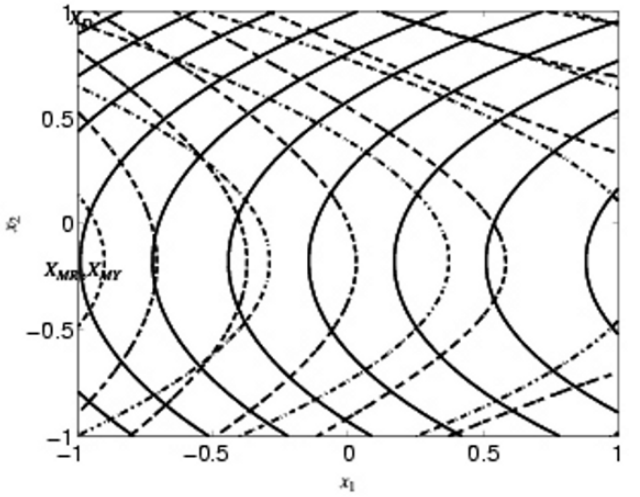

Fig 5. Contour plot of response surfaces for $\hat{C}_D$ (solid line), $\hat{C}_{MR}$ (dashed line) and $\hat{C}_{MY}$ (dashed-dotted line). Minimal values of $\hat{C}_D$, $\hat{C}_{MR}$ and $\hat{C}_{MY}$ are denoted with X_D, X_{MR} and X_{MY}, respectively.

2.4.2 Improvement of the model for the case with VGs

Table 4 Backward elimination of the polynomial response surface approximations for VG case.

	Removed terms	R^2	R_a^2
2nd order PRS for C_D	− − −	0.9231	0.8461
	β_{12}	0.9144	0.8573
	β_{22}	0.8824	0.8320
	Removed terms	R^2	R_a^2
2nd order PRS for C_L	− − −	0.9259	0.8517
	β_{11}	0.9259	0.8765
	β_{12}	0.9259	0.8941

The original RS was a second-order polynomial that was constructed over the design domain $6\,[\text{cm}] \le H \le 30\,[\text{cm}]$ and $24^o \le \alpha \le 46^o$. Ones the PRS

were constructed, it was found that the minimal value of $\hat{C}_D$ was at the edge of the design domain. Thus, two additional designs with $H = 38$ [cm] were added to the original six designs (black dots in Fig. 4). Also here t statistics were used to eliminate the regressors with insignificant or damaging influence onto the responses. Table 4 shows that R_a^2 for complete 2nd order PRS for $\hat{C}_D$ and $\hat{C}_L$ are 0.8461 and 0.8517, respectively. This was slightly improved to 0.8573 and 0.8941 for $\hat{C}_D$ and $\hat{C}_L$, respectively, using backward elimination procedure. The PRS models produced the optimal designs for both objective functions for vortex generator with maximal height and smallest angle (Fig. 6).

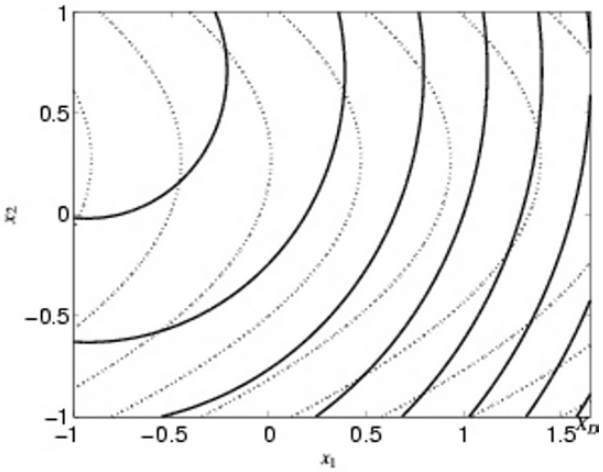

Fig 6. Contour plot of response surfaces for $\hat{C}_D$ (solid line) and $\hat{C}_L$ (dashed line) for VG case. Minimal values of $\hat{C}_D$ and $\hat{C}_L$ are denoted with X_D and X_L, respectively.

2.5 Validation of metamodels

Beside the measure of fit described above, another test in form of verification of the accuracy of the model prediction can be performed on the constructed metamodel in order to ensure its accuracy. This is done by constructing a new design that was used for the construction of the model and perform new computer experiment. The objective functions provided from this new simulation are then compared with the model prediction. For the purpose of validation of PRS approximations for the case of the train's front, flow around an additional train with $n = 4.015$ and $b = 3.52$ [m] was simulated. NS simulation of this new design resulted in following drag and moment coefficient: $C_D = 1.203$, $C_{MR} = 1.731$

and $C_{MY} = 7.892$ compared with responses $\hat{C}_D = 1.224$, $\hat{C}_{MR} = 1.675$ and $\hat{C}_{MY} = 7.542$ resulting from Eqs. 8-10. Thus the relative error between the NS simulated and the modeled objectives were 1.8%, 3.2% and 4.4% for the C_D, C_{MR} and C_{MY}, respectively. For the VG case, the design with maximal height and minimal angle was evaluated using NS simulation. This design point is located outside the DOE and the accuracy of the RS's approximation here is not expected to be large. The resulting C_D value was found to be 0.1068 compared with $\hat{C}_D = 0.1006$ resulting from PRS model. Thus the modelling error was approximately 5.8%.

3 Optimization Based on Metamodels

The multi-objective problem of the train's front resulted in both objectives with optimal values for the same design. For a short train used in the present paper a drag reduction of approximately 5% was achieved using the optimal design of VGs. However objectives were in conflict for VG case and this MOP was solved using an evolutionary multi-objective optimization procedure (so called real-coded genetic algorithm NSGA-II) by Deb *et al.* [3]. Running this genetic algorithm together with computer experiments (NS simulations) would be extremely computer demanding. However, since the metamodels for each objective are available in form of simple polynomial expressions, the evaluation of generic algorithm is fast and efficient. The objective of such an algorithm is to find solutions (in form of combinations of objectives) such that there is no other solution for which at least one objective has better value while values of remaining objectives are the same or better. Solutions obtained using this optimization procedure are called Pareto-optimal. The parameters chosen for the NSGA－II simulations are presented in Table 5.

Table 5 Parameters used for the NSGA－II simulation.

Population size	100
Generations	100
Crossover probability	0.9
Distribution parameter (for crossover)	20
Mutation probability	0.25
Distribution parameter (for mutation)	20

A population of hundred train designs were regenerated hundred times resulting in hundred Pareto-optimal solutions shown in Fig. 7a. Rolling and yawing moment coefficients tend to produce very similar optimal designs while drag

coefficient is in conflict to these two moment objectives. Figure 7a shows the Pareto optimal set of the three objectives. Note that the objectives on the axis are scaled due to relatively small changes in optimal designs. Pareto optimal solutions of two objectives in conflict $\hat{C}_D$ vs. $\hat{C}_{MR}$ presented in Fig. 7b show for example a reduction of 4% in drag by changing design results in an increase of rolling moment coefficient of 6%.

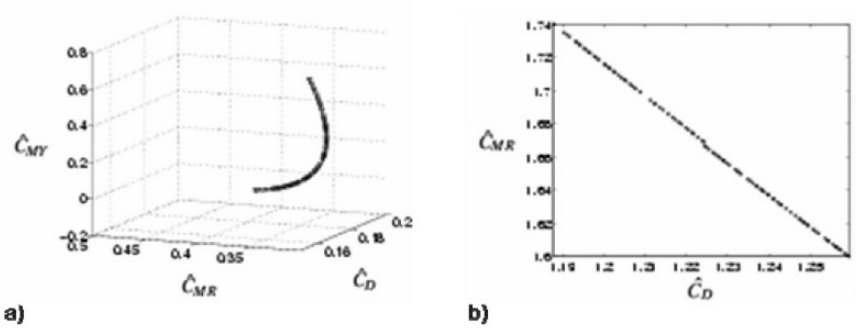

Fig. 7 a)Pareto optimal solutions for $(\hat{C}_D - 1.259)\times 10^4$, $(\hat{C}_{MR} - 1.599)\times 10^4$ and $(\hat{C}_{MY} - 6.917)\times 10^4$. b) Pareto optimal solutions for $\hat{C}_D$ vs. $\hat{C}_{MR}$.

4 Discussion

The present paper shows that optimization of train's aerodynamics can be done using simple polynomial response surfaces instead of complex NS simulations. Although only a first attempt is presented, a fairly good accuracy of objective functions was achieved with only second order PRSs. However, there are other metamodels available such as radial basis neural networks (RBNN) or Kriging models. It is reasonable to expect that these or some blend of these models will provide even better fit with the data and accuracy of the model than pure PRSs. Two optimization cases presented here illustrate the importance of choice of turbulence models in NS simulations on the optimization. Unfortunately the weakness of the Reynolds-Averaged Navier-Stokes simulations reflects on the optimization results. Besides, convergence problems often prevent reasonable fit of response surfaces with the data in DOE making them useless for the optimization purposes. On the other hand models such as standard $k-\varepsilon$ which almost always converge can produce inaccurate metamodel. In wait for a tremendous increase of computer power required for time-dependent NS simulations an appropriate trade-off between the accuracy and fit of metamodels with RANS data must be made. Making the optimization process automatic is of highest priority for putting the

suggested technique into production. Providing computational grids for designs in DOE is the Achilles heel of any such attempt. Hopefully new morphing and CAD tools will overcome this problem.

5 Acknowledgments

This work is financed by Banverket (Swedish National Rail Administration) under contract no.S05-3157/AL50 and it is a part of the project called Gröna Tåget (Eng. Green Train). FLUENT Sweden and Bombardier Transportation are supporting the project. Computer time at SNIC (Swedish National Infrastructure for Computing) resources at the Center for scientific computing at Chalmers (C3SE) is gratefully acknowledged. Several computational meshes used in simulations were made within student diploma projects [5,8].

References

1. Diedrichs B, Berg M, Stichel S and Krajnović S: (2007) Vehicle dynamics of a highspeed passenger car due to aerodynamics inside tunnels, I MECH E Part F Journal of Rail and Rapid Transit, Vol. 221, pp. 527-545
2. Chiu T and Squire L: (1992) An experimental study of the flow over a train in a crosswind at large yaw angles up to 90^0, Journal of Wind Engineering and Industrial Aerodynamics,45: pp. 47-74.
3. Deb K, Agrawal S, Pratap A and Mayarivan T: (2000) A fast and elitist multiobjective genetic algorithm for multi-objective optimization: NSGA-II, Parallel problem solving from nature VI conference, Paris, pp. 849-858.
4. Diedrichs B, Krajnović S and Berg M: (2008) On Tail Vibrations of Very High-Speed Trains Cruising Inside Tunnels, Engineering Applications of Computational Fluid Mechanics, 2(1):pp. 51-75.
5. Bjerklund E, Emilsson J, Hobroh E, Lenngren J, Norrgård C and Rynell A: (2007) Design of high-speed trains for cross-wind stability, Bachelor thesis (kandidatarbete), Departments of Applied Mechanics, Chalmers University of Technology, Gothenburg.
6. Hemida H, Krajnović S: (2006) Exploring the flow around a generic high-speed train under the influence of side winds using LES, Fourth International Symposium on Computational Wind Engineering, July 16-19, Yokohama, Japan.
7. Hemida H, Krajnović S and Davidson L: (2005) Large eddy simulations of the flow around a simplified high speed train under the influence of cross-wind. 17th AIAA Computational Dynamics Conference}, Toronto, Ontario, Canada.
8. Georgii J, Gustafsson O, Joelsson E, Martini H, Näsholm K and Ringius G: (2007) Drag reduction of high-speed trains using vortex generators, Bachelor thesis (kandidatarbete), Departments of Applied Mechanics, Chalmers University of Technology, Gothenburg.